**UNIVERSITÀ DEGLI STUDI DI MILANO**
FACOLTÀ DI SCIENZE MATEMATICHE,
FISICHE E NATURALI
Corso di Laurea Magistrale in Fisica

# Higgs mass measurement in the di-photon decay channel with the ATLAS experiment.



Relatore: Dott. Leonardo Carminati

Correlatore: Dott. Ruggero Turra

Tesi di Laurea di:

Rimoldi Marco

Matr. 808083

Codice P.A.C.S.: 14.80.bn

Anno Accademico 2012 - 2013

# Contents

*Dedicated to my family*

# Riassunto

Questo lavoro di tesi si è svolto all'interno del gruppo di ricerca di fisica delle particelle elementari dell'Università degli Studi di Milano, nell'ambito dell'esperimento ATLAS al Cern di Ginevra. Questo esperimento è stato progettato per sfruttare appieno le potenzialità del collider adronico LHC andando a esplorare regioni di energia e di luminosità mai raggiunti fino ad ora.

Nella mia tesi ho effettuato la misura della massa del bosone di Higgs nel canale di decadimento in due fotoni utilizzando i dati di collisioni p-p raccolti nel 2012 ad una energia nel centro di massa di 8 TeV corrispondenti a $20.3\,\mathrm{fb}^{-1}$.

Questo decadimento è caratterizzato da un piccolo branching ratio ($\sim 10^{-3}$) ma presenta una risoluzione di massa molto buona (FWHM $\sim$ 3.6 GeV) e una segnatura sperimentale semplice corrispondente a due fotoni energetici isolati che rilasciano tutta la loro energia nel calorimetro elettromagnetico. Il segnale del bosone di Higgs (cross section $\simeq 3 \cdot 10^{-2}$ pb) deve essere estratto da un fondo irriducibile di QCD $\gamma\gamma$ (30 pb) e da un fondo riducibile di eventi $\gamma$-jet ($\sim$ 20% del fondo totale) e jet-jet ($\sim$ 0.03%) dove i jet sono ricostruiti erroneamente come fotoni.

Una prima misura in questo canale di decadimento è stata effettuata e resa pubblica nel Marzo 2013 e ha portato come risultato:

$$m_H = 126.7 \pm 0.7 \text{ GeV} \tag{1}$$

Nel mio lavoro di tesi ho contribuito all'affinamento della misura e alla riduzione dei sistematici sperimentali. La comprensione del funzionamento del calorimetro ha un impatto cruciale sulla determinazione della massa e i relativi errori sistematici dell'Higgs; è stato per questo svolto un importante sforzo per la rideterminazione e rivaluatazione della procedura di calibrazione del calorimetro cercando di ridurre le incertezze sistematiche correlate.

Il calorimetro di ATLAS è diviso longitudinalmente in 3 layer (L1,L2,L3) nella regione $|\eta| < 2.5$ e un Presampler è aggiunto nella regione centrale $|\eta| < 1.8$. Avendo differenti dimensioni e caratteristiche è necessario definire una scala di calibrazione che corregga le differenze tra dati e le simulazione MC. In particolare viene definita una scala intrinseca per il PS e una scala relativa tra L1 e L2. Ai dati e alle simulazione MC viene poi applicata una calibrazione basata su un algoritmo multivariato che cerca, a partire da quantità misurate nel rivelatore, di risalire all'energia dell'oggetto ricostruito ottimizzandone la risoluzione. Una scala globale estratta dal picco del decadimento $Z \to e^+e^-$ conclude la procedura di calibrazione. Le incertezze nel metodo

di estrazione di queste scale insieme alle incertezze sulle correzioni di uniformità di risposta del calorimetro entrano direttamente nella determinazione dei sistematici correlati all'energia dei fotoni.

Nuove misure data driven hanno permesso di conoscere il materiale del rivelatore con maggiore precisione: è stata per questo definita una nuova geometria per la descrizione del detector e questo ha permesso di diminuire gli errori sistematici correlati alla determinazione del materiale passivo. Ho studiato l'impatto sull'energia dei fotoni causato da aggiunta di materiale in particolari regioni sensibili del rivelatore.

Mi sono occupato di propagare le incertezze sulla energia dei fotoni ad incertezze sulla posizione del picco del segnale dell'Higgs. Per fare questo ho valutato lo spostamento del picco di massa invariante ricostruita dai due fotoni dopo aver applicato una variazione di $1\sigma$ di un particolare sistematico. Ho utilizzato differenti metodi validandone la procedura di estrazione. Le sistematiche sulla posizione del picco entrano come parametri (""nuisance parameter"") nel fit finale della massa. E' stata posta particolare attenzione nella definizione di un modello di correlazione per le sistematiche dei due fotoni seguendo il modo con cui esse sono state ricavate.

I fotoni selezionati nei dati sono stati divisi in 10 categorie tenendo conto delle proprietà legate al detector (pseudorapidità), allo stato di conversione dei fotoni e a proprietà cinematiche del decadimento. Ho valutato le performance attese in molte categorizzazioni e scelto quella che minimizza l'errore aspettato sulla massa.

La misura della massa avviene definendo una likelihood combinando l'informazione delle 10 categorie. Il modello di segnale è stato estratto dai MC pesando i vari modi di produzione dell'Higgs nelle proporzioni previste dal Modello Standard in funzione della massa dell'Higgs da stimare. Il modello di background viene invece scelto utilizzando campioni MC di solo background ad alta statistica e scegliendo la funzione che minimizza ogni possibile bias introdotto dalla scelta della parametrizzazione. I parametri della funzione scelta sono direttamente fittati sui dati.

Il valore della massa dell'Higgs è estratto dalla minimizzazione di un Profile Likelihood Ratio:

$$-2\ln\lambda(m_H) = -2\ln\left(\frac{L(m_H,\hat{\hat{\theta}})}{L(m_H,\hat{\theta})}\right) \tag{2}$$

dove il parametro di interesse è $m_H$, $\hat{\hat{\theta}}$ sono i nuisance parameter che massimizzano la likelihood per l'ipotesi di massa $m_H$ e $\hat{\theta}$ sono i nuisance parameter che massimizzano senza condizioni la likelihood. L'errore di $m_H$ è valutato come differenza tra il valore misurato della massa meno il valore di $m_H$ che intercetta la $-2\ln(\lambda(m_H))$ a 1.

# Introduction

This thesis work was carried out within the research group of elementary particle physics at the University of Milan, for the ATLAS experiment at CERN in Geneva . This experiment was designed to exploit the full potential of the hadron collider LHC going to explore regions of energy and luminosity never achieved until now.

In my thesis I made the mass measurement of the Higgs boson in the di-photon decay channel using data from pp collisions collected in 2012 to center mass energy of 8 TeV corresponding to $20.3\,\mathrm{fb}^{-1}$.

This decay is characterized by a small branching ratio ( $\sim 10^{-3}$ ) but has a very good mass resolution (FWHM $\sim$ 3.6 GeV ) and a simple experimental signature corresponding to two isolated photons that release all their energy in the electromagnetic calorimeter. The signal of the Higgs boson ( cross section $\simeq 3 \cdot 10^{-2}$ pb ) must be extracted from an irreducible background of QCD $\gamma\gamma$ ( 30 pb ) and a reducible background events $\gamma$-jet ( $\sim$ 20% of the total fund ) and jet-jet ($\sim$ 0.03%), where the jets are reconstructed incorrectly as photons.A first measurement in this decay channel is been carried out and yield public in March 2013 and has resulted:

$$m_H = 126.7 \pm 0.7 \text{ GeV}$$

In my thesis I have contributed to the refinement of the measurement and reduction of systematic experimental . The understanding of the operation of the calorimeter has a crucial impact on the determination of the Higgs mass and the relative systematic errors; An important effort was done for the restatement and re-evaluating of the calibration procedure of the calorimeter trying to reduce the systematic uncertainties related .

# Chapter 1

# The SM and the Higgs Boson

## 1.1 Interaction

The Standard Model of particle physics (SM) is a elegant and concise theory of elementary particle and their interaction [1, 2, 3]. The main elementary constituents of matter are point-like spin-$\frac{1}{2}$ particles called *fermions*. They obey to the Dirac free Lagrangian:

$$L_{free} = \bar{\Psi}(\gamma^{\mu}\partial_{\mu} - m)\Psi \quad (\bar{\Psi} \equiv \Psi^{+}\gamma^{0}) \tag{1.1}$$

yielding the Dirac Equation for free fermions

$$(i\gamma^{\mu}\partial_{\mu} - m)\Psi = 0 \tag{1.2}$$

Each component of $\Psi$ is a function of the space-time coordinates x, $\gamma^{\mu}$ are the Dirac matrix and $m$ the fermion mass.The previous formalism only describes the free or non-interacting fields theory. Interactions are typically introduced by requiring local gauge invariance under a specific symmetry group. For example, a redefinition of the field under the $U(1)$ group of the form $\Psi \to \Psi' \equiv e^{i\Theta(x)}\Psi$ should not alter the Lagrangian by more than a total derivative of a function of the coordinates. Consider equation 1.2 you get:

$$\partial_{\mu}\Psi(x) = \partial_{\mu}\Psi'(x) = e^{i\theta(x)}\left[\partial_{\mu} + i\partial_{\mu}\Theta(x)\Psi(x)\right] \tag{1.3}$$

This is not invariant but the invariance can be restored by the addiction of a spin-1 field $A_{\mu}(x)$, which transforms as $A_{\mu}(x) \to A_{\mu}(x)' \equiv A_{\mu}(x) - iQ\partial_{\mu}$ where Q is a constant, under the same U(1) symmetry. The transformation of the $A_{\mu}$ field allows to cancel the right term in equation 1.3. The normal derivative can be replace by the covariant derivative:

$$D_{\mu}(x)\Psi(x) = [\partial_{\mu} + iQA_{\mu}(x)]\Psi(x) \tag{1.4}$$

After the introduction of the free Lagrangian term for the $A_\mu$ field one obtain a Lagrangian invariant under the $U(1)$ symmetry.

$$L = \bar{\Psi}(\gamma^\mu D_\mu - m)\Psi - QA_\mu\bar{\Psi}\gamma^\mu\Psi - \frac{1}{4}F^{\mu\nu}F_{\mu\nu} \tag{1.5}$$

where $F^{\mu\nu} = \partial^\mu A^\nu - \partial^\nu A^\nu$. The quantization of this Lagrangian leads to the theory of Quantum Electromagnetic (QED). The field $\Psi$ are identified with the fermions, as $e/\mu\ /\tau$, and a gauge boson $A^\mu$ with the photon. Mass terms for the field $A^\mu$ of the form $m_a^2 A^\mu A_\mu$ cannot be added in the Lagrangian because they would spoil the gauge invariance.

### 1.1.1 Quantum ChromoDynamics (QCD)

QCD is a Yang-Mills theory based on a gauge group $SU(3)$. The matter fields are the quarks, they are in the fundamental representation of the gauge group and have spin $\frac{1}{2}$. Quarks are electrically charged and also carry an other quantum numbers, called *color charge*. Therefore a quark field has two indices, $\Psi^{\alpha,A}$ with $\alpha = 1, 2, 3$ the color index and A the flavor index. Each quark is described by a Lagrangian of the type:

$$L_{QCD} = \sum_f \bar{q}_f\left(i\gamma^\mu\partial_\mu - m_f\right)q_f - g_s G_a^\mu \sum_f \bar{q}_f^\alpha\gamma^\mu\left(\frac{\lambda^a}{2}\right)_{\alpha\beta} q_f^\beta - \frac{1}{4}G_a^{\mu\nu}G_{\mu\nu}^a \tag{1.6}$$

where:

- $g_s$ represents the strength of the interaction
- $\lambda_a$ $SU(3)$ matrix and represents the interaction between the quarks and the gluon fields $G_a^\mu$
- $G_a^{\mu\nu}$ is the kinetic term for the gluons.

$$G_a^{\mu\nu} = \partial^\mu G_a^\nu - \partial^\nu G_a^\mu - g_s f^{abc} G_b^\mu G_c^\nu$$

### 1.1.2 Electro-Weak Interaction

The Electro-Weak theory [1, 2] is described in a $SU(2)_L \otimes U(1)_Y$ gauge symmetry group. The subscript L refers to left-handed fields while the subscript Y is related to the conserved quantum numbers,the *weak hypercharge*. The weak hypercharge is defined from the formula:

$$Q = I_z + \frac{1}{2}Y \tag{1.7}$$

where $I_Z$ is the third component of the weak isospin and Q is the electric charge. As we will see later the field associated $B^\mu$ with the $U(1)$ symmetry group does not correspond directly to the electromagnetic interaction.

Elementary particles are grouped in three families with increasing mass:
**Leptons**

$$\begin{pmatrix} e \\ \nu_e \end{pmatrix} \begin{pmatrix} \mu \\ \nu_\mu \end{pmatrix} \begin{pmatrix} \tau \\ \nu_\tau \end{pmatrix} \tag{1.8}$$

**Quarks**

$$\begin{pmatrix} u \\ d \end{pmatrix} \begin{pmatrix} c \\ s \end{pmatrix} \begin{pmatrix} t \\ b \end{pmatrix} \tag{1.9}$$

The interaction among the particles is derived by the gauge invariance principle. The gauge symmetry implies the existence of two coupling constants ($g$ and $g'$) and four gauge fields related with the generators of the EW symmetry group. $W_i^\mu$ ($i = 1, 2, 3$) are the three fields associated to $SU(2)$ while $B^\mu$ associated with $U(1)$. The $W^\mu$ fields couple with only left-handed spinors while $B^\mu$ couples in the same way to right-handed and left-handed spinors. The combination of the first two component of $W_i^\mu$ are associated with two charged vector boson $W^\pm$.

$$W^\pm = \frac{1}{\sqrt{(2)}} \left(W_1^\mu \mp W_2^\mu\right) \tag{1.10}$$

The third component $W_\mu^3$, mixes with the $B^\mu$ via the Weinberg angle $\theta_W$ [2] in order to form two neutral bosons: the photon and the $Z$.

$$\begin{pmatrix} W_3^\mu \\ B^\mu \end{pmatrix} = \begin{pmatrix} \cos\theta_w & \sin\theta_w \\ \sin\theta_w & \cos\theta_w \end{pmatrix} \begin{pmatrix} Z^\mu \\ A^\mu \end{pmatrix} \tag{1.11}$$

In gauge theories the mass of the gauge boson is zero while their masses have been measured and found to be 80 and 91 GeV respectively. The inclusion of the mass into a gauge theory is nontrivial, as gauge boson mass terms of the form $M^2 V^\mu V_\mu$ (introduced by hand) would break the local gauge invariance. To solve this problem, the gauge theory must be spontaneously broken.

## 1.2 Higgs Sector

As discussed before, the strong, weak and electromagnetic interactions are described in a local gauge invariant theory $SU(3) \otimes SU(2)_L \otimes U(1)_Y$. The SM Lagrangian cannot accommodate explicit mass term, without spoiling the electroweak gauge invariance. In order to introduce explicit mass term a spontaneous symmetry breaking (SSB) is needed. This mechanism was propose independently by Higgs, Engler, Brout [4, 5, 6]. The presence of the Higgs boson has been independently confirmed by ATLAS [7] and CMS [8] experiments at CERN in July 2013. This discovery allowed to Higgs and Englert to get the Nobel prize in 2013 [9].

In the EW context the SSB is introduced by considering a doublet of complex scalar fields $\Phi(x)$ and a scalar potential $V(\Phi)$ given by e.g.:

$$\Phi(x) = \begin{pmatrix} \phi^+(x) \\ \phi^0(x) \end{pmatrix} \tag{1.12}$$

$$V(x) = \mu^2 \phi^+ \phi^0 + \lambda \left(\phi^+ \phi^0\right)^2 \tag{1.13}$$

The Electroweak Lagrangian is invariant under the $SU(2)_L \otimes U(1)_Y$ transformation and can be written as

$$L = (D_\mu \phi)^\dagger (D^\mu \phi) - V(\phi^\dagger \phi) \tag{1.14}$$

with

$$V(\phi^\dagger \phi) = \mu^2 \phi^\dagger \phi + \lambda (\phi^\dagger \phi)^2 \tag{1.15}$$

The covariant derivative can be written:

$$D_\mu = \partial_\mu - ig\frac{\sigma}{2} \cdot \mathbf{W}_\mu - ig'\frac{Y}{2} \cdot \mathbf{B}_\mu \tag{1.16}$$

The existence of minima is guaranteed by taking $\lambda > 0$. The usual choice of $\mu^2 > 0$ gives a mass term for $\Phi$ and implies a trivial minimum of the potential al $\Phi = 0$. If one chooses $\mu^2 < 0$ the minimum obeys the condition:

$$< 0|\Phi|0 >= \begin{pmatrix} 0 \\ \nu/\sqrt{2} \end{pmatrix} \tag{1.17}$$

with $\nu = \sqrt{-\frac{\mu^2}{2\lambda}} > 0$ where the ground state of $\Phi^+$ was chosen to be zero.

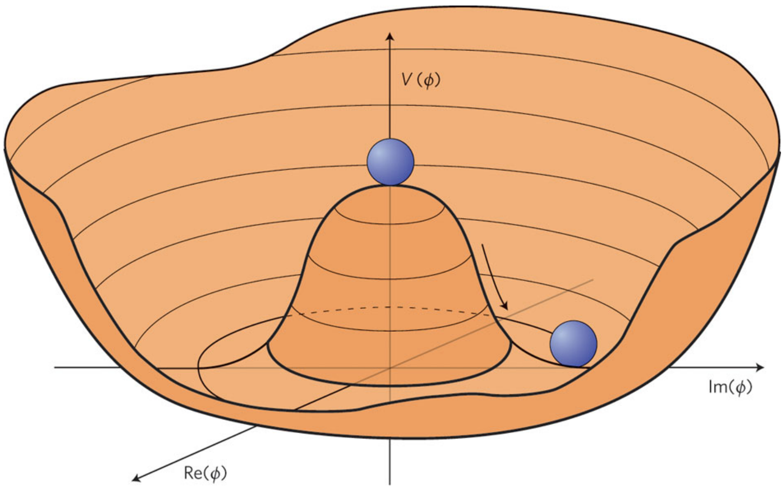


FIGURE 1.1: Illustration of the Higgs potential for a scalar fields with $\mu^2 < 0$

Although the Lagrangian remains invariant under $SU(2)_L \otimes U(1)_Y$ transformation, the choice of a particular value of the ground state breaks the symmetry. The choise is now to develop the theory around a point of minimum, writing the doublet as a function of a real field.

$$\Phi = \frac{1}{\sqrt{2}} \begin{pmatrix} 0 \\ \nu + \phi \end{pmatrix} \tag{1.18}$$

where $\phi$ is the real fields i.e. the displacement from vacuum state. The resulting kinetic term for the scalar fields, taking into account that $Y = 1$ for the Higgs field is

$$\begin{aligned} L_{kin} =& (D_\mu \phi)^\dagger (D^\mu \phi) \\ =& \left| \left\{ \partial_\mu - \frac{ig}{\sqrt{2}} \begin{bmatrix} W_\mu^3 & W_\mu^1 - iW_\mu^2 \\ W_\mu^1 + iW_\mu^2 & W_\mu^3 \end{bmatrix} \right\} - \frac{ig'}{\sqrt{2}} B_\mu \frac{1}{\sqrt{2}} \begin{bmatrix} 0 \\ \nu + \phi \end{bmatrix} \right|^2 \end{aligned} \tag{1.19}$$

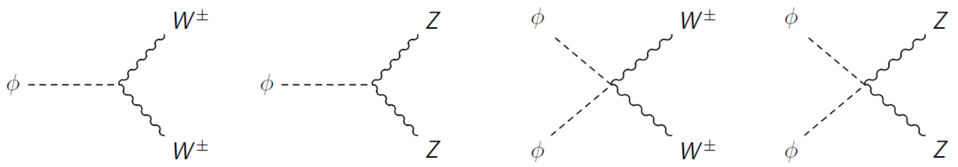


FIGURE 1.2: Feynman graph for Higgs sector

Taking into account equation 1.10 we obtain:

$$\begin{aligned} L_{kin} =& \frac{1}{2}\partial_\mu\phi\partial^\mu\phi + \left(\frac{g\nu}{2}\right)^2 W^-W^+ + \frac{1}{2}\left(\frac{g\nu}{2\cos\theta_W}\right)^2 Z^2 + \\ & \frac{g^2\nu}{2}\phi W^-W^+ + \frac{1}{4}\frac{g^2\nu}{\cos^2\theta_W}\phi Z^2 + \left(\frac{g}{2}\right)^2\phi^2 W^+W^- \\ & + \frac{1}{2}\left(\frac{g}{2\cos\theta^W}\right)^2\phi^2 Z^2 \end{aligned} \tag{1.20}$$

We can identify two mass terms:

$$m_W = \frac{g\nu}{2} \qquad\qquad m_Z = \frac{g\nu}{2\cos\theta_W} = \frac{m_W}{\cos\theta_W} \tag{1.21}$$

The potential 1.15 can be expressed as

$$\begin{aligned} V(\Phi) &= \frac{\lambda}{4}(\nu+\phi)^4 - \frac{\mu^2}{4}(\nu+\phi)^2 \\ &= const + 2\mu^2\phi^2 + 2\sqrt{2}\frac{\mu}{\sqrt{\lambda}}\phi^3 + \lambda\phi^4 \end{aligned} \tag{1.22}$$

where

$$m_H = \sqrt{2}\mu \tag{1.23}$$

where the cubic and 4th order terms in $\phi$ are the Higgs self-interaction terms. Fermions acquire mass through a Yukawa coupling:

$$L_f = -\frac{1}{2}(\nu+\phi)\lambda_f \bar{f} f \tag{1.24}$$

The coupling between fermions and the Higgs Boson $\lambda_f$ is arbitrary. They are related to the fermion mass via $m_f = \lambda_f \frac{\nu}{\sqrt{2}}$ which are free parameters of the theory

## 1.3 Standard Model

Combining the electroweak theory , the QCD and the Higgs mechanism one obtains a model that well describes the elementary particles and their interactions. As said before the constituents of matter can be grouped in two families, fermions and bosons. Bosons (Table. 1.1) carry the fundamental forces, while fermions are the constituents of known matter in the Universe. Fermions are divided into two main families, leptons (Table. 1.2) and quarks (Table. 1.3), both divided into three generations. Quarks and fermions acquire mass through the same mechanism as the gauge fields but this time the mass are free parameters.

| Interaction | Boson | Mass [GeV] | Electric charge |
|---|---|---|---|
| Eletromagnetic | $\gamma$ | 0 | 0 |
| Weak | W | $80.385 \pm 0.015$ | $\pm 1$ |
| | Z | $91.1876 \pm 0.0021$ | 0 |
| Strong | g | 0 | 0 |

TABLE 1.1: Stardard Model Bosons Properties [10]

| Lepton | Mass | Electric charge |
|---|---|---|
| Electron (e) | 0.511 MeV | -1 |
| e-neutrino ($\nu_e$) | $< 2$ eV | 0 |
| Muon ($\mu$) | 105.7 MeV | -1 |
| $\mu$-neutrino ($\nu_\mu$) | $< 1.9$ eV | 0 |
| Tau ($\tau$) | 1776.8 MeV | -1 |
| $\tau$-neutrino ($\tau$) | $< 18.2$ eV | 0 |

TABLE 1.2: Leptons Properties[10]

| Quark | Mass | Electric charge |
|---|---|---|
| Up (u) | $2.3^{+0.7}_{-0.5}$MeV | $+\frac{2}{3}$ |
| Down (d) | $4.8^{+0.7}_{-0.3}$ MeV | $-\frac{1}{3}$ |
| Charm (c) | $95 \pm 5$ MeV | $+\frac{2}{3}$ |
| Strange (s) | $1.275 \pm 0.025$ GeV | $-\frac{1}{3}$ |
| Top (t) | $173.5 \pm 0.7$ GeV | $+\frac{2}{3}$ |
| Bottom (b) | $4.18 \pm 0.03$ GeV | $-\frac{1}{3}$ |

TABLE 1.3: Quarks Properties[10]

Quarks interact also through the weak interaction. One particularity is that the mass eigenstates of quarks are different from the eigenstates of the weak interaction. To conserve the universality of the electroweak even in the quark sector, Nicola Cabibbo introduced a concept that later led to CKM (Cabibbo-Kobayashi-Maskawa) matrix (Equation 1.25).

$$\begin{pmatrix} |d'\rangle \\ |s'\rangle \\ |b'\rangle \end{pmatrix} = \begin{pmatrix} |V_{ud}| & |V_{us}| & |V_{ub}| \\ |V_{cd}| & |V_{cs}| & |V_{cb}| \\ |V_{td}| & |V_{ts}| & |V_{tb}| \end{pmatrix} \begin{pmatrix} |d\rangle \\ |s\rangle \\ |b\rangle \end{pmatrix} \tag{1.25}$$

The square of $V_{ij}$ is the probability that the i (u,c,t) quark decay into an j (d,s,b) quark. Mathematically, it connects a vector of down-like quark mass eigenstates to a vector of the down-like interaction partners of the up-like quarks. Requiring unitarity, the $V_{CKM}$ matrix can be represented with three angle ($\theta_{12}$,$\theta_{23}$,$\theta_{13}$) and one CP-violating phase $\delta_{13}$. The CKM matrix in general has a complex phase $e^{i\delta}$ where $\delta$ is the Kobayashi-Maskawa phase [11] which is responsible for all CP violating phenomena in flavor changing processes in the Standard Model [12]. CP violation was Kobayashi's and Maskawa's initial motivation for an expansion of the original $2 \times 2$ Cabbibo matrix.

Summarizing the SM describes very well known matter but it has 18 free real parameters to be determined by experiments.

- 9 Fermion mass $\rightarrow$ ($m_e$,$m_\mu$,$m_\tau$,$m_u$,$m_d$,$m_s$,$m_c$,$m_t$,$m_b$)
- 4 CKM parameters
- 3 coupling $g, g', \alpha_s$
- 2 parameters for scalar sector

## 1.4 Higgs Measurement

On the 4th of July, 2012 the discovery of a new boson compatible with the SM Higgs boson, was announced at CERN [13]. The discovery was made at the same time both by CMS and by ATLAS.In this section theoretical constraints, previous direct searches by LEP and Tevatron and indirect limits from Electroweak data are presented.

- **Theoretical constraints**
  Extending the validity of the SM beyond the energies for which it has been tested imposes some limits on the Higgs mass.
  *The $W^+W^- \rightarrow W^+W^-$ scattering*, which involves the quadratic gauge coupling and exchanges of the Z, $\gamma$ and possibly the Higgs Boson. If the boson is too heavy or does not exist, the unitarity is violated unless some new physics appears at the scale of 1 TeV, or if the Higgs is lighter than approximately 800 GeV.
  *The Triviality bound* set a stronger upper limit to the Higgs mass. Assuming a scalar sector of the SM is a $\phi^4$ theory, it remains valid as long as the Higgs quartic coupling is finite. As this coupling is expected to increase with energy, a cut-off $\Lambda$ must be set, after which some new physics taken over. If the SM is restricted to the electroweak scale ($\Lambda \sim 1 \times 10^3$ GeV) the Higgs could have mass up to 1 TeV. If its validity extends to the GUT scale ($10^{16} GeV$) masses above 200 GeV are not allowed.
  *The Stability bound* set a lower limits in the mass of the Higgs. For a low mass Higgs the self-coupling loops with fermions and gauge bosons must be included. The major contributions comes from the top quarks and contributes with a negative sign. If $M_H$ is too low, the sign of the quartic term in the scalar potential is flipped and there is not minima anymore.

  Combining all these effect, the theoretical limits on the Higgs mass are represented in Fig. 1.3. While an lower limit is set by the vacuum stability bound.

- Before LHC the most stringest limits came from direct search of the Higgs Boson at Tevatron 1.5 and LEP(Fig. 1.4 ). The initial phase at the energy of the Z pole of LEP, excluded the mass range below 65.2 GeV. The upgraded LEP2 increases the center of mass energy up to 209 GeV, looking the "Higgs-strahlung" production ($e^+e^- \rightarrow Z^* \rightarrow HZ$). The exclusion limits for $m_H < 114.4$ GeV was set to 95% confidence level (CL). The Tevatron

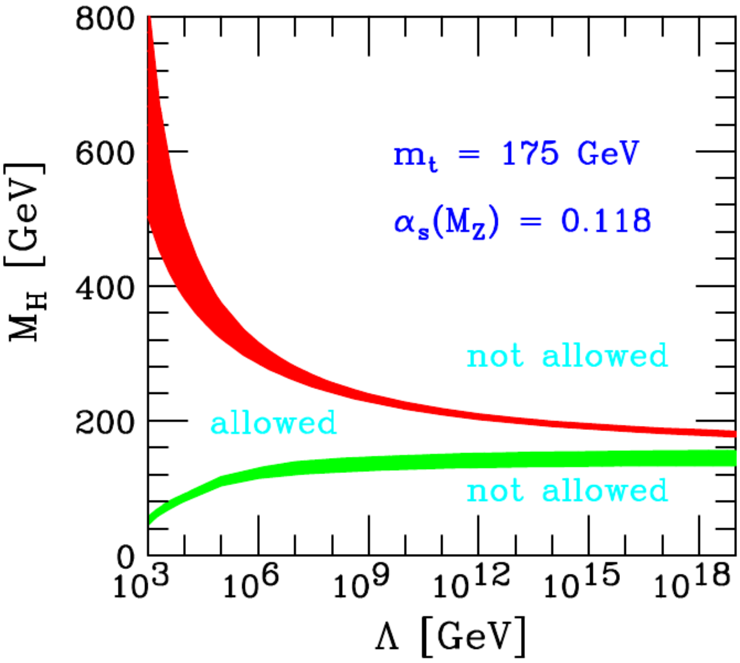


FIGURE 1.3: Theoretical limits on the Higgs boson mass from the triviality (upper bound) and vacuum stability arguments (lower bound), as a function of the cut-off $\lambda$. The allowed region lies between the bands and the colored/shaded bands illustrate the impact of various uncertainties. Extracted from ref. [14].

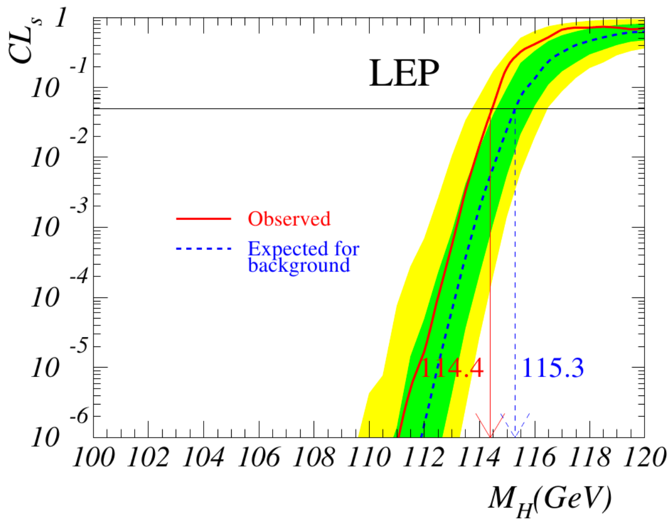


FIGURE 1.4: Confidence level of signal plus background hypothesis on the Standard Model Higgs boson searches at LEP. Masses below 114.4 GeV, defined by the intersection of the horizontal line at CL s = 0.05 with the observed curve are excluded at 95%CL. Ref [15]

operates a t $\sqrt{s} = 1.96TeV$ colliding $p\bar{p}$ until 30 September 2011. Using the $10fb^{-1}$ and combining the results from the two experiments, CDF and $DØ$ the excluded regions at 95 % CL is between 100 and 103 GeV and betweem 147 and 180 GeV.

- The stringest limits from the electroweak precision data come from the LEP Electroweak Working Group [17] and more recently from the GFitter toolkit [18]. Two many results are provided, including or not the constrain from the direct measurements of the Higgs Boson

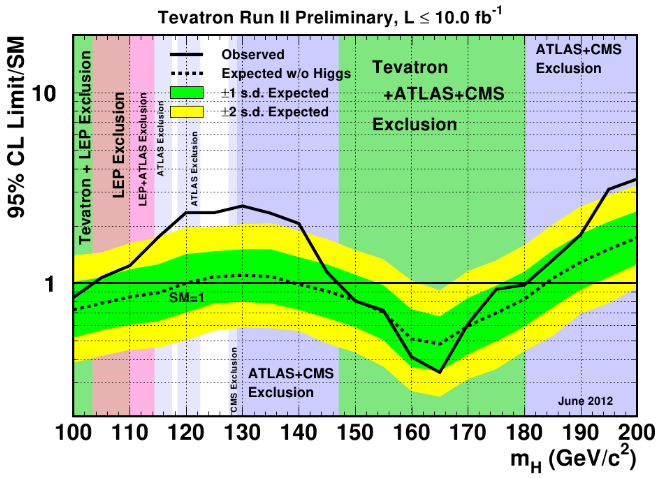


FIGURE 1.5: Observed and expected 95% CL upper limits on SM Higgs boson production at the Tevatron. Masses between 100 and 103 GeV, and between 147 and 180 GeV, for which the observed curve lies below 1, are excluded at 95% CL. From [16]

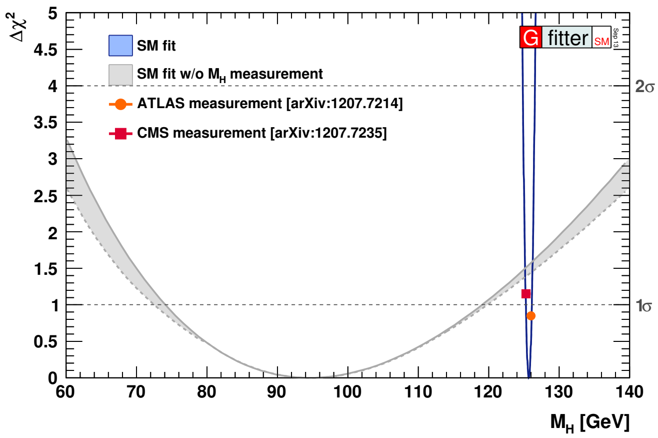


FIGURE 1.6: $\Delta\chi^2$ as a function of Higgs boson mass $M_H$, shown as blue band. Also shown is the result of the fit without the $M_H$ measurements (grey band). The solid and dashed lines give the results when including and ignoring theoretical errors, respectively.

from ATLAS and CMS.

$$\begin{aligned} \text{Electroweak precision data only:} M_H &= 94^{+24}_{-22} GeV \\ \text{Including direct searches:} M_H &= 125.7 \pm 0.4 GeV \end{aligned} \tag{1.26}$$

- In July 2012, an observation of a new particle in the search of the Standard Model Higgs Boson was perform [7]. Using the datasets correspond to integrated luminosities of 4.8 $fb^{-1}$ collected at $\sqrt{7}$ TeV in 2011 and 5.8 $fb^{-}1$ collected at $\sqrt{8}$ TeV in 2012, clear evidence for the production of neutral boson with a measured mass of $126.0 \pm 0.4(\text{stat}) \pm 0.4(\text{syst})$ was shown. This measurement combine the individual research in $H \to ZZ^* \to 4l$, $H \to \gamma\gamma$ and $H \to WW^* \to e\nu\mu\nu$ channels in the 8 TeV data and $H \to ZZ^*, \gamma\gamma, WW^*, b\bar{b}$ and $\tau^+\tau^-$ in the 7 TeV data. This observation, which has a significance of 5.9 standard deviations, corresponding to a background fluctuation probability of $1.7 \times 10^{-9}$. This observation(Fig. 1.7) is compatible with the production and decay of the Standard Model Higgs boson.

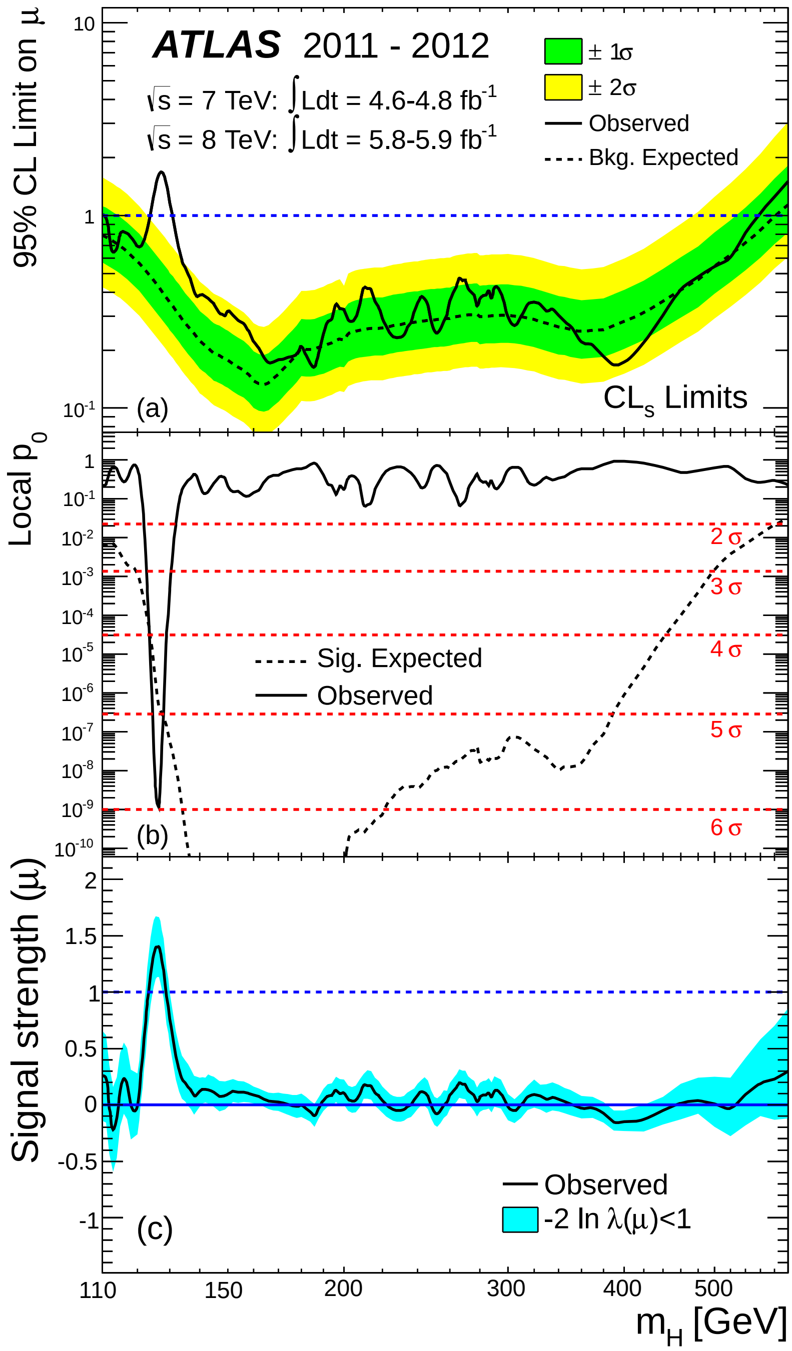


FIGURE 1.7: Combined search results: (a) The observed (solid) 95% CL upper limit on the signal strength as a function of $m_H$ and the expectation (dashed) under the background-only hypothesis. The dark and light shaded bands show the plus/minus one sigma and plus/minus two sigma uncertainties on the background-only expectation. (b) The observed (solid) local $p_0$ as a function of $m_H$ and the expectation (dashed) for a SM Higgs boson signal hypothesis ($\mu = 1$) at the given mass. (c) The best-fit signal strength muhat as a function of $m_H$. The band indicates the approximate 68% CL interval around the fitted value.[7]

## 1.5 Higgs Production

Though the SM does not predict the mass of the Higgs boson, it does predict how the Higgs can be produced and how it can decay. At pp colliders as the LHC, the mechanism with the highest probability to produce a SM Higgs is gluon-gluon fusion, represented in Figure 1.8a, where a Higgs is produced from a top-quark loop created by a pair of gluons. The second most abundant is VBF, plotted in Figure 1.8b, where colliding quarks emit a pair of weak bosons that decay into a Higgs. The quarks are expected to give rise to very energetic jets located in the forward region, with a large rapidity gap between them. The next most abundant process is Higgstrahlung (the associated production with a weak boson, plotted in Figure 1.8c, where a produced weak boson (either $W^{\pm}$ and $Z^0$) radiates a Higgs. The decay of the vector bosons to leptons (including neutrinos) provide good trigger efficiency and help reducing QCD background. Finally, the last process is represented by Feynman diagram in Figure 1.8d, is the associated production with a top-antitop quark pair.

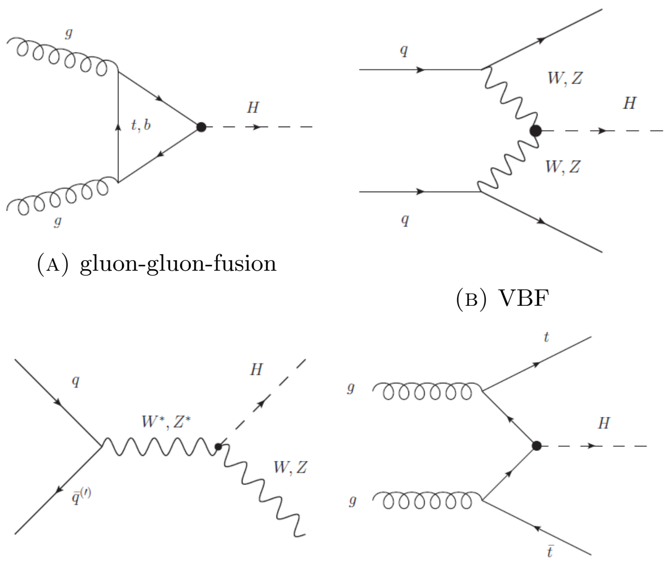


(A) gluon-gluon-fusion

(B) VBF

(C) Associated production

(D) top-antitop production

FIGURE 1.8: Higgs Production Modes

The branching ratio change rapidly with Higgs boson mass. Their values fro a Higgs mass boson of 125 GeV are summarized in Table 1.4. The cross sections for each of these production mechanisms depends on Higgs mass, with cross section decreasing with mass, as shown in Figure 1.9. All the cross sections presented are provided by the LHC Higgs Cross Section Working Group [19].

## 1.6 Decay Modes

The Higgs boson couples to any massive particle, though the strength of the coupling is directly proportional to mass. For this reason, the Higgs (of any mass) decays mostly to the heaviest kinematically accessible particle pair. Thus, as shown in Figure 1.10, lower mass Higgs ($<$ 135

| Decay | Branching Ratio | QCD | EW |
|---|---|---|---|
| $H \to t\bar{t}$ | $< 5 \cdot 10^{-8}$ | $\sim 5\%(NLO)$ | $< 2 - 5\%(NLO)$ |
| $H \to b\bar{b}$ | $5.78 \cdot 10^{-1}$ | $0.1 - 0.2\%(NNLO)$ | $1 - 2\%(NLO)$ |
| $H \to c\bar{c}$ | $2.68 \cdot 10^{-2}$ | $0.1 - 0.2\%(NNLO)$ | $1 - 2\%(NLO)$ |
| $H \to \tau\tau$ | $6.37 \cdot 10^{-2}$ | - | $1 - 2\%(NLO)$ |
| $H \to gg$ | $8.6 \cdot 10^{-2}$ | $10\%(NNLO)$ | $1\%(NLO)$ |
| $H \to \gamma\gamma$ | $2.30 \cdot 10^{-3}$ | $< 1\%(NLO)$ | $1\%(NLO)$ |
| $H \to WW$ | $2.16 \cdot 10^{-1}$ | $0.5\%(NLO)$ | $\sim 0.5\%(NLO)$ |
| $H \to ZZ$ | $2.67 \cdot 10^{-1}$ | $0.5\%(NLO)$ | $\sim 0.5\%(NLO)$ |

TABLE 1.4: Main branching ratios for a standard model Higgs boson at mH = 125 GeV in fermionic and bosonic final states and the associated systematic uncertainties coming from missing higher orders QCD and EW terms [19]. The highest orders reached for the partial width are indicated.

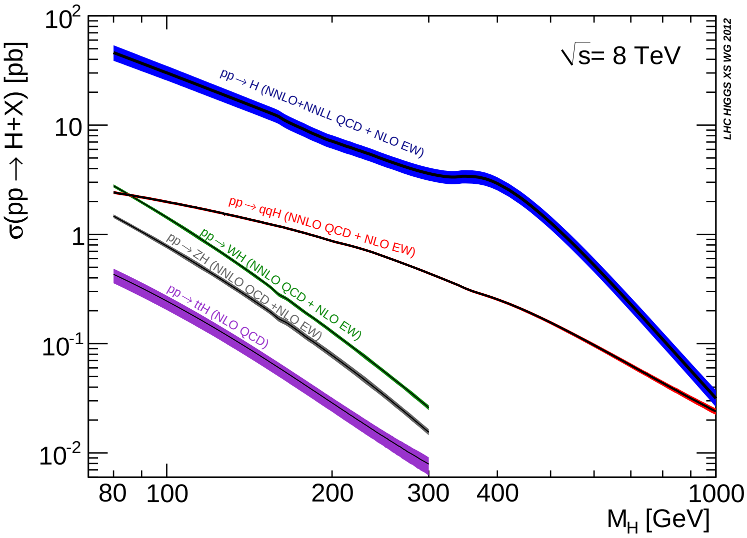


FIGURE 1.9: Higgs production

GeV) prefers $H \to b\bar{b}$ decays, whereas heavier Higgs prefer $H \to W^+W^-$. The width, $\Gamma$, of the Higgs Boson (which is inversely proportional to the life-time $\tau$), can be seen in Fig. 1.11. At the mass where it is observed, around 126 GeV, the width is so small that the detector resolution dominates the observed width. In this region there is a variety of different decay channel available,as can be appreciated int Fig. 1.10.

### 1.6.1 $H \to \gamma\gamma$

In the Standard Model the coupling of the Higgs with two photons occurs through top loop and W-boson loops. This channel provides a clean signature to LHC with two isolated photons with a high transverse momentum. The partial width for the decay into photons is [20], [21]:

$$\Gamma = [H \to \gamma\gamma] \frac{G_F \alpha^2 m_H^3}{128\sqrt{2}\pi^3} \left| \sum_f N_c Q_f^2 F_{1/2}^H(\tau_f) + F_1^H(\tau_W) \right|^2 \tag{1.27}$$

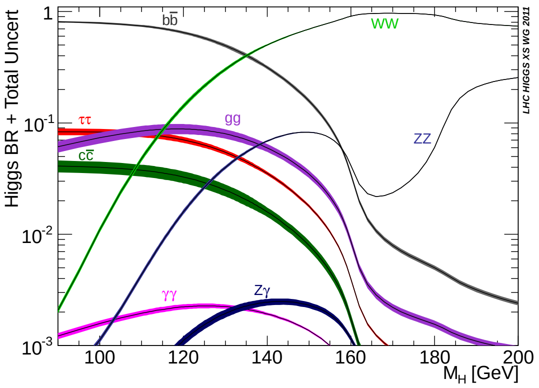


FIGURE 1.10: The SM Higgs branching ratios as a function of Higgs mass MH.

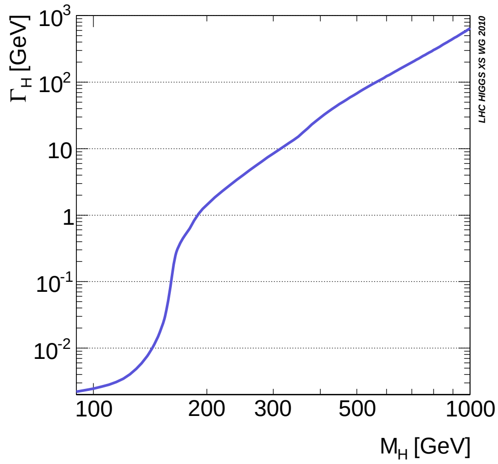


FIGURE 1.11: The predicted width of the SM Higgs boson as a function of its mass [19].

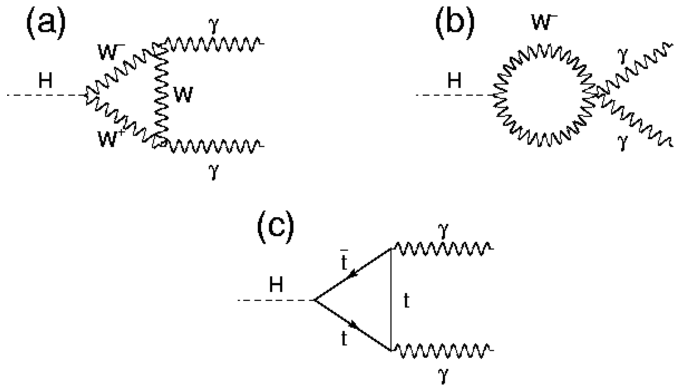


FIGURE 1.12: Higgs Feynman diagram couples with two photons.

where $Q_f$ is the charge of the fermion. The squared term corresponds to form factors that depends on the spin of the particle in the loop:

- $F^H_{1/2}(\tau_f)$ for the spin (fermions, mainly the top quark)
- $F^H_1(\tau_W)$ for spin 1 (W boson)

These form factor are function of $\tau_i$ with $\tau_i = \frac{m_H^2}{4m^i}$ and $i = f, W$.

$$F^H_{1/2}(\tau_f) = 2[\tau + (\tau - 1)f(\tau)]\tau^{-2}$$
$$F^H_1(\tau_f) = 2[2\tau^2 + 3\tau + 3(2\tau - 1)f(\tau)]\tau^{-2}$$

with the function as $f(\tau)$ defined as:

$$f(\tau) = \begin{cases} \arcsin^2\sqrt{\tau} & \tau \leq 1 \\ -\frac{1}{4}[\log[\frac{1+\sqrt{1-\tau^{-1}}}{1-\sqrt{1-\tau^{-1}}} - i\pi]]^2 & \tau \geq 1 \end{cases}$$

# Chapter 2

# The ATLAS detector at the LHC

In this chapter an introduction to LHC collider [22] and its physics environment is given, together with a description of the ATLAS detector [23]:A particular emphasis will be given to the characteristics of the ATLAS electromagnetic calorimeter.

## 2.1 LHC

The LHC (Large Hadron Collider) is a proton-proton(and heavy-ions) collider machine based at CERN near Geneve. This machine uses the 27 km tunnel, located underground between 50 m and 175 m depth, that was built between 1984 and 1989 for the LEP machine. In 2000, LEP was dismissed to give way to the LHC. The approval of the LHC project has been given in December 1994, by the CERN Council [24]. During the years of ATLAS data taking it has worked in increasing energy, starting from the center of mass energy of 7 TeV in 2011 to 8 TeV during 2012.

The LHC, pictured in Figure 2.1, is a two-ring synchrotron particle accelerator. Its 1232 dipole magnets bend the beams into its circular orbit, whereas its 392 quadrupole magnets focus the beams. The dipoles magnetic field required to bend the proton path is 8.3 T. The resulting current and material requirements are beyond the capabilities of traditional electromagnets, thus, NbTi superconducting magnets that operate at 1.9 K are used instead. This is accomplished by using an elaborate cryogenics system, with liquid helium cooling the magnets to their operating temperature. A succession of small to large accelerators is used to accelerate the protons to the energy needed for injection into the LHC. Protons are first accelerated through LINAC 2 up to 50 MeV and then pass to PSB where the beams reach to 1.4 GeV. The last two steps are the PS (Proton Synchrotron) and the SPS (Super Proton Synchrotron). The injection of the particle beam in the LHC occurs at an energy of 450 GeV. The beams are injected in bunches with a length corresponding to 1.71 ns (reduced to 1.06 ns for collisions) and nominally spaced by 25 ns. During the 2011-12 data taking the beams were spaced by 50 ns.

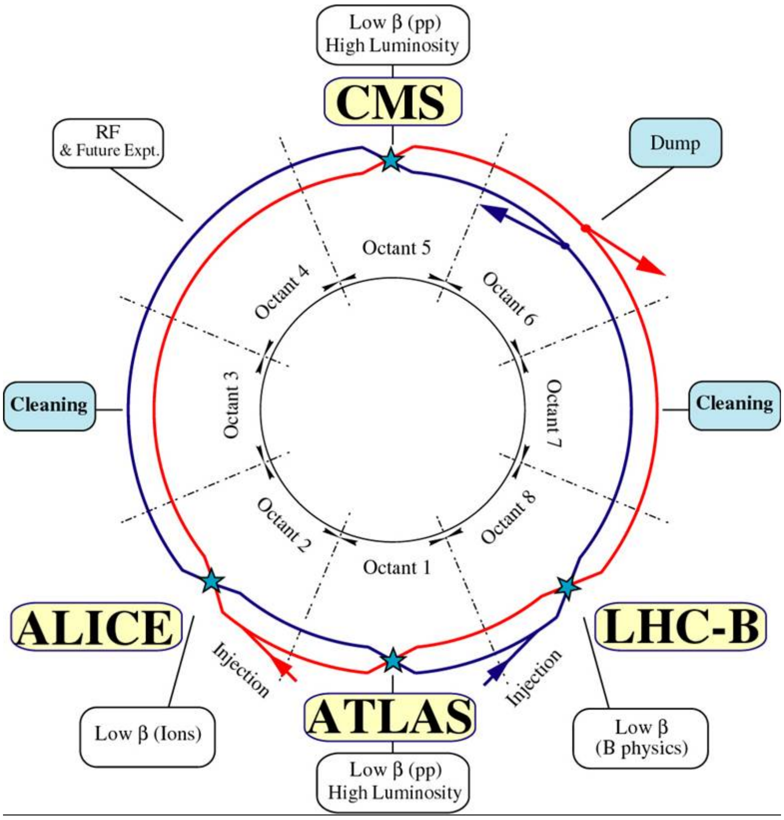


FIGURE 2.1: Schematic layout of the LHC.[25]

### 2.1.1 Luminosity

A measurement of intensity of the beam is *luminosity*, depending only on parameters of the beam:

$$L = \frac{N_b^2 n_b f_r \gamma_r}{4\pi\epsilon_n \beta^*} \tag{2.1}$$

where (nominal parameters for the LHC are given in parenthesis):

- $N_b$ is the numbers of particle per bunch ($\sim 10^{10} - 10^{11}$),
- $n_b$ is the number of bunch per beam (2808),
- $f_r$ is the revolution frequency (11245 Hz),
- $\gamma_r$ the relativistic gamma factor ($\sim$7000),
- $\epsilon_r$ the normalized traverse beam emittance (3.75 $\mu m$),
- $\beta^*$ is the beta function at the ATLAS collision point (0.55m)

The luminosity is related to the number of events of a given type production each second:

$$N_{event} = \sigma_{event} \cdot L \tag{2.2}$$

where $\sigma_{event}$ is the cross section of the considered process. A rare process can be observed only after accumulating a large amount of integrated luminosity. In Figure 2.2 are represented the

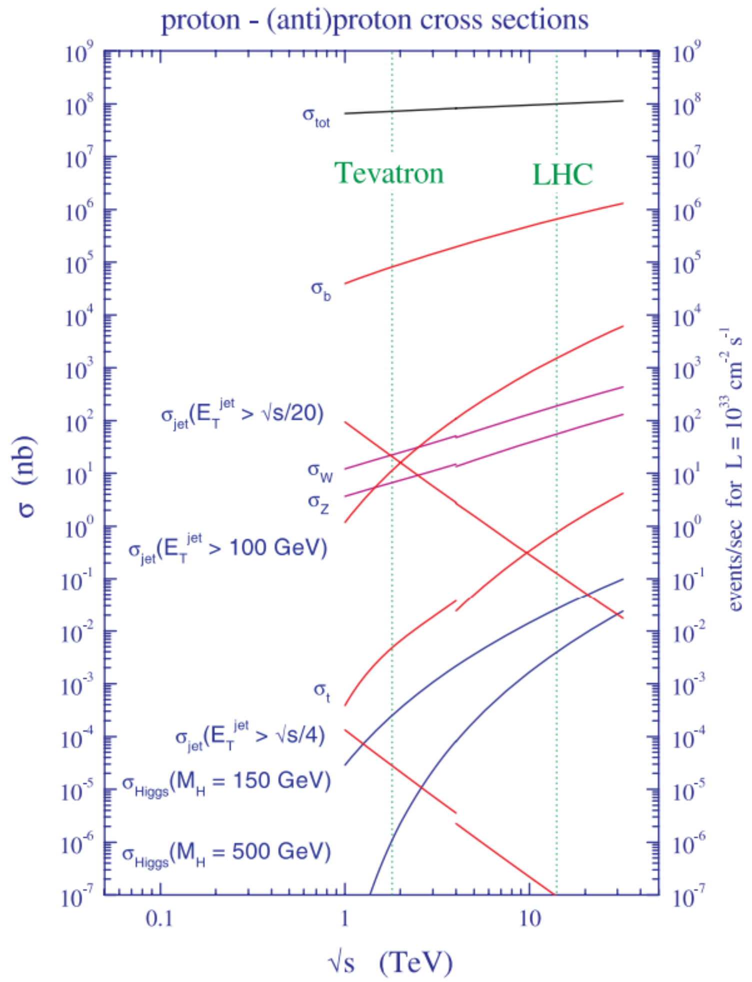


FIGURE 2.2: Standard model cross sections at the Tevatron and LHC colliders. [29]

cross section for different process in function of the center of mass energy. For the purpose of gathering the information about what happened in the collisions, four detectors are built at the collision points, as illustrated in Figure 2.1. These are ALICE (A Large Ion Collider Experiment) [26], ATLAS(A Toroidal LHC ApparatuS) [23], LHCb (Large Hadron Collider beauty experiment) [27] and CMS (Compact Muon Spectometer) [28]. ALICE is designed to primarily look at the heavy ion collisions that will take place in the LHC, to study the nature of quark-gluon plasma believed to exist in the very first fractions of time after the Big Bang. LHCb is specialized to look at hadrons containing the bottom quark to unveil the nature of CP-violation, to close in on the answer to the riddle of why there is such an asymmetry between matter and anti-matter in the universe. The ATLAS and CMS detectors are general purpose detectors, built to be able to discover a broad spectrum of possible new physics. They were both designed in such a way that, given the existence of the SM Higgs boson below 1 TeV, a discovery would be guaranteed. More details about the ATLAS detector, used in this thesis, will be given in the following section.

### 2.1.2 Run I

The first beam circulated in the LHC on September 10, 2008. Nine days later an incident was caused by a faulty electrical connection between two magnets during powering tests of the main dipole circuit [30] . Helium leakage into the tunnel and serious mechanical damage delayed the operations by about a year.

Repairs and consolidation work allowed the accelerator to resume its program in the end of 2009. The first collisions were achieved in November 23 and the world energy record was set one week later, with 1.18 TeV beams colliding at $\sqrt{s} = 2.36$ TeV. The research program started in March 30, 2010 with the LHC beam energy of 3.5 TeV. During 2011 LHC collected $\sim 4.7\,\text{fb}^{-1}$ at $\sqrt{s}$=7 TeV. During 2012 LHC delivered 20.3 $\text{fb}^{-1}$ at $\sqrt{s} = 8$ TeV. Figure 2.3 is the evolution of the

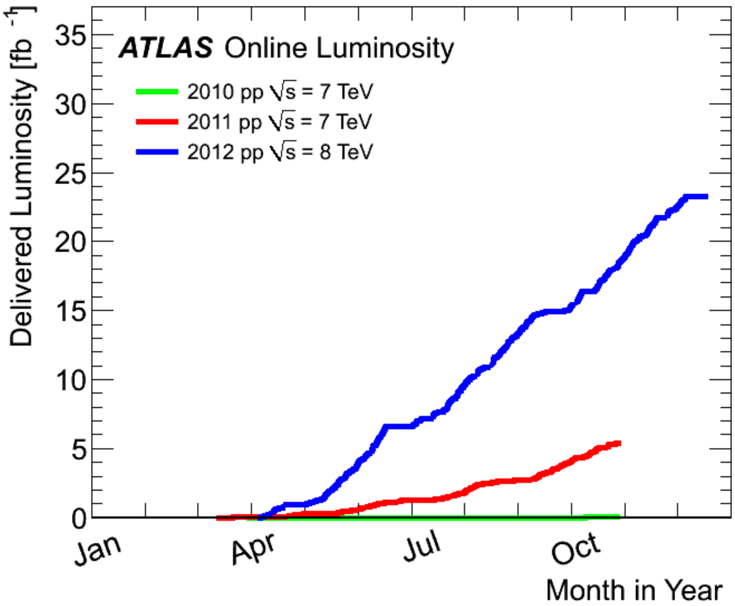


FIGURE 2.3: Delivered luminosity during the data taking years.

data taking. On December 17, 2012, LHC completed the *Run 1* data taking. The maximum instantaneous luminosity achieved during 2012 was $7.73 \times 10^{33} cm^{-2} s^{-1}$. Running will resume in 2015 with increased collision energy of 13 TeV.

## 2.2 ATLAS

The ATLAS (A Toroidal LHC ApparatuS) [31, 32, 33] is one of the two general purpose detectors at the LHC, and is the biggest one in volume. It is 25 meters high, 44 meters long and weighs about 7000 tonnes.

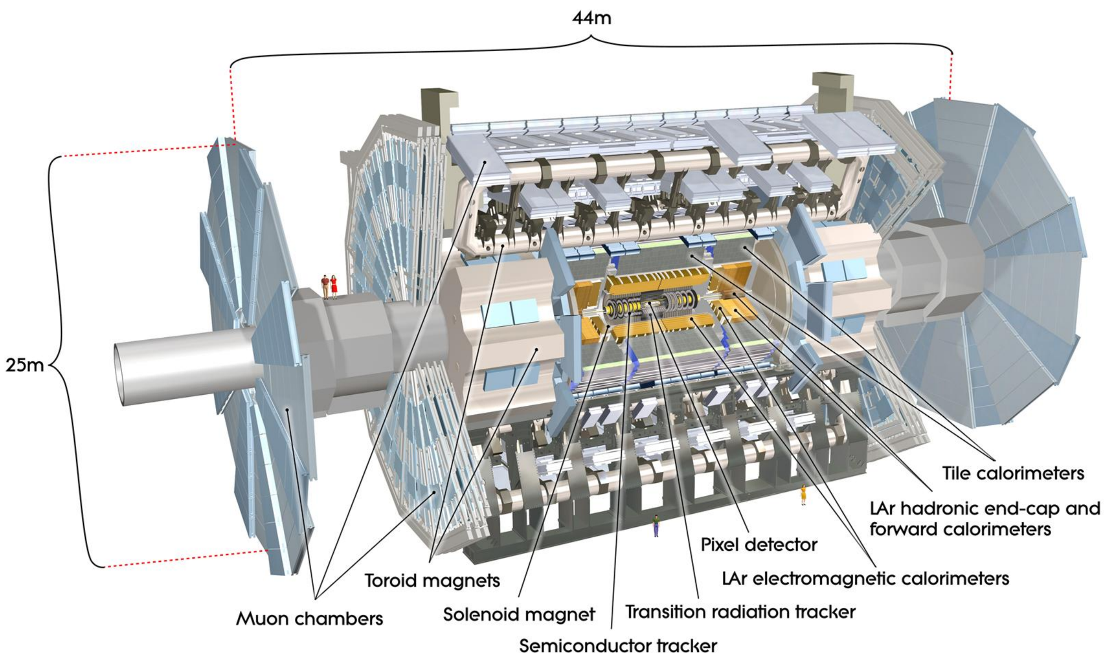


FIGURE 2.4: The ATLAS detector and its subdetectors.

The coordinates system of ATLAS, is a right-handed one, in which the z-axis points along the beam-pipe in the counterclockwise direction seen from above, the y-axis points upwards to the earth's surface and the x-axis points towards the center of the LHC ring. The azimuthal angle $\phi$ runs in the transverse plane around the beam-line. The polar angle $\theta$ is measured from beam-axis, but most commonly, the *pseudorapidity* $\eta$ is used instead.

$$\eta = -\ln\left[\tan\left(\frac{\theta}{2}\right)\right] \tag{2.3}$$

the difference of pseudorapidity of two particles is independent of the Lorentz boosts along the beam axis. The transverse momentum, $\vec{p}_T$, and the missing component, $\vec{p}_T^{miss}$ are defined in the x-y plane. The scalar magnitudes of $\vec{p}_T$ ($\vec{p}_T^{miss}$) are called $E_T(E_T^{miss})$. The distance in pseudorapidity-azimuthal angle space is defined as $\Delta R = \sqrt{\Delta\eta^2 + \Delta\phi^2}$.
The ATLAS detector is built up to layer of various subdetectors, each with its own purpose. The different components can be seen in Fig. 2.4.

## 2.3 Identifying Particles with the ATLAS Detector

ATLAS has an onion-like structure, with different layers of different kinds of detectors. I will shortly describe the various sub-detectors, but firstly I will address the motivation for such a structure. The purpose of the design is to be able to discriminate between different type of particles that cross the detector. An illustration of how the various particles are identified in the ATLAS detector is given in Fig. 2.5. The behavior of the most frequently produced stable particles through the layers of the detector are depicted.

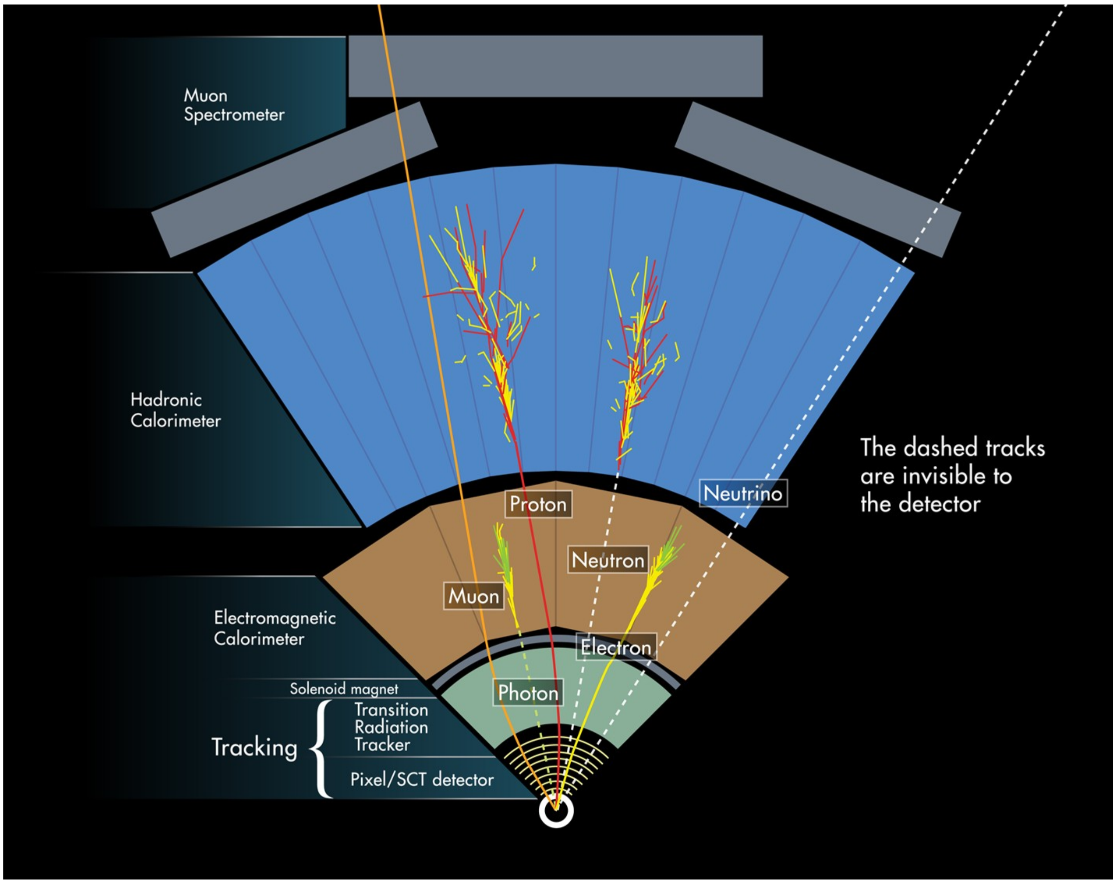


FIGURE 2.5: The identification of various particles with the use of the onion structure of the ATLAS detector

Charged particles, curved by the magnetic field, leave a track in the inner detector, indicated by full lines. Photons can convert into electron pair while crossing the inner detector therefore leaving only signs in some layers of the ID. Electrons and photons are fully stopped in the electromagnetic calorimeter, whereas hadrons, such as protons and neutrons, continue and deposit their energy also in the hadronic calorimeter. Muons, being minimum ionizing particles, leave a small amount of their energy in the detector, and make it through to the muon spectrometer.In the volume of the muon spectrometer they are curved by a toroidal magnetic field and are measured before they escape the detector. Dashed lines illustrate particles that do not interact with that part of the detector and are effectively invisible. Some particles escape the detector leaving no trace behind, as neutrinos – they can only be inferred by conservation of energy and momentum and show up as missing energy in some part of the detector.

## 2.4 The Inner Detector

The Inner Detector (ID) is the innermost detector and consist in three parts: the Pixel Detector, the microstrips tracker (SCT) and the transition radiation tracker (TRT). All these sub-detectors are immersed in a 2 T magnetic field produced by the solenoid magnets. The ID must provide excellent spatial resolution to make possible the reconstruction of the tracks and momentum of particles spanning a large energy domain. The inner detector will be subject to large doses of highly energetic particles, and must be radiation-hard in order to survive such a harsh environment: at design luminosity, it will see around 40 billion charged particles per second. Passive material in the ID must be minimized in order to avoid inducing particle shower, causing the objects to loose energy before the calorimeter. The resolution of the tracking parameter is given by:

$$\sigma\left(\frac{1}{p_T}\right) = a \oplus \frac{b}{p_T} \tag{2.4}$$

where the $\otimes$ indicates sum in quadrature. So one obtains:

$$\frac{\sigma\left(p_T\right)}{p_T} = a \cdot p_T \oplus b \tag{2.5}$$

where the constant $a$ is the intrinsic resolution of the detector, and $b$ arises from multiple scattering, dominating the resolution at low momentum.

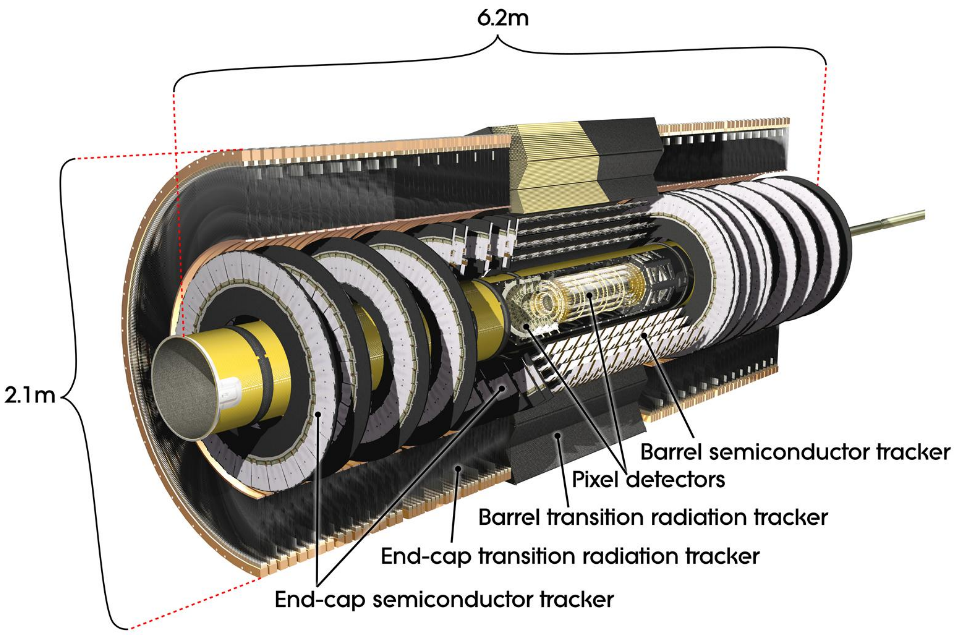


FIGURE 2.6: Cut-away view of the ATLAS Inner Detector

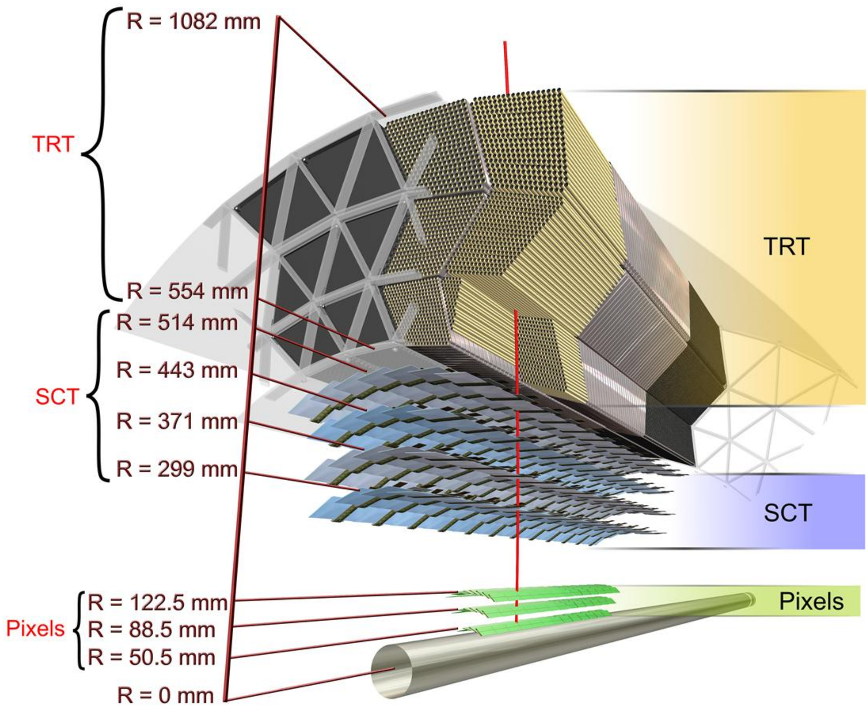


FIGURE 2.7: Illustration of the Inner Detector, for the barrel part

### 2.4.1 Pixel Detector

The first detector closest to the beam pipe is the Pixel Detector: it consist in a 1744 pixel sensors of $250\mu m$ thickness and dimensions $19 \times 63\,mm^2$. Each sensor has 46 080 read-out channels, thus making up more than 80.4 million read-out channels in total. The layer closest to the beam-line, at a radius of $5.05\,cm$, is called the *b-layer*. The other layers, at radii of 8.85 and 12.3 cm respectively, are called *layer 1* and *layer 2*. The end-cap disks are located at ±49.5, ±58.0 and ±65.0 cm along the z axis. The pixel layers have an intrinsic resolution of $10\,\mu m$ in the $R-\phi$ plane orthogonal to the beam axis ($z-\phi$ plane for the end-cap disks) and $115\,\mu m$ along z (R for the end cap disks). This detector is of fundamental importance in the identification of $b$-quark jets and reconstruction of secondary vertex from photon convertion.

### 2.4.2 Silicon Transition Tracker

After the Pixel Detector, the SCT completes the high precision tracking, with eight hits per tracks expected. The barrel consist in 4 cylindrical layers of modules of silicon microstrips, each made up by two sensor at a 40 mrad stereo angle in order to measure also the z coordinate. The pitch of the strips is about $40\mu m$. The endcap is made up by 9 disks. The intrinsic resolution of the STC is 17 $\mu m$in the $R-\phi$ and 580 $\mu m$ in $\eta$ and the total number of channels is approximately 6.3 milion.

### 2.4.3 Transition Radiation Tracker

The Transition Radiation Tracker surrounds the STC. It has been designed to provide large number of measured space-points and to enhance the electron identification capabilities in $|\eta| < 2$ region. It is made by straw tubes of about 4 mm diameter, that provide a large numbers of measured point ($\sim$ 30 hits). The TRT only provide $R - \phi$ information in the barrel region and $z - \phi$ information the endcap. In the barrel region the straw (4 mm diameter and 144 cm long) are disposed parallel to the beam axis. In the endcap region the 37 cm long straw are disposed radially in wheels. The total number of TRT readout channels is approximately 351000. The tubes are filled with non-flammable xenon-based gas (70% Xe,20% $CO_2$ and 10% $CF_4$).

## 2.5 The Calorimeters

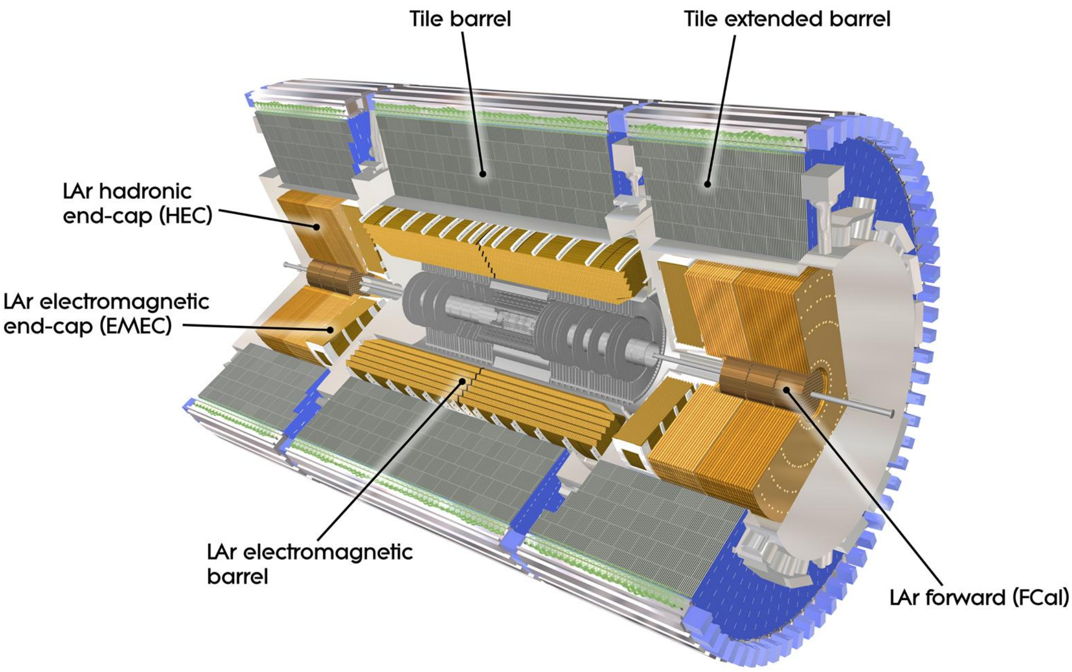


Figure 2.8: ATLAS Calorimeter

The calorimeters are located after the inner detector and used to measure electrons, photons and hadronic jets are reconstructed. Electrons and photons are identified in the liquid argon (LAr) electromagnetic calorimeters (EM) with excellent performance in terms of energy and position resolution. Liquid argon technology is also used in the detection of hadronic activity in the Hadronic End-cap Calorimeter (HEC) and in the Forward Calorimeter (FCal). The calorimeter is placed into a cryostat which also contains the inner solenoid. The end-caps cryostat contains all the end-caps calorimeter. The Hadronic calorimeter is complemented by a scintillator-tile detector of easier assembling and lower cost, extending up to $|\eta| < 1.7$. The general layout is shown in Figure 2.8. The total depth of the EM calorimeter exceeds 22 radiation lengths($X_0$) in the barrel region and 24 in the endcap. The hadronic calorimeter adds further 9.7 interaction lengths in the barrel region and 10 in the end-caps. The calorimeter resolution can be splitted in different term:

$$\frac{\sigma_E}{E} = \frac{a}{\sqrt{E}} \oplus \frac{b}{E} \oplus c \tag{2.6}$$

where E is the energy, a the stocastic (or sampling) term, b the noise term and c the constant term. The $\oplus$ correspond to the quadratic sum of the effects. The main contribution for the energy resolution for the electromagnetic and hadronic calorimeters are $\frac{10\%}{\sqrt{E}}$ and $\frac{40\%}{\sqrt{E}}$ respectively. More details about the electromagnetic calorimeter will be given in Chapter 3.

## 2.6 The Muon Spectrometer

The muon spectrometer surrounds the calorimeter. It is designed to detect and measure the momentum of charged particle than are not stopped by the calorimeters in the range $|\eta| < 2.7$. There are two different functions that muon chambers must accomplish: triggering and high precision tracking. The trigger system covers the region up to $|\eta| < 2.4$, and is composed by Resistive Plate Chambers (RPCs) in the barrel and Thin Gap Chamber (TGC) in the end-caps. The triggering system provides bunch-crossing identification (BCID), well-defined $p_T$ thresholds and a measurement of the muon coordinate in the direction orthogonal to the chambers dedicated to precision tracking.

The tracking is performed by the Monitored Drift Tubes (MDTs) and by Cathod Strips Chambers (CSCs) at large pseudorapidity. High precision mechanical assembly techniques and optical alignment systems provide the essential alignment of the chambers, while the magnetic field reconstruction relies on Hall sensors distributed throughout the spectrometer volume.

Different magnetic fields permit to perform the measure of the momentum.

- In the barrel region $|\eta| < 1.4$ is provided by the barrel toroid.
- For $1.4 < |\eta| < 1.6$ by a combination of barrel toroid and end-cap toroid fields.
- For $1.6 < |\eta| < 2.4$ by two end-cap toroids' fields.

The overall momentum resolution provided by the muon system is:

$$\begin{aligned} \frac{\sigma_{Pt}}{Pt} &= 4\% \text{ at } 50 \text{ GeV} \\ \frac{\sigma_{Pt}}{Pt} &= 11\% \text{ at } 1 \text{ TeV} \end{aligned} \tag{2.7}$$

# Chapter 3

# Calibration of the Electromagnetic Calorimeter

In this chapter, I will discuss the characteristics of the EM calorimeter with particular emphasis on photons reconstruction, identification and calibration. I will detail the calibration procedure, the main corrections and the systematics uncertainties on the energy scale.

## 3.1 Electromagnetic Calorimeter

The Electromagnetic Calorimeters are lead-liquid Argon detectors with accordion shaped absorbers and electrodes (Fig.3.1). This structure provides full-azimuthal coverage without crack regions. In the barrel, the accordion waves are parallel to the beam axis and their folding angle varies along the radius in order to keep the liquid Argon gap as constant as possible. In the electromagnetic endcaps, the accordion waves run axially and the folding angle varies with radius.

The Electromagnetic Calorimeter is longitudinally segmented in three layers in the region $0 < |\eta| < 2.5$. The cell granularity of the first layer is:

- $\Delta\eta \times \Delta\phi = 0.003 \times 0.1$ for $|\eta| < 1.4$
- $\Delta\eta \times \Delta\phi = 0.025 \times 0.0025$ for $1.4 < |\eta| < 1.475$
- $\Delta\eta \times \Delta\phi =$ 0.003-0.025 $\times$ 0.01 for $1.375 < |\eta| < 2.5$
- $\Delta\eta \times \Delta\phi = 0.1 \times 0.1$ for $2.5 < |\eta| < 3.2$

Thanks to its fine granularity it provides additional rejection power against $\pi^0$ decays. The middle layer has a constant cell size of $\Delta\eta\times\Delta\phi = 0.0025\times0.0025$. The second layer collects most of the energy of electrons and photons. The last layer is segmented in cells with a granularity of $\Delta\eta \times \Delta\phi = 0.05 \times 0.025$ completing the containment of the electromagnetic showers. For

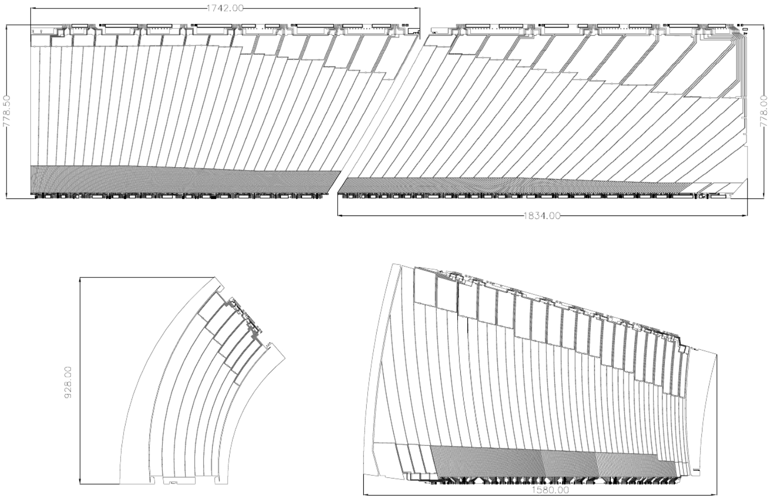


FIGURE 3.1: Different type of electrodes in the Electromagnetic Calorimeter, barrel (Up) and endcap (Down)

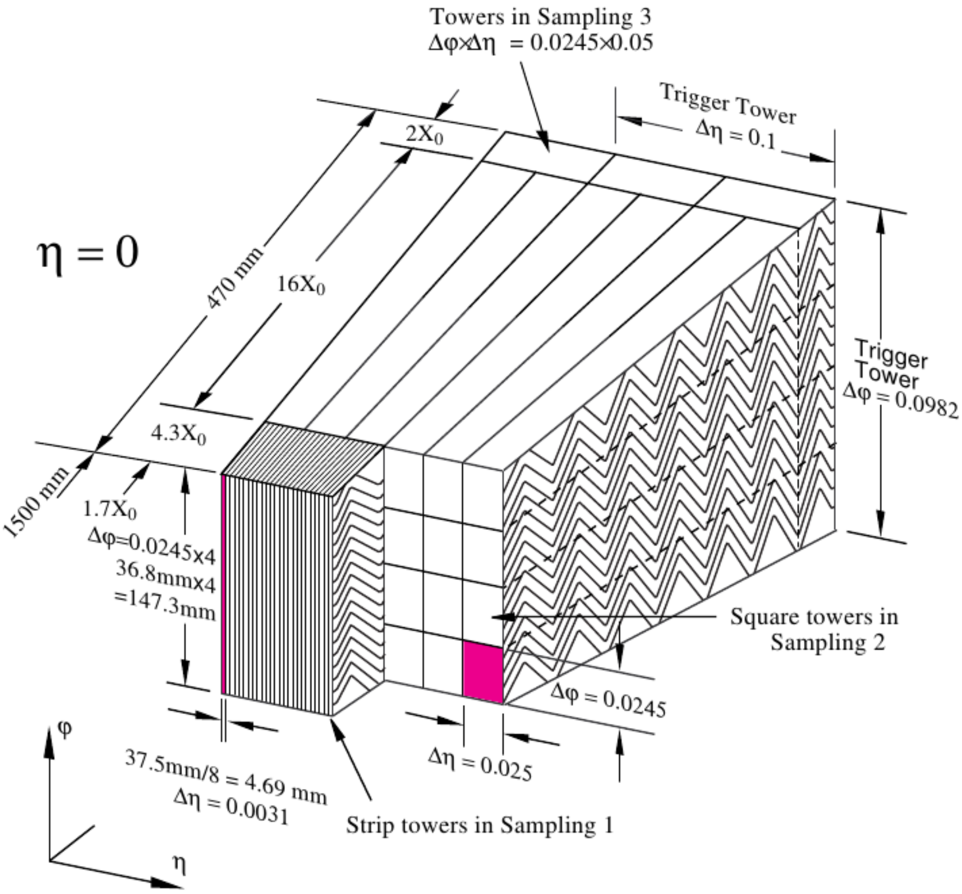


FIGURE 3.2: Barrel Module of the electromagnetic calorimeter

$|\eta| < 1.8$ another layer called presampler is present in front of the calorimeter; it is used to recover the energies lost in the ID material and Cryostat. The cumulative amounts of material before (Fig.3.4) and after the calorimeter (Fig 3.3) are shown as a function of the pseudorapidity.

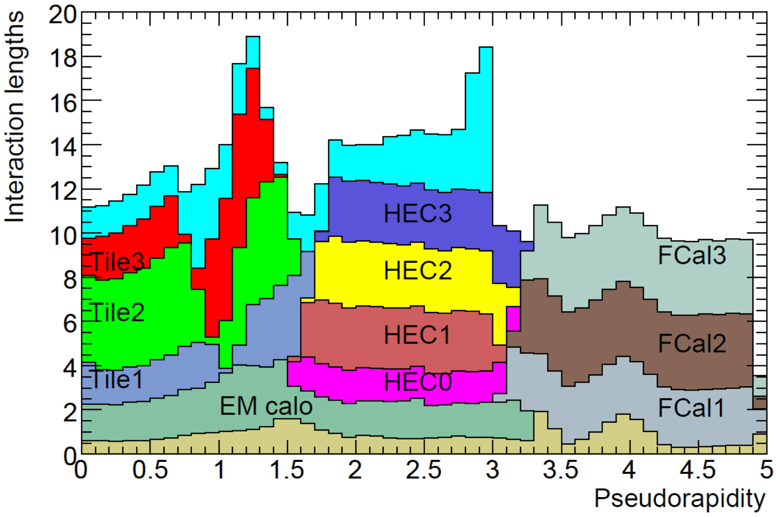


FIGURE 3.3: Cumulative amount of material, in $X_0$, as a function of $\eta$

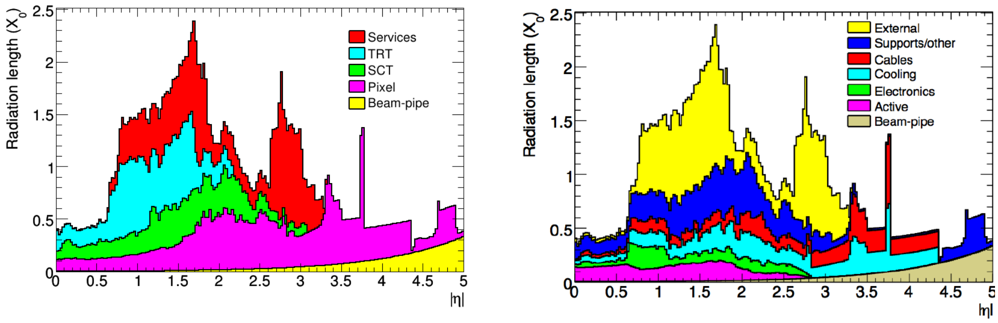


(a) (b)

FIGURE 3.4: Material budget in the inner detector in radiation length $X_0$ traversed by a particle existing the Inner Detector as a function of $\eta$ and integrated over $\phi$. The contributions of the different sub-detectors as well of the external services are shown in (a). Figure (b) shows the breakdown of this material budget into ID components [23]

An incident electron or photon interacts with lead and initiates an electromagnetic shower, whose secondary electrons ionize the active medium. An electrode in the middle of the liquid argon gap is powered on both sides with high voltage and the ionization electrons drift in gap. The total energy of the incident particle is proportional to the total ionization. The calibration of the electromagnetic calorimeter has a very important impact in the physics results related to electrons and photons. In particular a precise determination of the scale and the resolution are mandatory for the study of the properties of Higgs Boson decaying in two photons.

### 3.1.1 Barrel

The barrel calorimeter consists of two identical half-barrels, separated by a small gap of 4 mm at $z = 0$. Each half barrel is divided in 16 modules each covering $\Delta\phi = 22.5^o$.Each half barrel consist in 1024 accordion shaped lead absorbers interleaved with the readout electrodes. The readout electrodes consist of three conductive copper layers separated by insulating kapton sheets. The two outer layers are at high voltage whereas the inner layer is used for the readout of the signal via capacitive couplings. Azimuthal segmentation is obtained by ganging together the appropriate numbers of electrodes. For $|\eta| < 0.8$ ($|\eta| > 0.8$) the absorbers are made of lead and have a thickness of 1.53 mm (1.13 mm) respectively. The size of the drift gaps is 2.1 mm.

The barrel EM is divided into three sections in depth:

- **LAYER 1 (L1)** The very high segmentation in $\eta$ of the first layer permits a precise measurement of the shower position and a good rejection of fake photons from $\pi^0$ decay.
- **LAYER 2 (L2)** The second layer is the largest and allows to collect the larger fraction of the energy of the incoming particles and provide the most precise measurement in $\phi$.
- **LAYER 3 (L3)** The last layer is dedicated to the measurement of the tails of the showers.

All cells are read-out separately for a total number if 101760 channels

### 3.1.2 Endcap

The ECs are divided into two coaxial wheels: an outer wheel covering the region $1.375 < |\eta| < 2.5$ and a inner wheel covering $2.5 < |\eta| < 3.2$. The endcap wheels are divided into eight wedge shaped modules. In the outer (inner) wheel of each endcap, there are 768 (256) absorbers, interleaved with readout electrodes. The absorbers have a thickness of 1.7 mm for $|\eta| < 2.5$ and 2.2 mm for $|\eta| > 2.5$. The same segmentation in depth of the barrel calorimeter is present in the outer wheel, while only two layer for the inner wheel. The $\Delta\phi$ granularity is obtained by gathering the signal from adjacent electrodes.

### 3.1.3 Presampler

In the region $|\eta| < 1.8$, a presampler (PS) detector is placed in front of the calorimeter and is used to correct for the loss of energy upstream of the calorimeter. This detector consists of one single layer made of LAr, with a thickness of 1 cm in the barrel region and 0.5 cm in the endcap. Beyond $\eta = 1.8$ the PS is no longer necessary given the more limited dead material upstream the calorimeter. The PS is made of 32 identical azimuthal sectors, each of them 3.1 m long and 0.28 m wide. Each sector covers the region $\Delta\eta \times \Delta\phi = 1.52 \times 0.2$. The sectors are mounted on rails which are fixed on the barrel internal rings. Each sector contains eight modules, seven of them covering a region of $\Delta\eta \times \Delta\phi = 0.2 \times 0.2$ and the last, located at the edge of the sector, covering a region $\Delta\eta \times \Delta\phi = 0.12 \times 0.2$. Each module is divided into eight cells in $\eta$ and two cells in $\phi$, leading 16 cells per module, except at the ends of the barrel where the modules have a reduced size with only ten cells. In total 7808 readout channels are then needed for the PS. A module of the endcap PS is made of two active liquid-argon layers each 2 mm thick.

## 3.2 Electron and photon measurement in ATLAS

### 3.2.1 Reconstruction

The reconstruction of electrons and photons starts from energy deposits (clusters) in the EM calorimeter. The clusters are reconstructed using an algorithm called *sliding window*. The sliding windows algorithm starts defining a fixed size window ($0.125 \times 0.125$ correspond to $5 \times 5$ cells in the middle layer), that moves along the $\eta \times \phi$ rectangular plane [34]. If the sum of the energy of the cells in the $5 \times 5$ window is above a given threshold a pre-cluster is formed. The pre-cluster and the information of the ID are used to built the final electromagnetic cluster. The size of the cluster depends on the particles type.

- **An electron** is reconstructed if at least one well-reconstructed ID track is matched to the seed cluster.
- **A converted photons** are characterized by the presence of at least one track originating inside the tracker volume which matches an electromagnetic cluster.
- **An unconverted photons** are characterized by the absence of matched tracks.

The electron cluster is then rebuilt with size $3 \times 7$ and $5 \times 5$ longitudinal towers of cells in the barrel and endcap region respectively. For converted photons $3 \times 7$ cluster size is used in the barrel, while $3 \times 5$ cluster is associated to unconverted photons. The same cluster size $5 \times 5$ is used in the endcaps for converted and unconverted photons. The choice of the cluster size is a compromise between the attempt to contain the full cluster energy and the presence of pileup and electronic noise.

### 3.2.2 Identification

The cluster of electron and photon candidates should satisfy a set of identification criteria that require the longitudinal and transverse shower profiles to be consistent with those expected for electromagnetic showers. In particular for photons (Fig.3.5a) the main background is the $\pi^0 \to \gamma\gamma$ (Fig.3.5b) while for electrons are QCD jets, heavy flavor decays leading to non isolated electrons and electrons from photon conversion. The discrimination is obtained using information from the calorimeter, the ID and also using combination of these two.

Different sets of cut are defined for electron and photons.

- *Loose Selection:* It has a common set of cuts for $e$ and $\gamma$. This selection is based mainly on the information on the middle layer and the hadronic leakage.
- *Tight Selection:* The tight photon requirements are also optimised to provide good rejection of the most dangerous background consisting in jets with high $p_T$ leading $\pi_0$. They comprise tighter cuts on the variables used for the loose cut selection and additional cuts on the middle layer and especially on the strip layer with its fine granularity which provides good $\gamma$-$\pi_0$ separation.

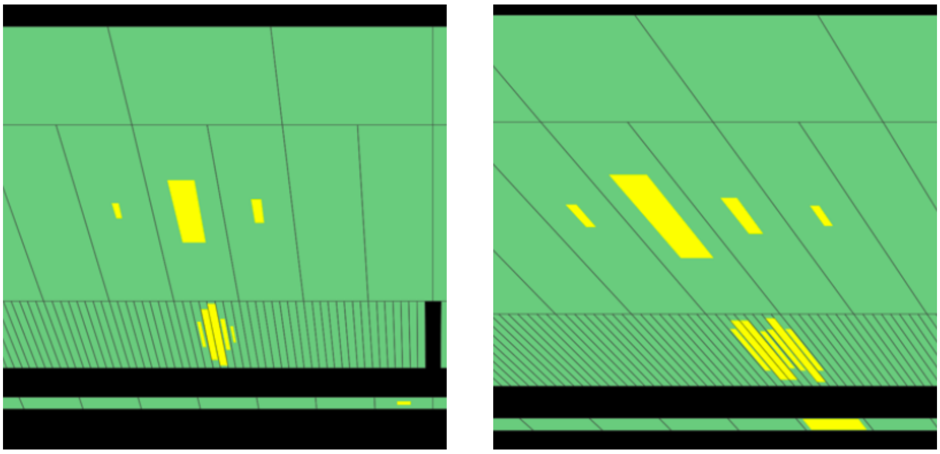

(A) Unconverted photon (B) $\pi^0 \to \gamma\gamma$

FIGURE 3.5: Shower shapes for a photon candidate (left) and a candidate for a jet with a leading $\pi^0$ (right), in data recorded in proton-proton collisions [35].

Table 3.1 summarized the different variables used for the different identification selections for photons.As an example, Figure 3.7 shows the distribution of the $R_\eta$ and $R_\phi$ for converted and unconverted photons. The cuts are optimized in bins of $E_T$ and $\eta$ for electrons and only in bins of $\eta$ for photons, but separately for unconverted and converted photons. The typical efficiency and rejection for the loose and the tight cut requirement are shown in Table 3.1 and Fig. 3.6.

| Type | Description | Name |
|---|---|---|
| | **Loose electron and photon cuts** | |
| Acceptance of the detector | $\lvert\eta\rvert < 2.47$ for electrons, $\lvert\eta\rvert < 2.37$ for photons ($1.37 < \lvert\eta\rvert < 1.52$ excluded) | - |
| Hadronic leakage | Ratio of $E_T$ in the 1st sampling of the hadronic calorimeter to $E_T$ of the EM cluster (used over the range $\lvert\eta\rvert < 0.8$ and $\lvert\eta\rvert > 1.37$) | $R_{had1}$ |
| | Ratio of $E_T$ in the hadronic calorimeter to $E_T$ of the EM cluster (used over the range $\lvert\eta\rvert > 0.8$ and $\lvert\eta\rvert < 1.37$) | $R_{had}$ |
| Middle layer of the EM calorimeter | Ratio in $\eta$ of cell energies in $3 \times 7$ versus $7 \times 7$ cells. | $R_\eta$ |
| | Lateral width of the shower | $w_2$ |
| | **Medium electron cuts (in addition to the loose cuts)** | |
| Strip layer of the EM calorimeter | Total lateral shower width (20 strips) | $w_{stot}$ |
| | Ratio of the energy difference between the largest and second largest energy deposits over the sum of these energies | $E_{ratio}$ |
| Track quality | Number of hits in the pixel detector (at least one) | - |
| | Number of hits in the pixels and SCT (at least seven) | - |
| | Transverse impact parameter (<5 mm) | $d_0$ |
| Track matching | $\Delta\eta$ between the cluster and the track in the strip layer of the EM calorimeter | $\Delta\eta_1$ |
| | **Tight electron cuts (in addition to the medium electron cuts)** | |
| B-layer | Number of hits in the B-layer (at least one) | |
| Track matching | $\Delta\phi$ between the cluster and the track in the middle layer of the EM calorimeter | $\Delta\phi_2$ |
| | Ratio of the cluster energy to the track momentum | E/p |
| TRT | Total number of hits in the TRT (used over the acceptance of the TRT, $\lvert\eta\rvert < 2.0$) | - |
| | Ratio of the number of high-threshold hits to the total number of TRT hits (used over the acceptance of the TRT, $\lvert\eta\rvert < 2.0$) | - |
| | **Tight photon cuts (in addition to the loose cuts, applied with stricter thresholds)** | |
| Middle layer of the EM calorimeter | Ratio in $\phi$ of cell energies in 3×3 and 3×7 cells | $R_\phi$ |
| Strip layer of the | Shower width for three strips around maximum strip | $w_{s3}$ |
| EM calorimeter | Total lateral shower width | $w_{stot}$ |
| | Fraction of energy outside core of three central strips but within seven strips | $F_{side}$ |
| | Difference between the energy of the strip with the second largest energy deposit and the energy of the strip with the smallest energy deposit between the two leading strips | $\Delta E$ |
| | Ratio of the energy difference associated with the largest and second largest energy deposits over the sum of these energies | $E_{ratio}$ |

TABLE 3.1: Definition of variables used for all electron and photon identification cuts.

| | | Efficiency (%) | Jet rejection |
|---|---|---|---|
| Loose | All | 95.45 ± 0.01 | 908 ± 4 |
| | Unconverted | 97.80 ± 0.01 | |
| | Converted | 91.73 ± 0.01 | |
| Tight | All | 82.88 ± 0.02 | 4770 ± 40 |
| | Unconverted | 85.04 ± 0.03 | |
| | Converted | 79.44 ± 0.04 | |

TABLE 3.2: Expected overall photon efficiencies and jet background rejections for the two sets of identification cuts and an $E_T$–threshold of 20 GeV. Taken from [36]

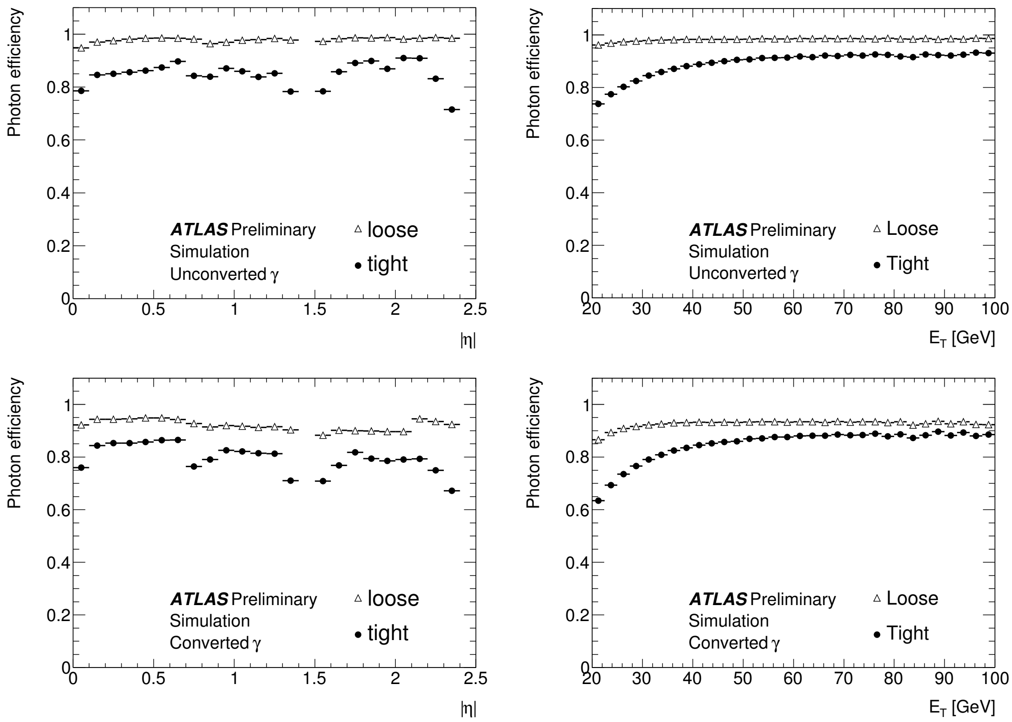


FIGURE 3.6: Expected photon efficiency vs $|\eta|$ (left) and $E_T$ (right) for loose and tight selection criteria and for unconverted (top) and converted (bottom) photons. Taken from [36]

## 3.3 Calibration Procedure

The calibration procedure that has been used for data and MC for the Run 1 data is described in this section (Fig 3.8). Data and MC follow different steps in order to ensure an optimal knowledge of the physic objects energy. The electromagnetic calorimeter is longitudinally segmented into separate compartments, the scales of the different samplings in data with respect to the simulation should be determined precisely in order to ensure the correct extrapolation of the response in the full $p_T$ range used in the various ATLAS analyses, from a few GeV up to the TeV scale. At this stage of the calibration the scale of the Presampler (E0) and the ratio between the layer 1 and 2 energies (E1/E2) are fixed (more details in Section 3.4).The next step consists of a set of uniformity corrections (Section 3.5) applied to data in specific regions, typically non optimal high voltage regions or cells with problems during signal amplification of the calorimeter. The data and MC energies are corrected using a MVA multivariate calibration (Section 3.6). The goal of the MVA calibration is to estimate the initial energy of the particles, identifying and if

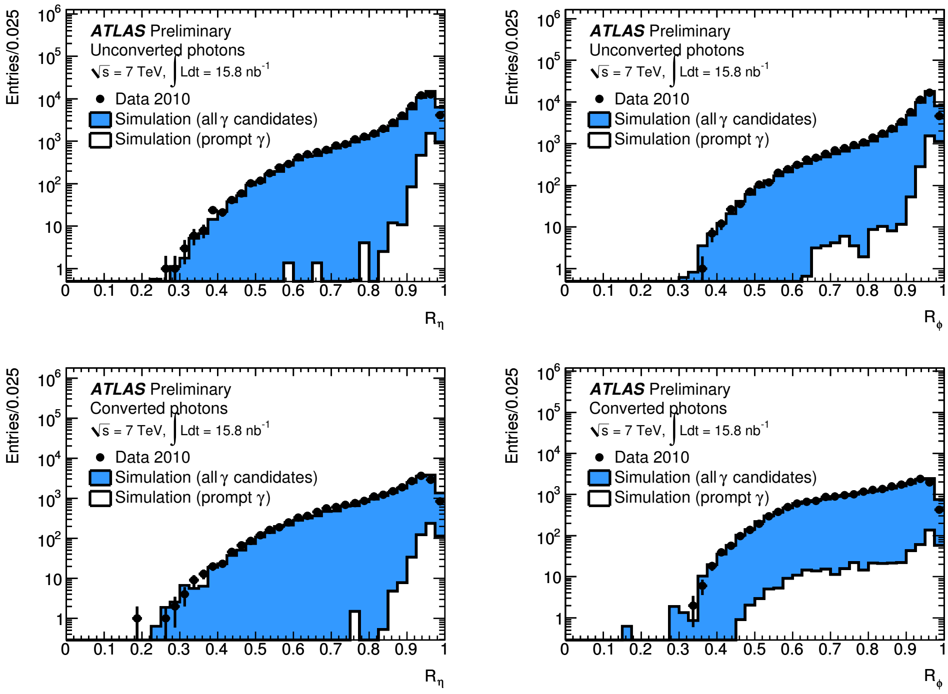


FIGURE 3.7: Examples of discriminating shower shape variables based on the energy deposit in the second longitudinal compartment of the electromagnetic calorimeter, for photon candidates with $|\eta| < 0.6$. Left: transverse shape variable $R_\eta$. Right: transverse shape variable $R_\phi$. Top: unconverted photon candidates. Bottom: converted photon candidates [37]

possible removing any dependence of the response with quantities like the impact position on the calorimeter and the shower profile. After all the mentioned corrections, electrons and photons response in data and simulation are matched using the large accumulated sample of $Z \rightarrow e^+e^-$ events (Section 3.7).A global scale extracted from the Z decay into electrons are applied to data while a smearing correction is applied on MC energies. In fact, the Z invariant mass resolution is typically larger in data than in the Monte Carlo because not all experimental effects are injected in the simulation. In the next sections I will go into the details of the calibration procedure. The impact on the photon energy of a certain systematics is evaluated in MC through the comparison between a nominal MC and a distorted MC in which the energy of the photons is increased by 1 sigma of the systematic uncertainty.

## 3.4 Calibration of the EM layer

The electromagnetic calorimeter is divided into three layers and a presampler ($|\eta| < 1.8$). A proper calibration of these four layer is necessary in order have the same response in data and MC for every layer.

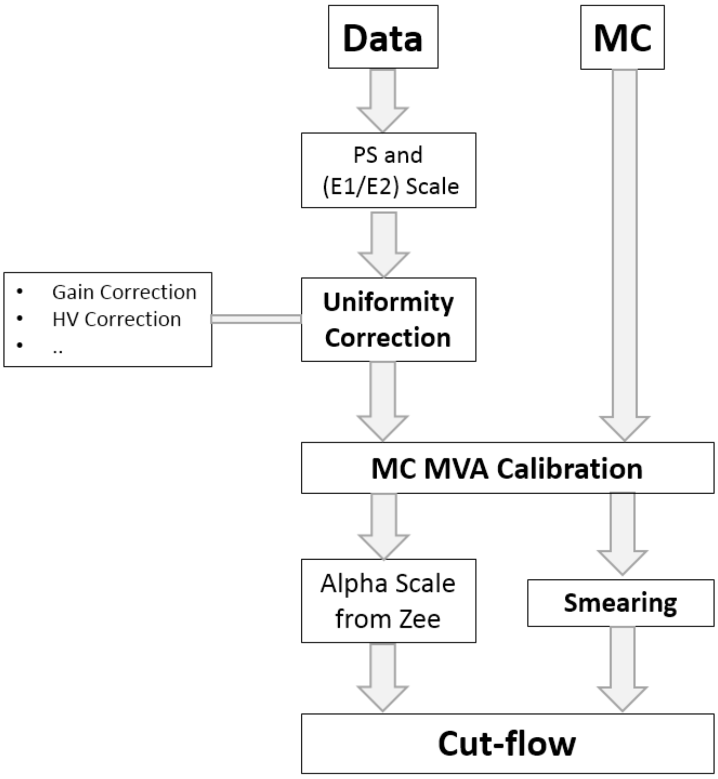


FIGURE 3.8: Procedure of calibration for Data and MC.

### 3.4.1 $E1/E2$ Modelling

The ratio between the energy deposits in the first ($E_1$) and the second ($E_2$) layer of the calorimeter provides a direct measurement of the the strip/middle layer inter-calibration.

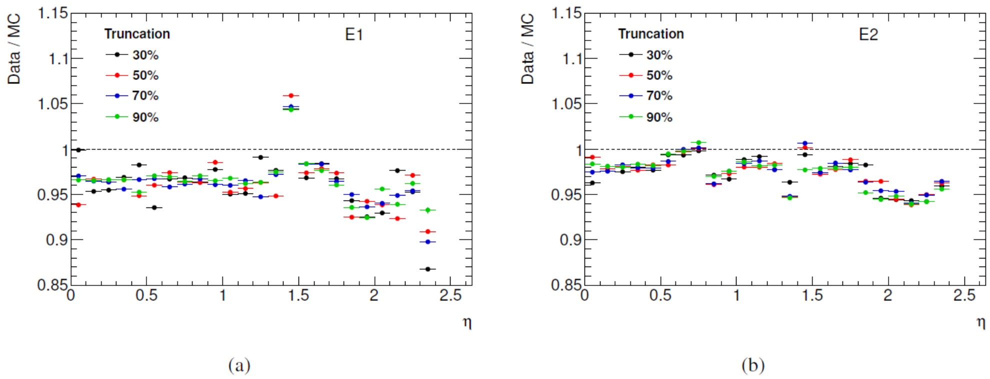


FIGURE 3.9: Ratio of the mean muon energy loss in data and MC for layer 1 (a) and layer 2 (b), estimated with the truncated mean method.

For this study muons are selected in Data and MC: muons deposit typically 50 MeV in the strips and about 250 MeV in the middle sampling of the electromagnetic calorimeter and deposit energy is very localized region: they can be considered as almost minimum ionizing particles (MIP). The usage of the muons is justified by the fact that their energy deposits are insensitive to the amount of material in front of the calorimeter and constitute a direct probe of the calorimeter response. However, due to very low fraction of energy loss in the layers, this method is sensitive to cross talk and electronic noise. The ratio between Data and MC for $E_1$ and $E_2$ are shown separately in Figure 3.9. As you can see the ratio data/MC is not uniform in function of $\eta$. To get flat the energies response, $E_2$ is corrected by the inter-calibration scale $\alpha_{1/2}$ defined as the double ratio between the energy deposit in the first and the second layer in Data and MC:

$$\alpha_{1/2} = \frac{\left\langle E_{1/2}^{data} \right\rangle}{\left\langle E_{1/2}^{MC} \right\rangle} \tag{3.1}$$

Different methods are used to extract the mean of the energy loss distribution: using a convoluted fit of a Landau and a Gaussian function or a truncated mean, defining the interval as the smallest one containing the 70% and the 90% of the distribution. The result of this study is illustrated in Figure 3.10. The systematics uncertainty on the energy scale (Fig. 3.11) is derived from the comparison of the different methods to extract the mean. The statistical components can be neglected. The typical accuracy of the measurement ranges from 1 to 3 %.

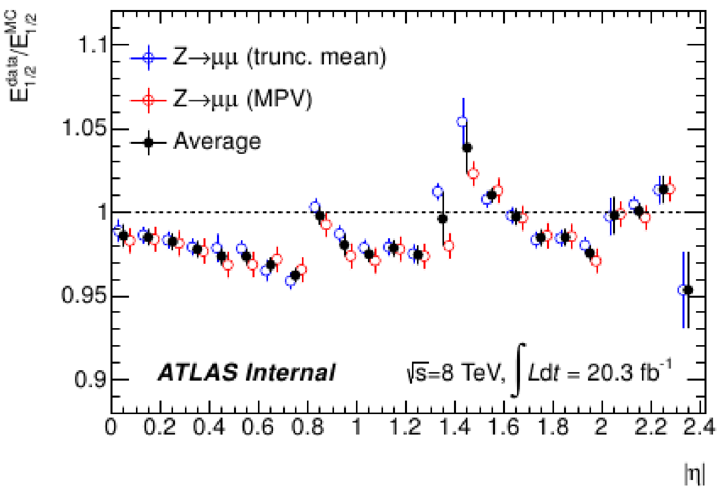


FIGURE 3.10: S1-S2 intercalibration. The errors bars represent sum of the statistical and the systematics errors [38]

### 3.4.2 PS energy scale

The PS energy scale $\alpha_{PS}$ is defined as the ratio between the PS energy in Data e MC and it is estimated from electrons from W and Z decay. The ratio can be interpreted as a energy scale only after subtracting the effect of passive material mis-modelling. In fact passive material in the simulation affects the electron shower development and the PS energy distribution. The presampler energy is correlated with the $E_1/E_2$ and it can be investigated using distorted MC in which materials were added in specific region in the definition of the geometry of the detector (Fig. 3.12). The impact on the distortion on $E_0$ and $E_{1/2}$ has been studied for each geometry [38].

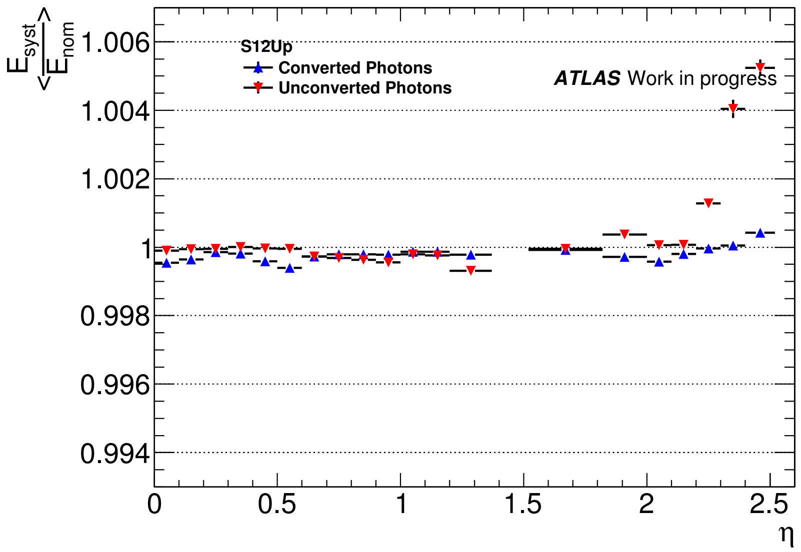


FIGURE 3.11: Photon Energy uncertainties coming from Intercalibration of L1 and L2

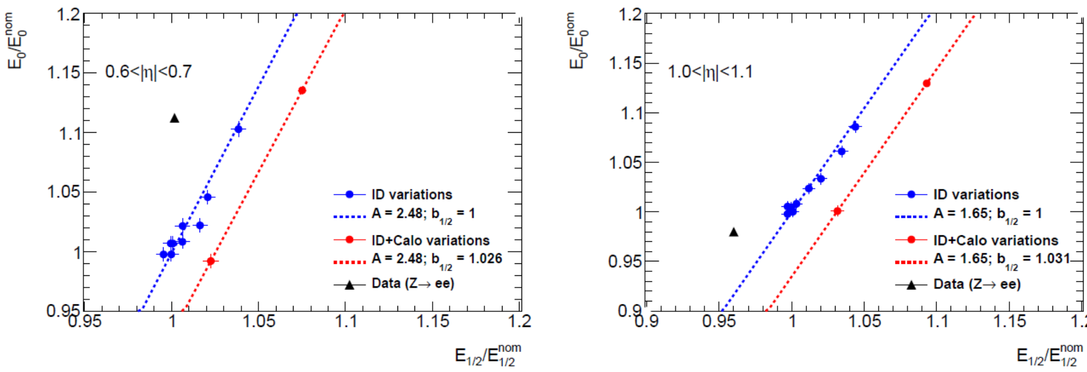


FIGURE 3.12: Correlation between $E_0$ and $E_{12}$ under material variations upstream of the calorimeter. The circles are obtained adding up to 15% X0 inside the ID volume. The squares correspond to 5% X0 added between the PS and L1, in addition to ID material variations. The simulation variations are normalized to the nominal geometry prediction.

The following parameterization in Eq. 3.2 summarizes the impact of passive material variations in front of the accordion on $E_0$ and $E_{1/2}$.

$$\frac{E_0\left(\eta\right)}{E_0^{nom}\left(\eta\right)} = 1 + A\left(\eta\right)\left(\frac{E_{1/2}}{E_{1/2}^{nom}\left(\eta\right) b_{1/2}\left(\eta\right)} - 1\right) \tag{3.2}$$

where $b_{1/2}$ parametrizes a possible bias of $E_{1/2}$ in the accordion. This bias can reflect imperfect relative calibration of the calorimeter samplings, and/or imperfect modeling of the passive material between the presampler and the accordion. $b_{1/2}$ is extracted in data using a sample of unconverted photons with a 300 MeV cut on the PS energy. In this way the sample is a little sensitive to material before the presampler. After the subtraction of material contribution one can determine the $E_0^{corr}$ in MC by injecting $E_{1/2}$ measured in Data:

$$\frac{E_0^{corr}(\eta)}{E_0^{nom}(\eta)} = 1 + A(\eta)\left(\frac{E_{1/2}^{data}}{E_{1/2}^{nom}(\eta)\, b_{1/2}(\eta)} - 1\right) \tag{3.3}$$

where $E_0^{corr}$ corresponds to the amount of expected PS energy scale in the simulation, after correction for the material induced bias. The intrinsic PS scale can be defined as:

$$\alpha_{PS}(\eta) = \frac{E_0^{data}(\eta)}{E_0^{corr}(\eta)} \tag{3.4}$$

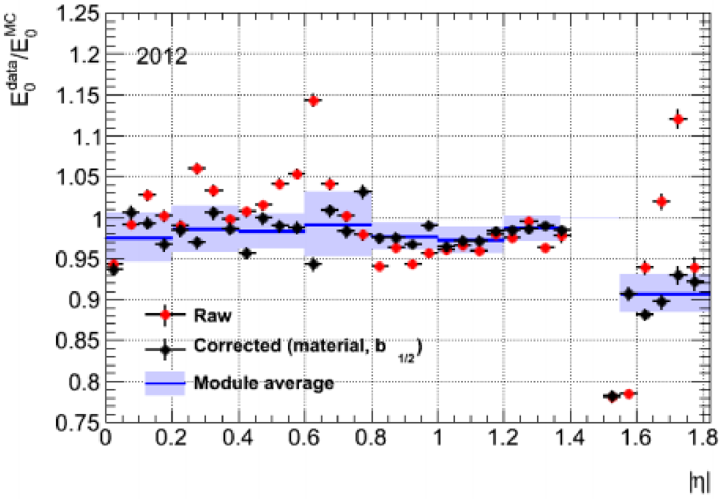


FIGURE 3.13: Ratio of average presampler energies in data and simulation, before and after the corrections for material and $b_{1/2}$. The filled rectangles represents $\alpha_{PS}(\eta)$ [38]

Uncertainties affecting the determination of $\alpha_{PS}(\eta)$ arise from the statistical and systematic uncertainties affecting $A(\eta)$ and $b_{1/2}$ and ranges between 2 to 3 %. The impact as a function of pseudorapidity is shown in Fig. 3.14.

## 3.5 Uniformity correction

A set of corrections are applied to data in order to improve the uniformity of response of the detector.
Four significant effects have been found for which it was necessary to introduce specific correction.

- **HV Issues:** In a few sectors of the EM accordion calorimeter the High Voltage was set to non-nominal value because of the presence of short circuits occurring at the level of the electrodes. In these cases a suitable correction is applied to compensate for this effect. Figure 3.15 shows the reconstruction of the Z pole in a particular eta region before and after the HV correction.

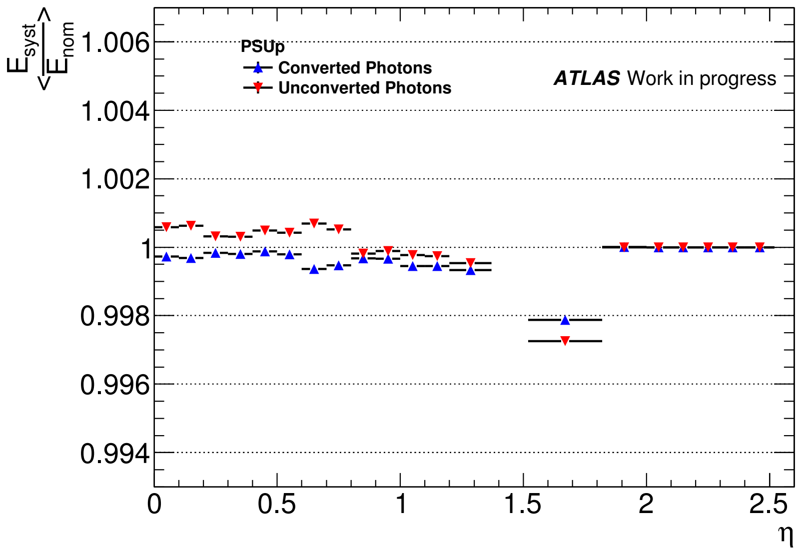


FIGURE 3.14: Photon Energy uncertainties coming from PS Scale

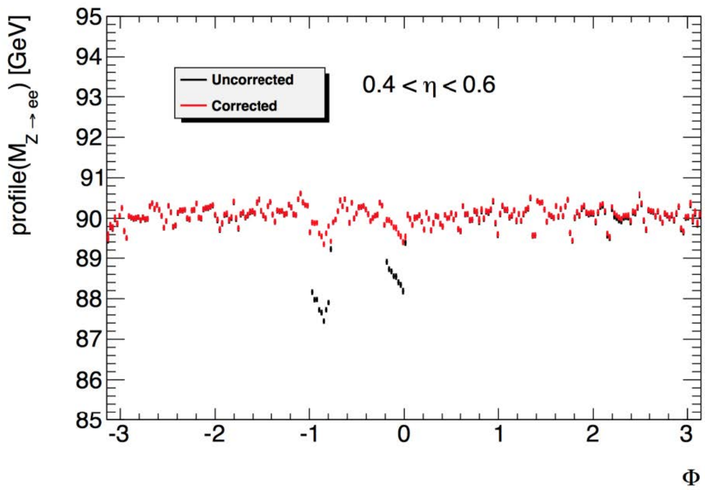


FIGURE 3.15: Profile of $M_{Z\to ee}$ for $1.2 < |\eta| < 1.37$ before and after HV correction.[39]

- **HV in PS:** In some PS sectors of the EM calorimeter the HV is set to non-nominal value due to noise issues. For all these cases, a time dependent correction is applied in order to mimic the response of nominal case.
- **Energy lost in gap:** A widening of the intermodule gaps has been observed in data which is not implemented in the description of the detector. This can cause different energy response between data and MC.
- **Gain Issues:** To be able to cover a wide energy range, signals from the detector are amplified in separate gains commonly called low, medium and high. Different responses in the reconstructed $Z \to ee$ mass difference between data and MC as a function of the energy of one electron have been observed after separating the cases where all cells of the

cluster are in high gain and the one where at least one cell is in medium gain. An example is shown in Fig. 3.16. An average correction has been defined to mitigate this effect.

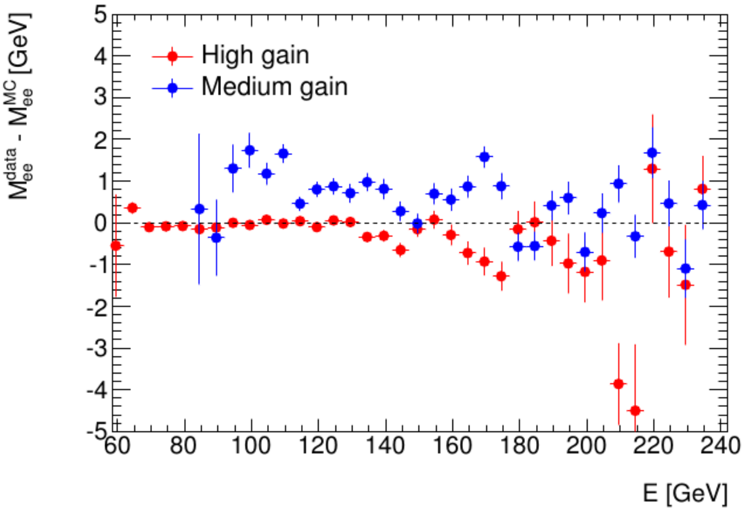


FIGURE 3.16: Reconstructed Z mass difference in Data e MC as a function of one electron energy. The cases where the cluster is made of all cells in high and the one with at least one cell in medium gain are shown separately [39]

No valid explanation for this effect has been found so the whole difference is considered as as uncertainty. The impact of the uncertainty on the energy scale due to the gain systematic variation as a function of $\eta$ is shown in figure 3.17.

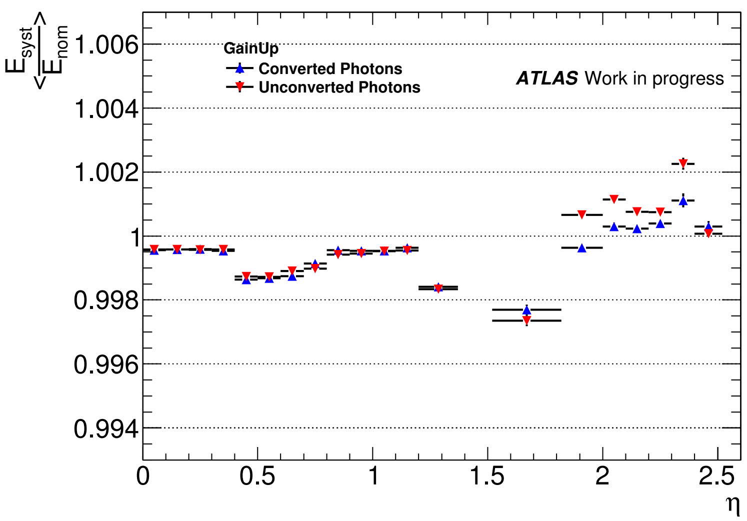


FIGURE 3.17: Photon Energy uncertainties coming from Gain Issues

## 3.6 MVA Calibration

After the end of Run 1 ATLAS data taking, the calibration chain has been revisited. A new calibration scheme has been developed using the Multivariate Analysis framework TMVA [40]. The aim of the calibration procedure is to estimate the real energy of the particles from the quantities measured by the calorimeter. The new calibration uses essentially the input used by the previous calibration [41] with some additional variables for converted photons. The input variable are:

- **Total energy in the accordion**: $E_{acc}$ defined as the sum of the uncalibrated energies of the accordion layers (strips, middle, back).
- $\frac{E_0}{E_{acc}}$: Ratio between the energy in the PS and the energy in the accordion.
- **Shower depth** $X = \frac{\sum X_i E_i}{\sum E_i}$ where $X_i$ is the depth of the center of each layer expressed in radiation length ($X_0$).
- **Pseudorapidity in the ATLAS frame** $\eta_{cluster}$ which is calculated with respect to the interaction point.
- **Cell index**: an integer number between 0 and 99 defined as the integer part of the division $\eta_{calo}/\Delta\eta$:
  - $\eta_{calo}$ is the pseudorapidity of the cluster in the calorimeter frame
  - $\Delta\eta = 0.025$
- $\eta$ **with respect to the cell edge** defined as the pseudorapidity (in the calorimeter frame) modulus the width of one cell of the middle layer $\Delta\eta = 0.025$.
- $\phi$ **with respect to the lead absorbers**

Additional variables are introduced only for converted photons:

- **Radius of the conversion** used only it $p_T > 3$ GeV, where $p_T$ is the sum of the transverse momentum of conversion tracks: otherwise R is not used.
- **Ratio between $E_T$ in the accordion and $p_T$ in the ID**: $E_T^{acc}/p_T$
  where $E_T^{acc} = E_T/\cosh(\eta_{cluster})$
- **Fraction of the conversion $p_T$ carried by the highest$-p_T$ track**.

The MVA calibration has been optimized for electron, unconverted photon and converted photon separately. The algorithm try to estimate the correction to be applied to the non-calibrated energy to match the true energy. The calibration constants have been extracted in bins of pseudorapidity and $p_T$. The binning was chosen to match approximately the non-uniformities of the detector. A grid of $10 \times 9$ bins in $|\eta_{cluster}| \times E_T^{acc}$ was defined, and an additional $2 \times 6$ smaller "special bins" for the regions close to the edges of the two half-barrel modules. The total numbers of bins is 102 for each type of particles. The bins edge are listed below:

- Bins in $|\eta_{cluster}|$: 0, 0.05, 0.65, 0.8, 1.0, 1.2, 1.37, 1.55, 1.74, 1.82, 2.0, 2.2, 2.47, where 1.37-1.52 is excluded and 0-0.05 and 1.52-1.55 are special bins.
- Bins in $E_T^{acc}$ ("normal"): 0, 10, 20, 40, 60, 80, 120, 500, 1000 and 50 000 GeV.
- Bins in $E_T^{acc}$ ("special"): 0, 25, 50, 100, 500, 1000 and 50 000 GeV.

### 3.6.1 Impact of the MVA Calibration

Fig. 3.18 shows the energy resolution and the linearity response for electron and photon (converted and unconverted) as a function of $\eta$ and different transverse energy ranges.

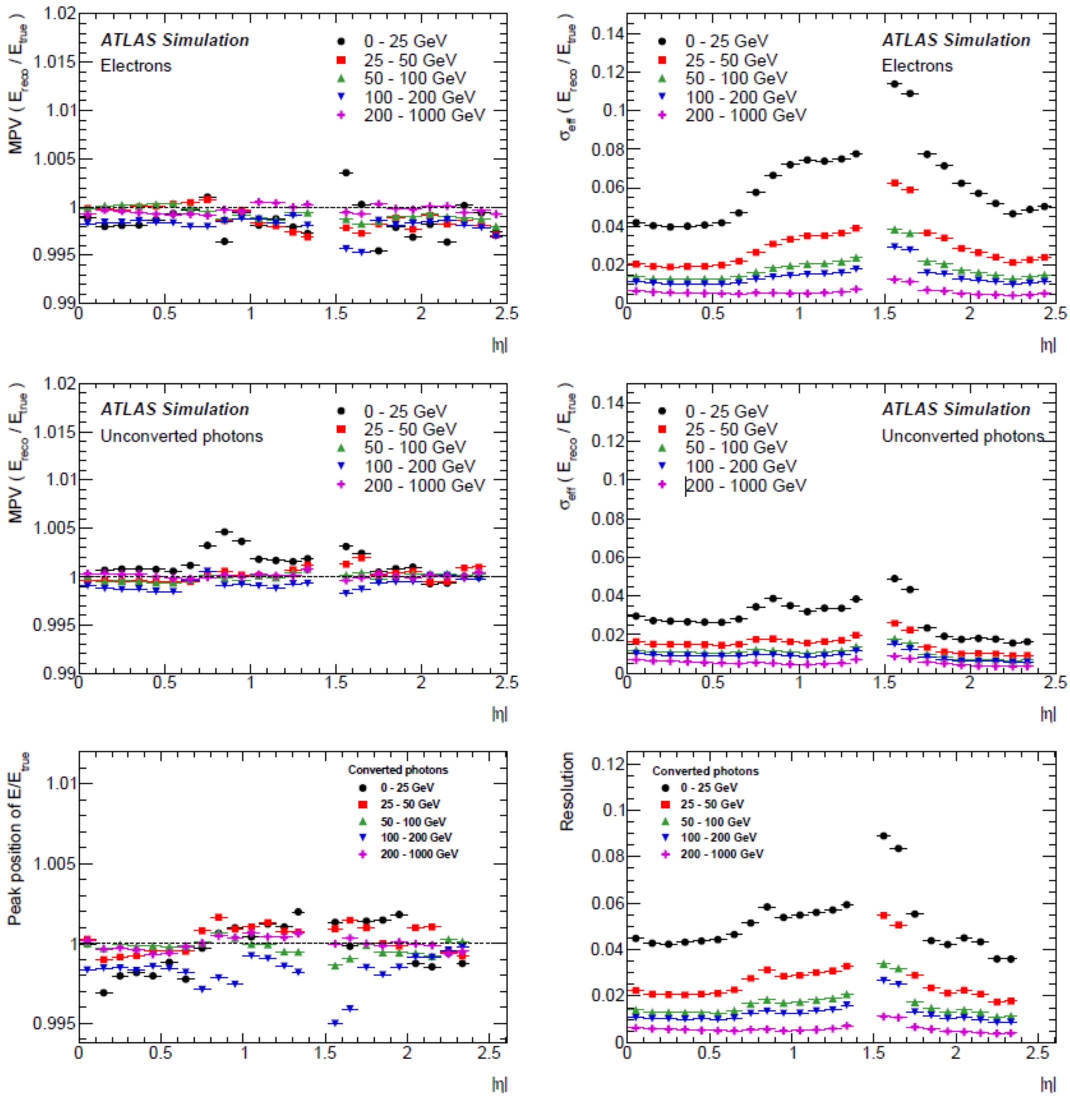


FIGURE 3.18: Energy response and resolution as function of $|\eta|$ and for different transverse energy ranges for electrons (top) unconverted photons (middle) and converted photons (bottom).

Figure 3.19 shows the di-photons invariant mass for a SM Higgs ($m_H = 125$ GeV) comparing the previous and the MVA calibration. The impact of the MVA calibration is important leading to a better reconstruction of the mass peak. The improvement on the resolution in the inclusive case is about 10%, with a maximum improvement in the transition region and for converted photon.

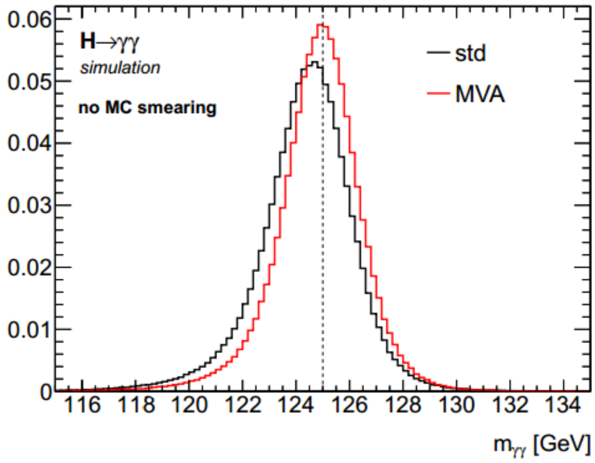


FIGURE 3.19: Di-photon invariant mass distribution for a SM Higgs with a mass of 125 GeV, comparing the standard calibration and the MVA calibration [42] .

## 3.7 Zee Scale

After the determination of the single layer scales (Section 3.4), a global data to MC calibration can be performed from the Z decay into electrons [43] in order to fix the global scale of the different calorimeter layers. The mass of a reconstructed $Z \to ee$ candidate is computed as:

$$M_Z = \sqrt{2E_a E_b(1 - \cos(\theta_{ab})} \tag{3.5}$$

where $E_a$ and $E_b$ are the energies of the two electrons measured by the calorimeter and $\theta_{ab}$ is the angle between the electrons measured by the tracker. Possible data to MC differences are parametrized in the following way for a given $\eta$ region:

$$E^{data} = E^{MC}(1 + \alpha_i) \tag{3.6}$$

where $E^{data}$ and $E^{MC}$ are the electron energy in data and simulation, and $\alpha_i$ represents the departure from optimal calibration, in a given pseudorapidity bin i. The impact on the Z mass peak can be parametrized:

$$\begin{aligned} M_{ij}^{data} &= M_{ij}^{MC}(1 + \alpha_{ij}) \\ &\sim M_{ij}^{MC}\left(1 + \frac{\alpha_i + \alpha_j}{2}\right) \end{aligned} \tag{3.7}$$

where $M^{data}$ and $M^{MC}$ are the measured di-electron mass in data and simulation, and $\alpha_{ij}$ the induced shift on the mass peak. The difference in resolution between MC and data must be taken into account. The expected resolution for the electromagnetic calorimeter can be written as:

$$\frac{\sigma(E)}{E} = \frac{a}{\sqrt{E}} \oplus \frac{b}{E} \oplus c \tag{3.8}$$

A smearing correction is derived for the MC under the assumption that the sampling term a is well modeled by the simulation. The noise term is taken from calibration runs so the additional correction must be proportional to the energy:

$$\sigma_{corr} = \sigma_{MC} \oplus c_{data} \times E \tag{3.9}$$

For each ($\eta_i$,$\eta_j$) category, the electron resolution correction and their impact on the mass peak satisfy

$$2c_{ij}^2 = c_i^2 + c_j^2 \tag{3.10}$$

Two different method are used for the extraction of the Zee scale and the smearing correction.

- **Lineshape fit method**
  This method consist in minimizing the following unbinned log-likelihood:

  $$-\ln(L_{tot}) = \sum_{k=1}^{N_{events}} -\ln L_{ij}\left(\frac{M_k}{1+\frac{\alpha_i+\alpha_j}{2}}\right) \tag{3.11}$$

  where $0 < i, j < N_{bin}$ , $N_{bin}$ is the number of region considered for the calibrated, $N_{events}$ is the total number of selected events and $L_{ij}(M)$ is the pdf quantifying the compatibility of an event with the expected Z boson line shape at the reconstruction level, when the electrons are in the i,j bin. The parameterization is based on the convolution of a Breit-Wigner and a Gaussian distribution.

- **Template fit method**
  This method considers two dimensional grid along ($\alpha_{ij}$,$c_{ij}$) for the different pseudorapidity configuration ($\eta_i$,$\eta_j$). A template histograms are created from this grid and for each ($\eta_i$,$\eta_j$) category the optimal value of $\alpha_{ij}$ and $c_{ij}$ are obtained by $\chi^2$ minimization. The individual electron scales and resolution are obtained by solving the linear systems given by Eq. 3.10 3.7.

The constant term and the smearing correction are shown in Figure 3.20. The uncertainties on energy scale from the extraction of the Zee scale are splitted in two contribution coming from the statistical and systematic part coming from pileup, electron selection and background contamination (Figure 3.21-3.22). After all corrections an overall are applied the Z lineshape description is fairly accurate as shown in Figure 3.23

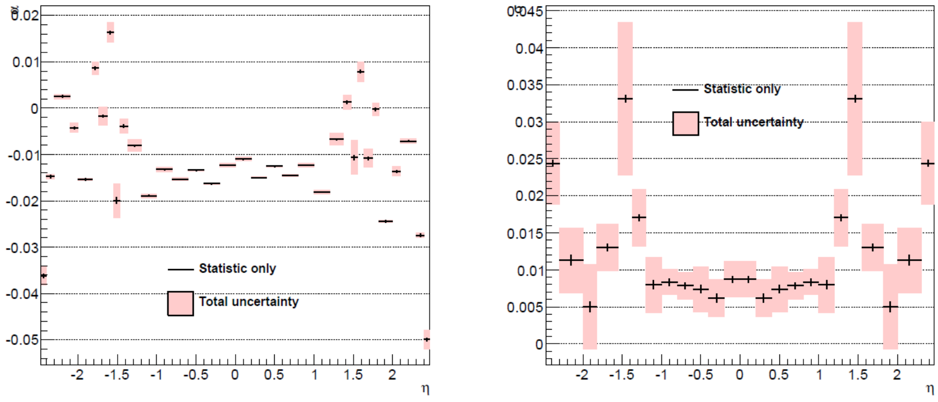


(a) (b)

FIGURE 3.20: Energy scales (a) and constant terms (b), as a function of $\eta$, displayed with only statistical uncertainties (black) and with the total uncertainties (red boxes).

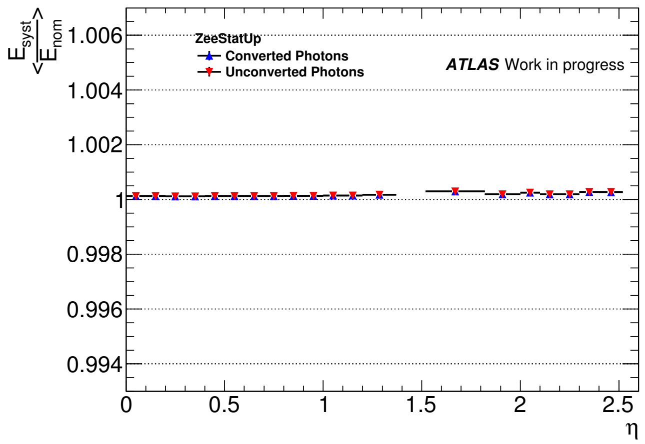


FIGURE 3.21: Photon Energy uncertainties coming from the extraction of the Zee Scale

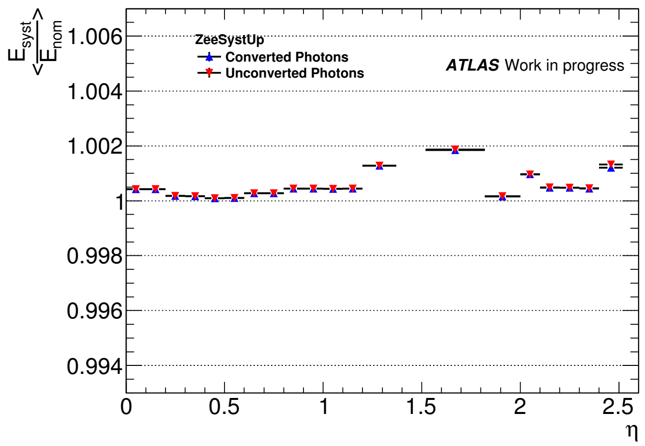


FIGURE 3.22: Photon Energy uncertainties coming from the extraction of the Zee Scale

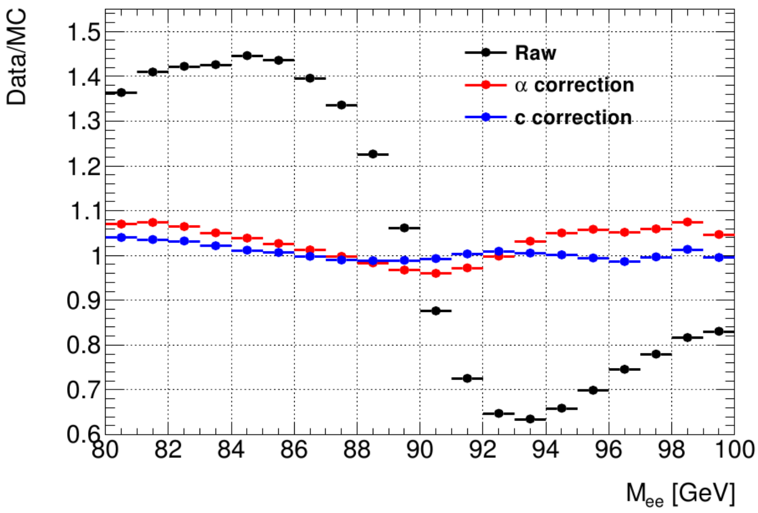


FIGURE 3.23: Ratio of the data to MC, as a function of the di-electron invariant mass. The ratio is shown ahead of correction (black) after the energy scale correction (blue) and after the smearing correction (blue)

## 3.8 Impact of passive material mismodeling

The study of the impact of material on the energy scale is described in this section. The description of the material inside the detector is well know for the object that built the structure of the detector. In the region between different part (e.g. between barrel and endcap region) the distribution of material is not well modeled due to dead material which may be services for the cryogenics or for the transport of electrical signals outside of the detector. The knowledge of the arrangement of the materials is very important with regard to the modeling of the interaction of electrons and the shower development of photons. Fig.3.24 shown the development of the shower shape in the EM calorimeter: the middle layer collects most of the shower, whereas the strips and the back collect respectively the begin and the end of this shower. The presampler measured the signal from particles which started showering in the ID material. Additional material in front of the calorimeter leads to a premature development of the shower that deposits then more energy in the strips and the presampler and less in the middle.

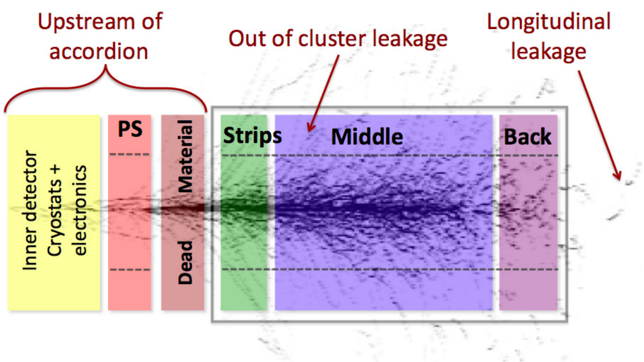


FIGURE 3.24: Illustration of the electromagnetic shower developing in the ATLAS electromagnetic calorimeter.

After all the correction for the layer calibration bias, the ratio $E_{1/2}$ for electromagnetic shower is a sensitive variable for the amount of detector material in front of the active calorimeter. Higher (lower) values of $E_{1/2}$ in data respect to MC indicates an earlier (later) shower development and hence a local excess (deficit) of material. Figure 3.25 shows the residual difference between data and MC on the modeling of $E_1$ over $E_2$. This plot indicates that the new simulation of the ATLAS geometry is well describing the material in front of the calorimeter.

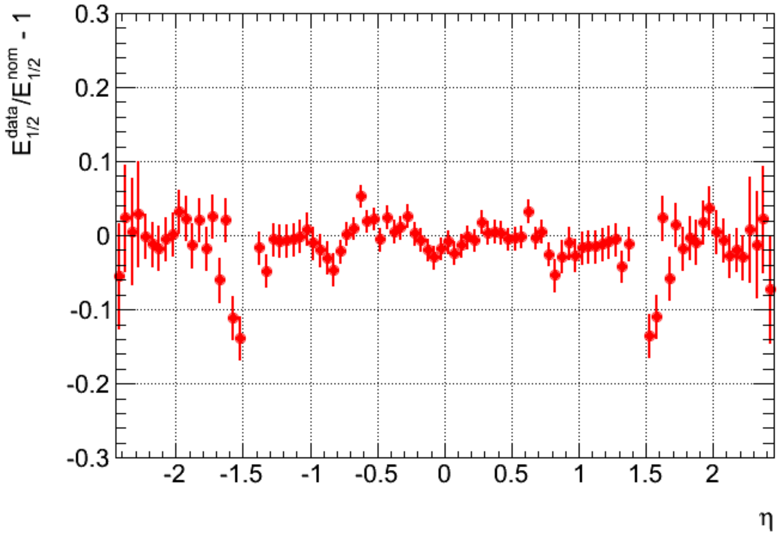


FIGURE 3.25: $E_{1/2}$ in data and simulation, after calibration corrections, using the new geometry.

The determination of material can be studied using the shower shape of different types of particles (Fig.3.26)

- **Muons** are sensitive to all the detector material.
- **Electron** are sensitive to all the material before the EM calorimeter.
- **Unconverted Photons** are less sensitive to inner detector material. If a additional veto on the PS activity is required, these photons are specifically sensitive to passive material after the PS and in front of S1.

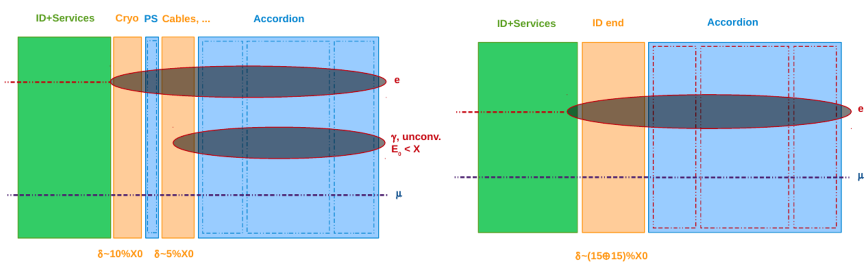


FIGURE 3.26: Sketch of EM shower development for the different particle categories described in the text, for $|\eta| < 1.8$ (left) and $|\eta| > 1.8$ (right).

The uncertainties related to the determination of passive material in the detector has an impact ($\delta\alpha$) on the energy scale of the photons.

$$\delta\alpha = \delta x_i \frac{\Delta\alpha_i}{\Delta X_i} \tag{3.12}$$

where $\delta x_i$ is the measured uncertainties on the determination of material in detector, $\Delta\alpha_i$ is the impact on the energy scale of a $\Delta X_i$ radiation length variation of detector geometry in a particular region.

### 3.8.1 Measurement of material distortion in data

The uncertainties on the determination of passive material is directly measured on data. The broad detector material categories that are addressed can be roughly summarized as follow, introducing very simplified nomenclature and ignoring the transition region.

- **ID Material**:
  covering the region close to the interaction point. This uncertainty is considered to be known *a priori*.
- **Cryostat Material**:
  covering material located between the maximal conversion radius and the PS, it's measured as difference between the energy energy release of electron and photons .
- **Calorimeter Material**:
  covering material within the volume of the calorimeter and located between PS and L1, it's measured with unconverted photons with a veto on the PS activity.

The impact of the passive material mismodelling on the energy response strongly depends on the radial position of the bias, due to varying distance of flight over which bremsstrahlung photons can drift away from the primary particle.

The measured uncertainties on the material can be divided in two contribution:

$$\delta x_i = \Delta X_{corr} + \Delta X_{datadriven} \tag{3.13}$$

where $\delta x_i$ is the total uncertainty in radiation length measured on data, $\Delta X_{corr}$ is the contribution in $X_0$ coming from the modelling of the Lar uncertainties (see next subsection). The residual $\Delta X_{datadriven}$ (ie the difference between the measured uncertainties and the correlated one) should be attributed to a variation of material in a particular regions. Figure 3.27-3.29 shown in red the total uncertainties of $X_0$ material, in dashed the correlated part.

### 3.8.2 LAr Uncertainties

The LAr Uncertainties affected the correlated part in Equation 3.13. The measurement of the strips/middle inter calibration is based on the response of the detector to the muons (see section

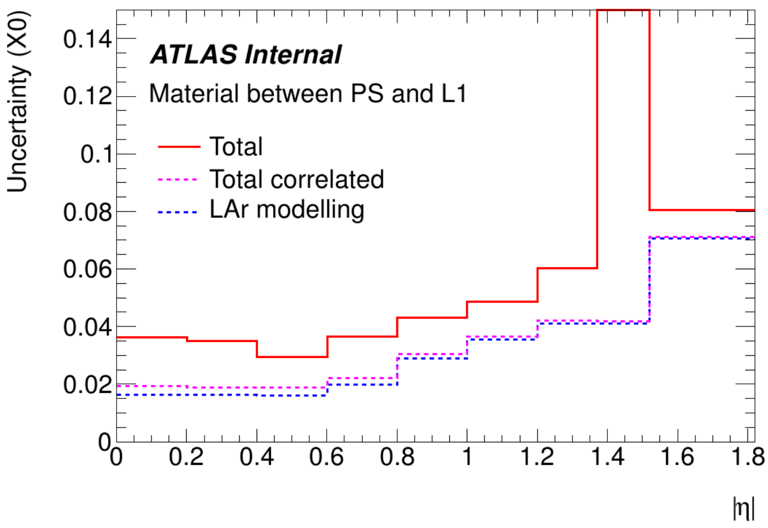


FIGURE 3.27: Uncertainty on the calorimeter material estimate, $\Delta X_{calo}$. The LAr $E_{1/2}$ modelling systematic uncertainty is assumed correlated across $\eta$.
The remaining part of the uncertainty is data driven and considered uncorrelated.

3.4). The response of the detector to electrons and photons is different since muons can be considered as minimum ionization particle while electron and photons not. Different source of uncertainties are considered:

- **The charge collection effect:**
  This relates to the true energy loss in LAr and the induced current. This factor is not constant because of the structure of the accordion folds and electrodes. The difference between the effect seen for muons and electrons or photons is taken as an effective uncertainty on the relative layer calibration and on the E1/E2 variable for EM shower.

- **The effective inactive area between L1 and L2:**
  This is a small longitudinal space between L1 and L2 in which the full electric fields is not applied. For the barrel, the effective inactive area of $\sim$ 1.1 mm was estimated while for the endcap a similar estimate was found to be $\sim$ 0.4 mm. The inactive area is interpreted as affecting the calibration of layer 2.

- **Location of the transition region between L1 and L2.**
  A change in the location of this transition effect directly the ratio E1/E2 without changing the total energy deposit. It is thus a direct source of uncertainty in the calibration derived from muons. The effect on muons is directly proportional to the change in the path length in the layer.

- **Cross talk:**
  This effect can be between the layer 1 and layer 2 or between neighbouring cells in L1 on one hand, and L2 on the other. Cross talk within L1 and L2 affect muons, electrons and photons differently, given the different number of cells used for the energy measurement.

- **Lateral EM shower shapes:**
  This uncertainties does not effect the intrinsic E1/E2 calibration with muons, but this have

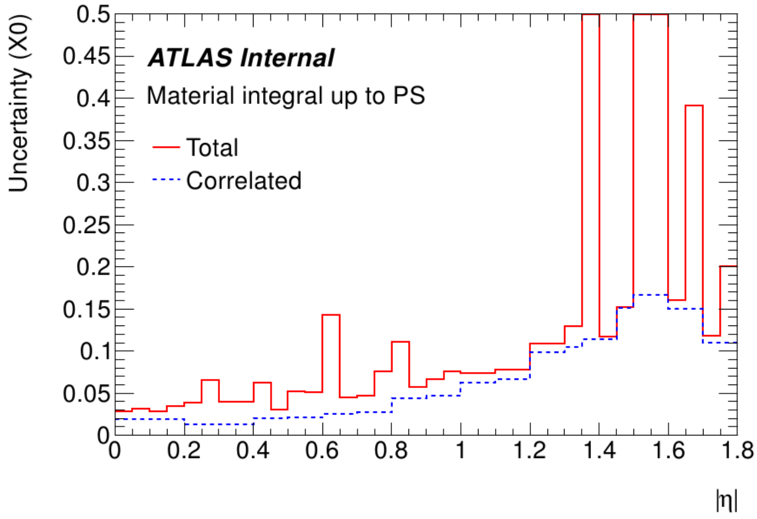


FIGURE 3.28: Uncertainty on the material integral up to the PS, $\Delta X_{PS}$. The LAr $E_{1/2}$ modelling systematic uncertainty is assumed correlated across $\eta$. The remaining part of the uncertainty is data driven and considered uncorrelated.

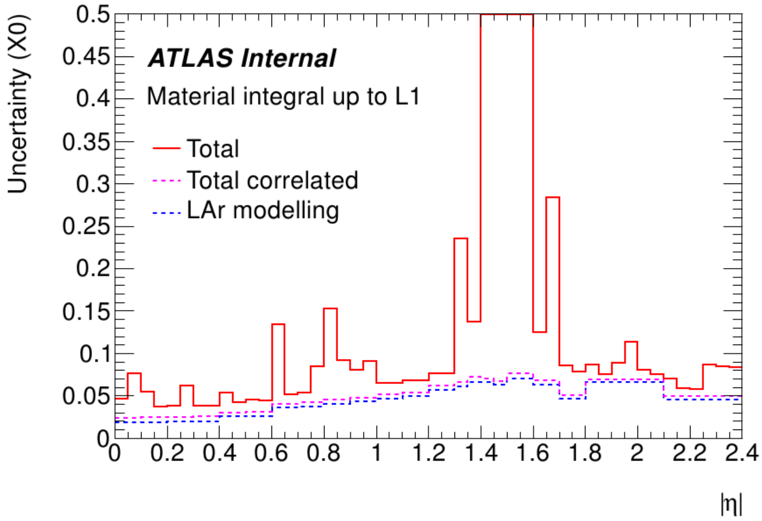


FIGURE 3.29: Uncertainty on the material integral up to L1, $\Delta X_{S1}$. The LAr $E_{1/2}$ modeling systematic uncertainty is assumed correlated across $\eta$.
The remaining part of the uncertainty is data driven and considered uncorrelated.

an effect for photons and electrons because this is measured using only cells in the cluster and the lateral leakage is mostly on layer 2.

### 3.8.3 Material

The data driven part of Equation 3.13 has to be attributed to a variation of detector geometry. The ID and Cryo material uncertainties are parametrized in function of the material measurement uncertainties up to the PS ($\Delta X_{PS}$) and S1 ($\Delta X_{S1}$).

Different distorted geometry have been defined and they are illustrated in Fig. 3.30-3.34.

**s1695** Distortion **A**

ID Material scaling by 5%. Figure 3.30

**s1683** Distortion **C'+D'**

SCT and Pixel service scaled by 10%. Figure 3.31

**s1684** Distortion **E'+L'**

$+5\%X_0$ at SRT/TRT endcap, $+5\%X_0$ between ID and PS. Figure 3.32

**s1685** Distortion **F'+M'+"X"**

$+7.5\%X_0$ at ID endplate, $+5\%X_0$ between PS and strips, Lar material increase in transition region.Figure 3.33

**s1643** Distortion 1643 **G'**

All variation together. Figure 3.34

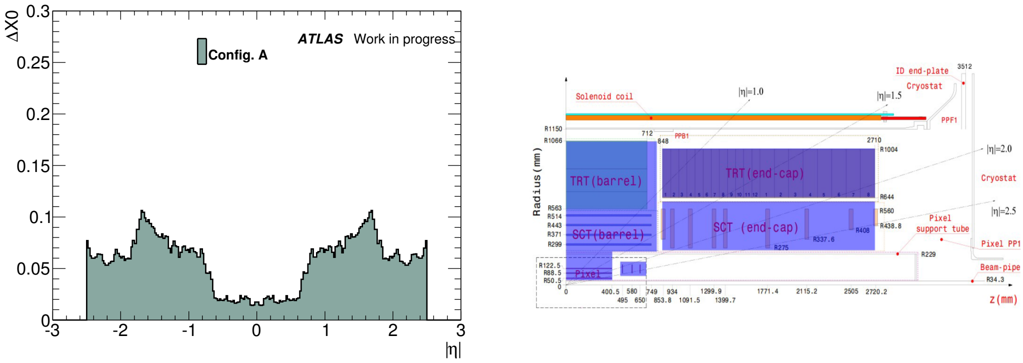


FIGURE 3.30: Distortion s1695, A

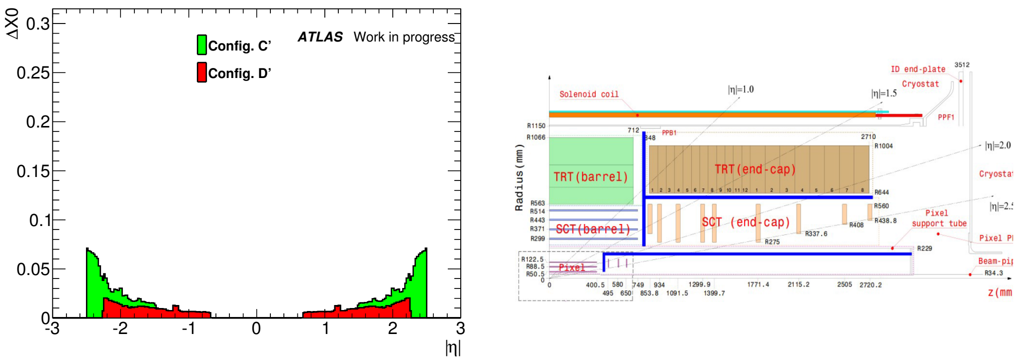


FIGURE 3.31: Distorsion s1683, C+D

The impact on energy scale due to additional material can be study by considering the ratio:

$$1 + \alpha_\gamma = \frac{\left\langle \frac{E_{reco}}{E_{true}} \right\rangle_{Dist}}{\left\langle \frac{E_{reco}}{E_{true}} \right\rangle_{Nom}} \tag{3.14}$$

where

- $E_{reco}$ is the reconstructed energy

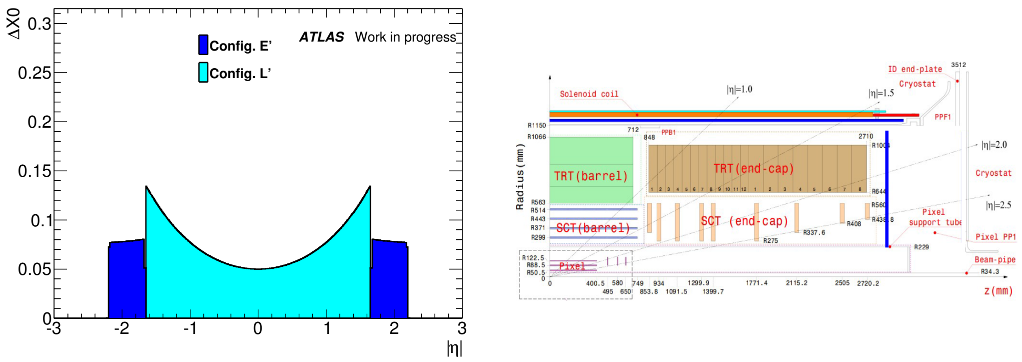


FIGURE 3.32: Distorsion s1684, E+L

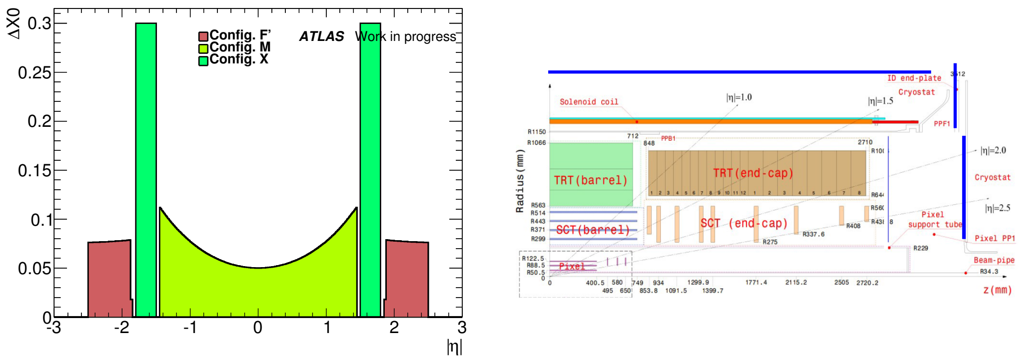


FIGURE 3.33: Distorsion s1685, F+M+"X"

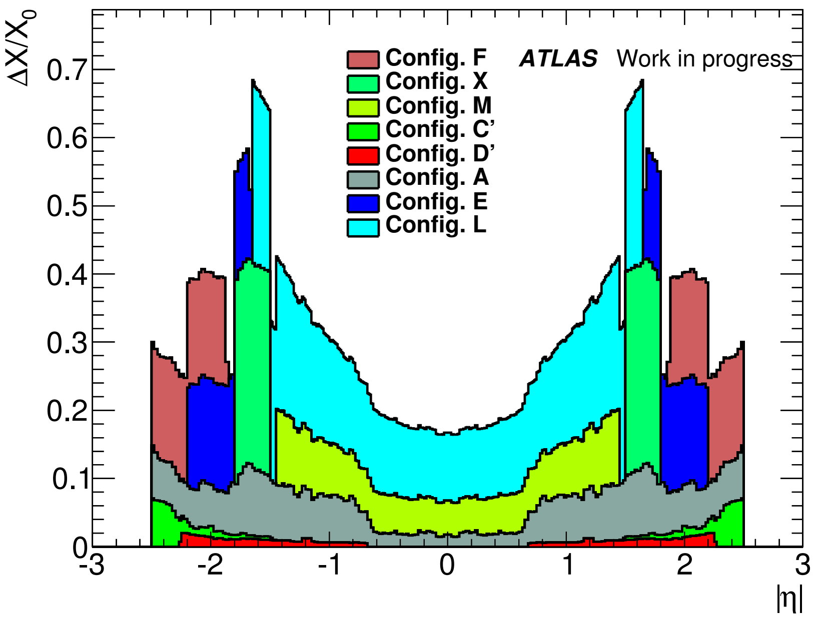


FIGURE 3.34: Distorion 1643

- $E_{true}$ is the true energy

in Nominal (Nom) and Distorted (Dist) MC. The distorted MC chosen for the study is very pessimistic configuration where large amount of material is added in specific region of the detector and not correspond to the effective measured uncertainties on the material determination. For each of the distortion the scale factor $\alpha_e$ are obtained(using the method described in Section 3.7) by comparing mass distribution of the $Z \to ee$ peak in nominal MC and distorted MC.

$$E_{dist} = (1 + \alpha_e)E_{nom} \tag{3.15}$$

In Figure 3.35 the $Zee$ scales are shown for the different distortion. For electron with energy

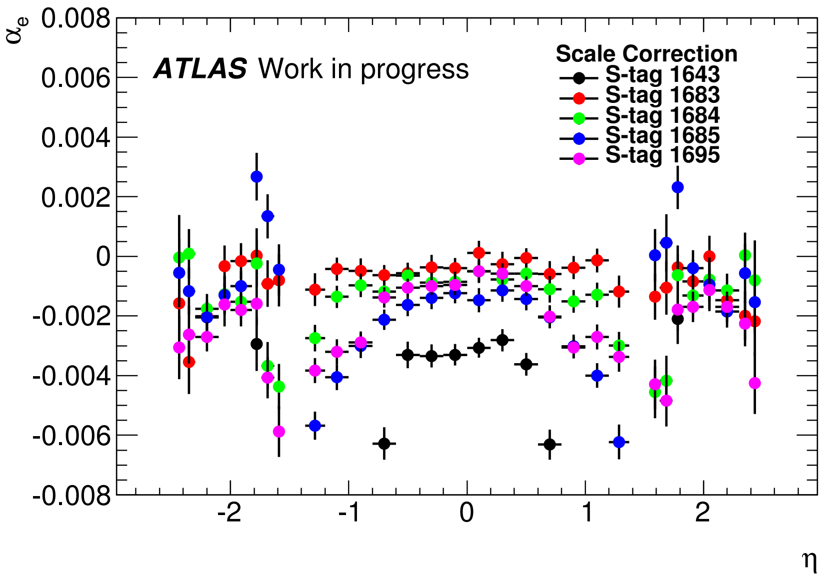


FIGURE 3.35: Scale MC to MC $Z \to ee$

around 40 GeV in a distorted MC, these scale factor should recover the energy that would have these electron if there was no additional material. Since converted photons resemble more to electron, the application of these scale would correct the energy of converted photons while over correct the energy of unconverted photons. This difference can be estimate evaluating:

$$1 + \delta_{mat} = \frac{\left\langle \frac{E'_{reco}}{E_{true}} \right\rangle_{Dist}}{\left\langle \frac{E_{reco}}{E_{true}} \right\rangle_{Nom}} \tag{3.16}$$

where

$$E'_{reco} = \frac{E_{reco}}{1 + \alpha_e} \tag{3.17}$$

Fig 3.36-3.40 shows the distributions of $1 + \delta_{mat}$ (left plot) and $1 + \alpha_\gamma$ (right plot) in function of $\eta$ for the different distortion. In the right plot the shift from 1 is more evident for converted photons: this is due to the fact that converted photons are more affected by the change of the material. This difference is recovered after applying the scales $\alpha_e$. As expected in the left plot the energy measurement for unconverted photons is overestimated. The $\delta_{mat}$ distribution are also shown in function on the conversion status (Fig. 3.41)

In order to estimate the effective effect of additional material the $\delta_{mat}$ can be divided by the amount of material $X_0$ in a given region of $\eta$. Figure 3.42 shown the "per mille" variation of

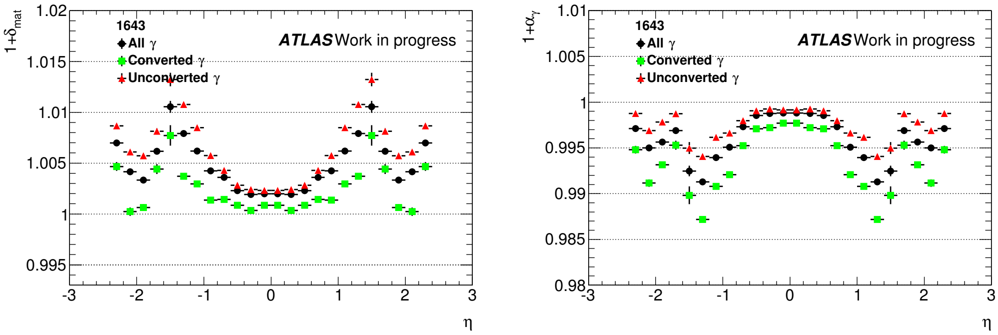


(A) $1 + \delta_{mat}$ (B) $1 + \alpha_\gamma$

FIGURE 3.36: Distorion 1643

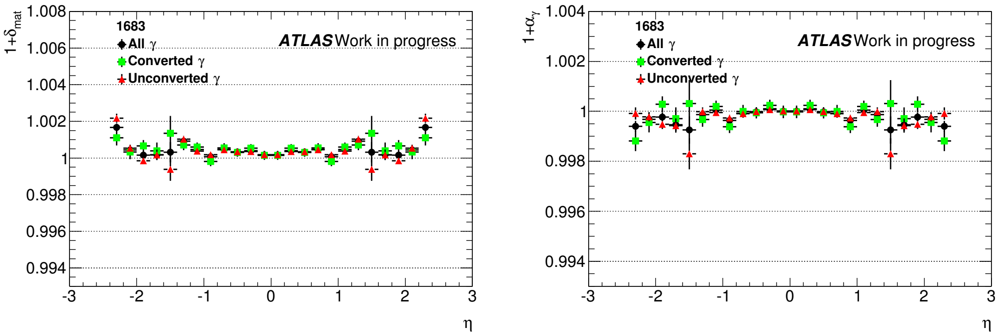


(A) $1 + \delta_{mat}$ (B) $1 + \alpha_\gamma$

FIGURE 3.37: Distorion 1683

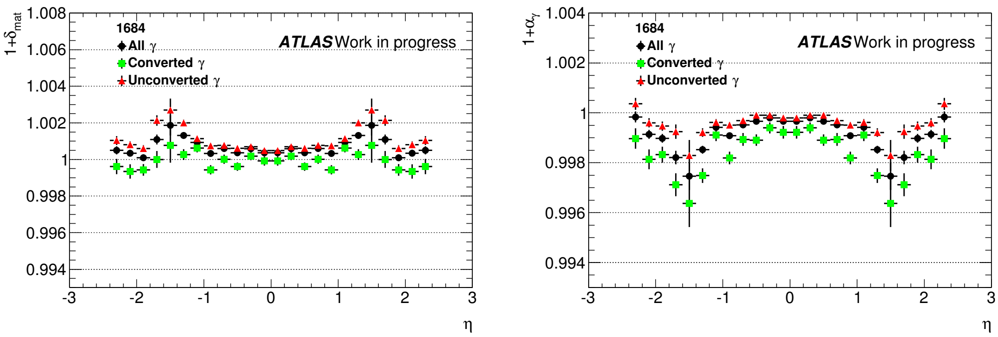


(A) $1 + \delta_{mat}$ (B) $1 + \alpha_\gamma$

FIGURE 3.38: Distorion 1684

energy scale over the per cent variation of $X_0$. We call this variation $\Delta\alpha/\Delta X_0$. The main contribution is given by adding material in the inner detector region.

The residual impact of material $\Delta X_{datadriven}$ (Eq 3.13) can now be attached to a variation of the $\alpha$ scale in a specific region of the detector.

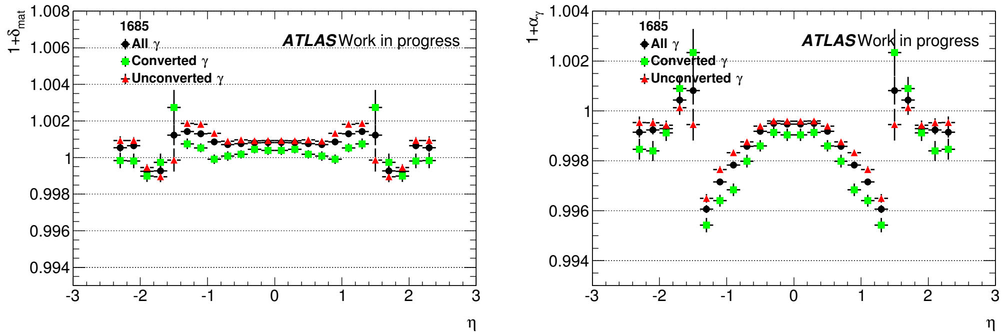


(A) $1 + \delta_{mat}$ (B) $1 + \alpha_\gamma$

Figure 3.39: Distorion 1685

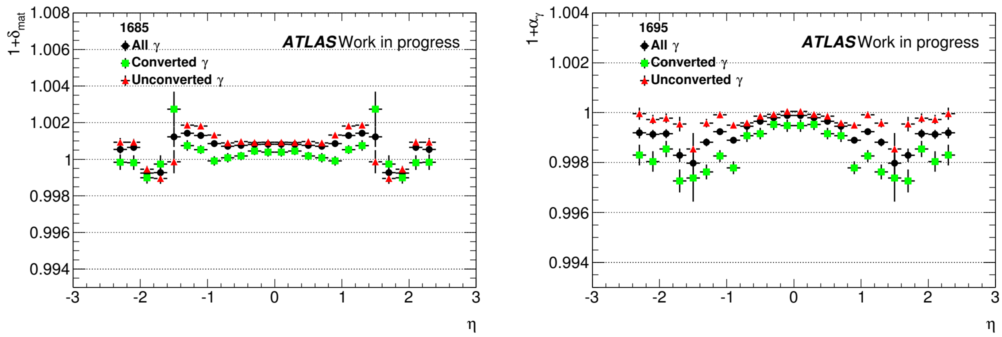


(A) $1 + \delta_{mat}$ (B) $1 + \alpha_\gamma$

Figure 3.40: Distorion 1695

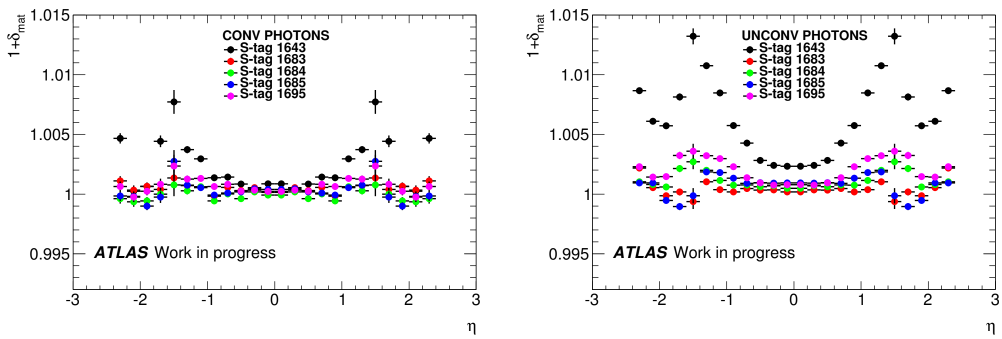


(A) Converted photon (B) Unconverted photon

Figure 3.41: $\delta_{mat}$ for every distorsion divided for photon conversion status

### 3.8.4 Overall uncertainty on the scale from material knowledge

The total impact of ID and Cryostat material biases upstream of the PS ($|\eta| < 1.8$) on energy scale can be expressed as:

$$\begin{aligned} \delta\alpha_{tot}^2 &= \delta\alpha_{ID}^2 + \delta\alpha_{Cyo}^2 + 2cov(\delta\alpha_{ID}, \delta\alpha_{Cryo}) \\ &= \delta X_{ID}\left(\frac{\Delta\alpha_A}{\Delta X_A}\right)^2 + \delta X_{Cryo}\left(\frac{\Delta\alpha_{E,L}}{\Delta X_{E,L}}\right)^2 + 2\frac{\Delta\alpha_A}{\Delta X_A}\frac{\Delta\alpha_{E,L}}{\Delta X_{E,L}}cov(\delta\alpha_{ID}, \delta\alpha_{Cryo}) \end{aligned} \tag{3.18}$$

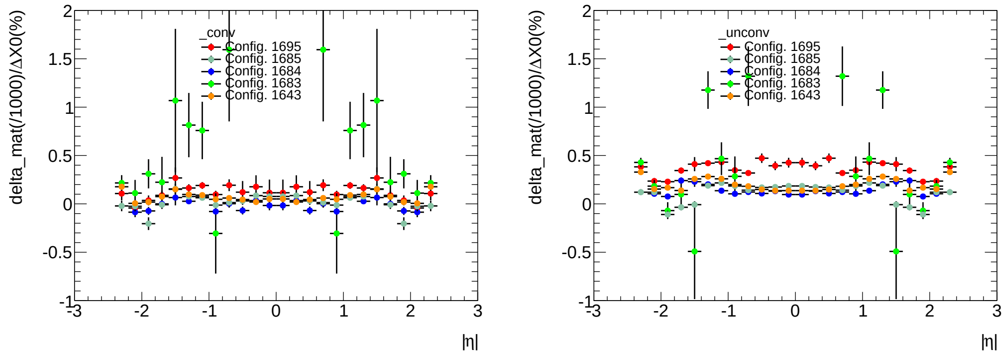


(A) Converted photon (B) Unconverted photon

FIGURE 3.42: $\delta_{mat}$ divide by the amount of material in given $\eta$ bin [(/1000)/(%)]

The last line can be simplified by considering the measured uncertainties of the ID all attributed to the configuration A

$$\delta X_{ID} \equiv \Delta X_A \tag{3.19}$$

and the Cryo uncertainties associated coming from:

$$\Delta X_{Cryo} = \Delta X_{PS,S1} \pm (\delta X_{PS,S1} \oplus \delta X_{ID}) \tag{3.20}$$

where $\delta X_{PS}$ is used for $|\eta| < 1.8$ and $\delta X_{S1}$ for $|\eta| > 1.8$.

$$cov(\delta\alpha_{ID}, \delta\alpha_{Cryo}) = -\delta X_{ID}^2 \tag{3.21}$$

The total energy scale variation can be written:

$$\delta\alpha_{tot}^2 = \left(\Delta\alpha_A - \Delta X_A \cdot \frac{\Delta\alpha_{E,L}}{\Delta X_{E,L}}\right)^2 + \delta X_{PS}^2 \left(\frac{\Delta\alpha_{E,L}}{\Delta X_{E,L}}\right)^2 \tag{3.22}$$

From Equation 3.22 we can decompose into different contributions.

$$\delta\alpha_{ID} = \Delta\alpha_A - \Delta X_A \cdot \frac{\Delta\alpha_{E,L}}{\Delta X_{E,L}} \tag{3.23}$$

$$\delta\alpha_{Cryo} = \delta X_{PS} \frac{\Delta\alpha_{E,L}}{\Delta X_{E,L}} \tag{3.24}$$

The first term, $\delta\alpha_{ID}$, is purely based on simulation, reflecting the a *priori* ID Material uncertainty an its impact on the energy scale. The second term $\delta\alpha_{Cryo}$, the material bias, $\delta X_{PS}$, is data driven and the energy scale sensitivity to this bias is determined from simulation. Similarly the integrated material estimate up to S1 is used for $|\eta| > 1.8$, beyond the PS acceptance.

$$\delta\alpha_{tot}^2 = \left(\Delta\alpha_A - \Delta X_A \cdot \frac{\Delta\alpha_{E,F}}{\Delta X_{E,F}}\right)^2 + \delta X_{S1}^2 \left(\frac{\Delta\alpha_{E,F}}{\Delta X_{E,F}}\right)^2 \tag{3.25}$$

$$\delta\alpha_{ID} = \Delta\alpha_A - \Delta X_A \cdot \frac{\Delta\alpha_{E,F}}{\Delta X_{E,F}} \tag{3.26}$$

$$\delta\alpha_{Cryo} = \delta X_{S1} \frac{\Delta\alpha_{E,F}}{\Delta X_{E,F}} \tag{3.27}$$

Finally, the energy scale bias induced by the passive material between the PS and the S1 ($\eta < 1.8$) is:

$$\delta\alpha_{Calo} = \delta X_{Calo} \frac{\Delta\alpha_{M,N}}{\Delta X_{M,N}} \tag{3.28}$$

### 3.8.5 Impact on energy scale of LAr and Material uncertainties

The impact of the LAr uncertainties has been evaluated with single particle simulations: muons and electrons of $E_T$ of 40 GeV (average $E_T$ of electrons coming from Z decay) and photons of 20 GeV (average $E_T$ of radiative photons) are simulated. The resulting $E_{1/2}$ distributions allow to evaluate the overall uncertainty. These effect is taken into account defining 4 source of uncertainties for the Lar calorimeter (Fig. 3.43-3.46). The impact of material uncertainties on the energy scale are shown in Figure 3.47-3.49.

- **Lar Calibration**
  This terms comes from the various uncertainties to the E1/E2 calibration derived from muons.

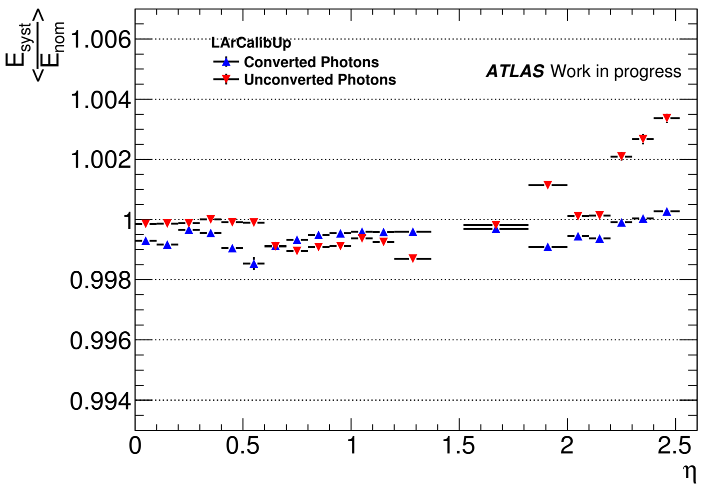


FIGURE 3.43: Photon Energy uncertainties coming from Lar Calibration

- **Lar Calibration for electron**
  This terms comes from the various uncertainties to the E1/E2 calibration for electrons in the endcap region.

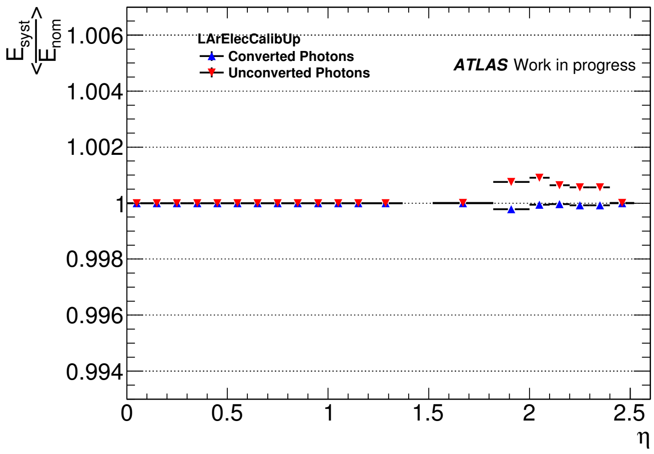


FIGURE 3.44: Photon Energy uncertainties coming from Lar Calibration for electron

- **E1/E2 modelling for electron and unconverted photons**
  This terms comes from the various uncertainties to the E1/E2 calibration for unconverted photons and electrons.

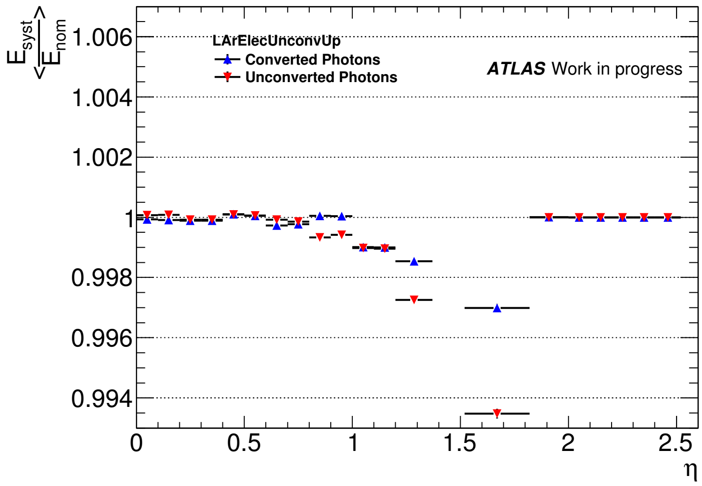


FIGURE 3.45: Photon Energy uncertainties coming E1/E2 modelling for electron and unconverted photons

- **E1/E2 modelling for unconverted photons**
  This terms comes from the various uncertainties to the E1/E2 calibration for unconverted photons with low energy deposits in the PS after correcting the effect affecting the E1/E2 from muons.

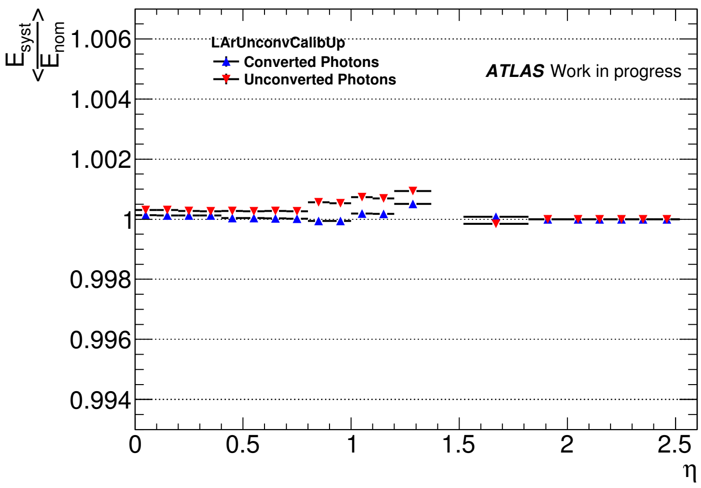


Figure 3.46: Photon Energy uncertainties coming from E1/E2 modelling for unconverted photon

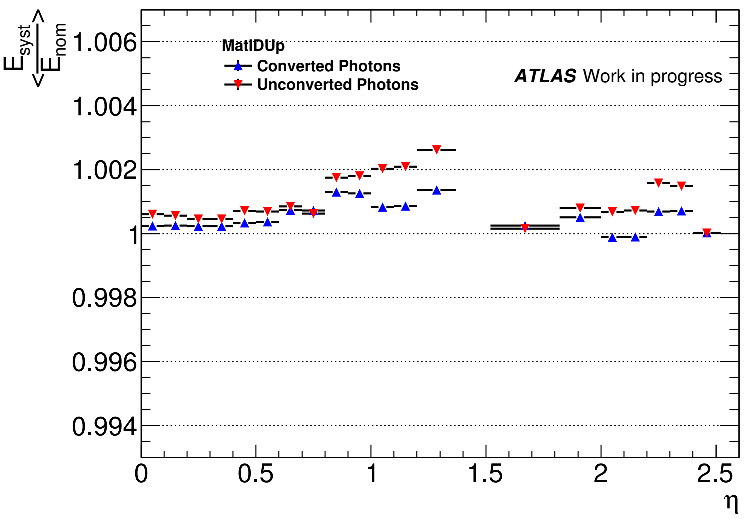


Figure 3.47: Photon Energy uncertainties coming from ID Material uncertainties

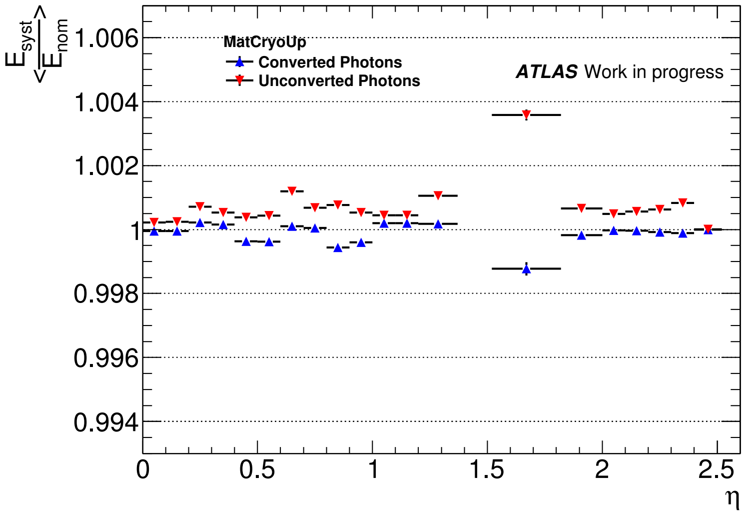


FIGURE 3.48: Photon Energy uncertainties coming from Cryo Material uncertainties

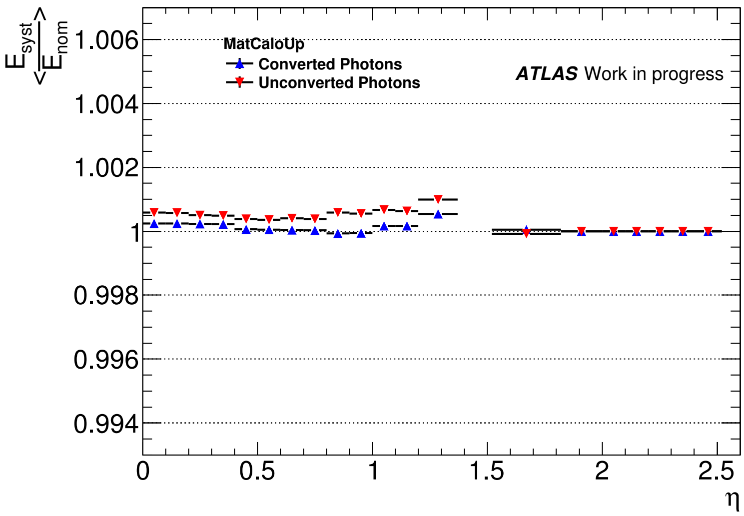


FIGURE 3.49: Photon Energy uncertainties coming from Calo Material uncertainties

## 3.9 Lateral leakage mis-modelling

Another important effect taken into account during the process of the calibration is shown development the lateral mis-modeling between photons and electron in the calorimeter. This effect is zero for electron from the Z which are used to extracted the $\alpha$ scale. In the case of photons the MC might mismodelling the description the the shower shape development and also the cluster size is different. This study was performed using radiative photons ($Z \rightarrow ll\gamma$) and electrons from the $Z \rightarrow e^+e^-$ in Data and MC. The nominal cluster energy of the electrons and radiative photons has been compared to the energy found in a larger window of size $\Delta\eta \times \Delta\phi = 7 \times 11$. The normalized difference:

$$\Delta(\gamma - e) = \left( \frac{E_{7\times 11} - E_{nom}}{E_{nom}} \right) \tag{3.29}$$

was studied for three pseudorapidity intervals, separating unconverted and converted photons. The most significant effects are ($0.29 \pm 0.08\%$) for converted photons($0.8 < |\eta| < 1.37$) and ($0.09 \pm 0.03\%$) for unconverted photons($|\eta| < 0.8$). The larger value in each bin is taken into account as systematic uncertainty. The impact of lateral leakage mismodeling on the energy scale is shown in fig 3.50.

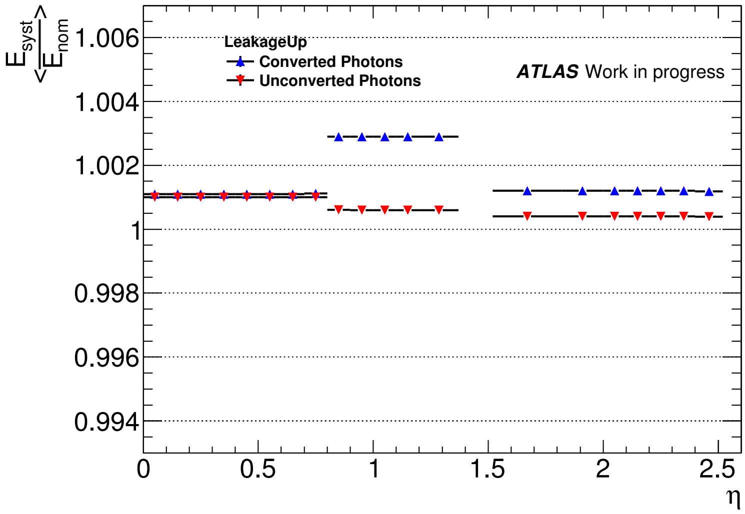


FIGURE 3.50: Photon Energy uncertainties coming from Lateral leakage mis-modelling

## 3.10 Photon conversion

The MC based calibration of the electromagnetic particles is done independently for electrons, converted photons and unconverted photons. Reconstructing an unconverted photons as a converted one would give a biased energy. In fact the energy of the photon would be overestimated as bigger corrections for energy loss in dead material would be applied. A true unconverted photons can be wrongly reconstructed as converted after the association a fake track of the ID. Last uncertainty to take into account is the possible wrong determination of the conversion radius due to dead pixel or STC modules. The impact on these 3 uncertainties on photon energy scale are shown:

- **Conversion Efficiency**:

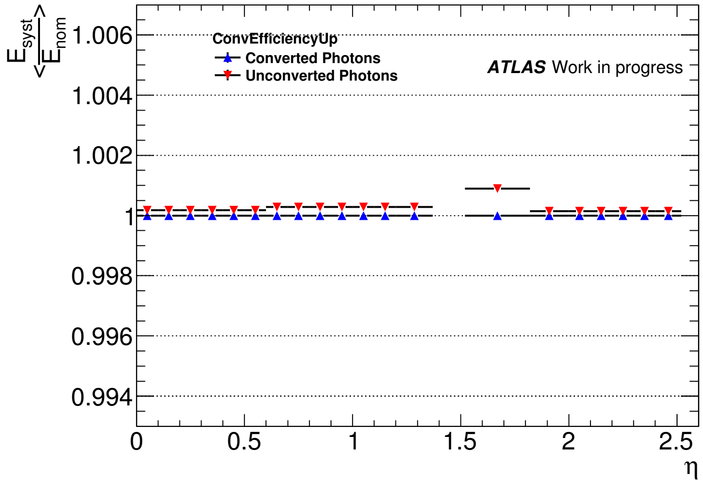


FIGURE 3.51: Photon Energy uncertainties coming from Conversion Efficiency

- **Conversion Fake Rate**:

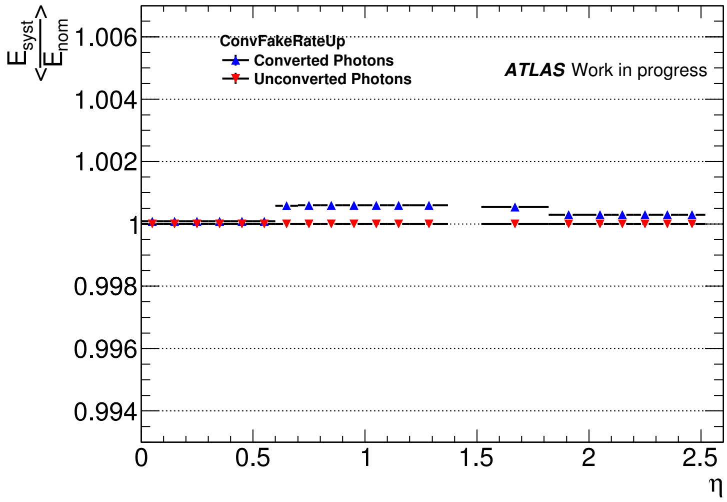


FIGURE 3.52: Photon Energy uncertainties coming from Conversion Fake Rate

- **Conversion Radius**:

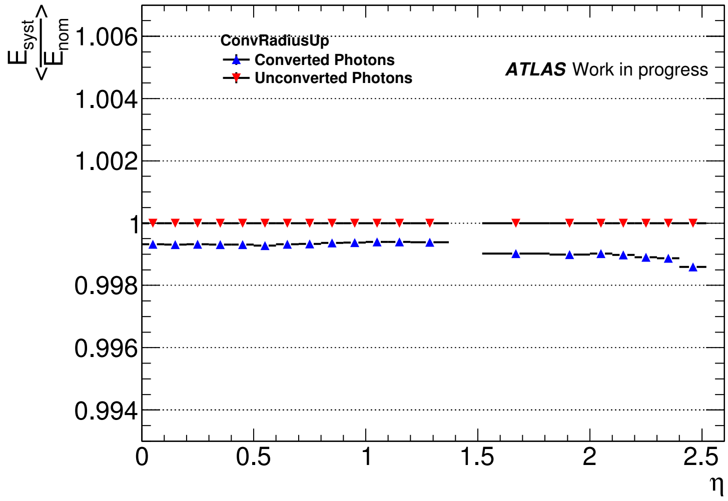


FIGURE 3.53: Photon Energy uncertainties coming from Conversion Radius

## 3.11 Geant4 systematic

The stability of the particle-matter interaction models provided by Geant4 9.4, the Geant4 version used by ATLAS during the LHC Run 1, were tested by simulating samples contains high-$E_T$ electrons with varied the physics list. Comparing different physics list allows to test the influence of bremsstrahlung and photon conversion on the developed of the EM showers. This test was performed using high-statistics $Z \to ee$ samples including or not pileup. The uncertainty related to Geant4 mismodeling on the photon energy scale is shown is Fig.3.54.

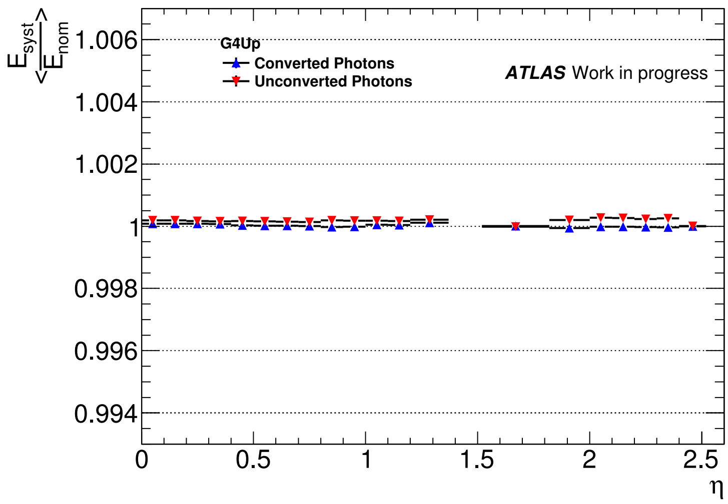


FIGURE 3.54: Photon Energy uncertainties coming from Geant4

## 3.12 Pedestal systematic

A small difference between the pedestal extracted from calibration runs and physics runs was found, that has an impact of about 10 MeV on energy computed from electromagnetic clusters. This effect is in average corrected for electrons at 40 GeV with the scale factor from the $Zee$ decay, but a small non-linearity can appear when going to different energy ranges. This bias has been taken as an uncertainty on the energy scale (Fig.3.55).

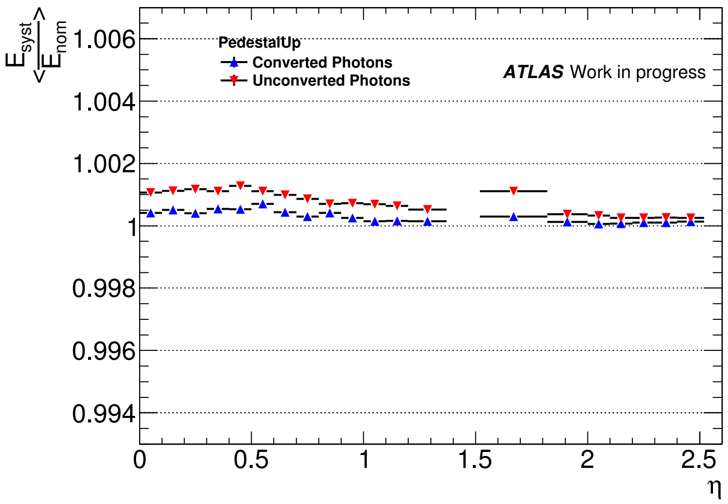


FIGURE 3.55: Photon Energy uncertainties coming from Pedestal

## 3.13 Photon Scale

The in-situ calibration applied to photons comes from $Z \to e^+e^-$ decays. The electron and photon behavior is not identical, therefore an electron to photon extrapolation has to be performed using MC simulation. A data-driven validation to the standard calibration is highly recommended to assure the best EM calorimeter performance, and is the purpose of the study of Z radiative decays. The goal of this study is to extract the photon energy scales in data directly from a clean photon sample from FSR (Final State Radiation ) events in order to validate the calorimeter calibration. For an $\eta$ or $E_T$ region $i$ after applying both the MVA Calibration (Sec 3.6) and the $Z \to e^+e^-$ in-situ corrections to the photons energy scale, any residual mis-calibration between data and MC can be parametrized as:

$$E_i^{MC} = \frac{E_i^{data}}{(1+\alpha_i)} \tag{3.30}$$

where $E_i^{\mathrm{MC}}$ and $E_i^{\mathrm{data}}$ are corrected photon energies in region $i$, for MC and data respectively, and $\alpha_i$ measures the residual mis-calibration in the photon energy scale (ES). The $\alpha_i$ energy-scale factors are extracted by comparing the three-body invariant mass distributions in data and MC in the following way:

1. The photon energy in data is shifted by $\alpha_i$ and the three-body invariant mass is recalculated.
2. The recalculated invariant mass distribution is compared to MC. The value of $\alpha_i$ that provides the best agreement in the distributions of data and MC is the residual miscalibration in the ES, which henceforth will be referred to as the "photon energy scale".

Collision data are compared to MC simulation. The photon scale are extracted from three different samples:

- $Z \to \mu\mu(\gamma)$ with collinear FSR
- $Z \to \mu\mu(\gamma)$ with non-collinear FSR
- $Z \to ee(\gamma)$ with non-collinear FSR

The results from the three analyses are used to produce a weighted combination of the photon scale in three different categories: unconverted (Figure 3.56), 1 track converted (Figure 3.57) and 2 track converted (Figure 3.58).As can be seen from mentioned figures the in-situ scale for photons agree with the ones from electrons within the quoted uncertainties.

## 3.14 Electron calibration cross checks

At this point, the electron energy scale is fully specified; after all corrections are applied, the energy response is expected to be linear and uniform. Another cross check is done categorizing the electrons that decay from Z as a function of transverse energy in broad pseudorapidity intervals, with the following boundaries:

- $|\eta|$ : 0 - 0.6 - 1 - 1.37 - 1.55 - 1.82 - 2.47
- $E_T$ : 27 - 35 - 42 - 50 - 100 GeV.

The analysis is performed after applying all corrections derived above, so that the fitted energy scales are expected close to 0 and linear. The results are shown in Figure 3.59. The $J/\psi$-based energy scales are also reminded. In all cases, the energy scales found in the present section lie within the *a priori* uncertainty envelope.

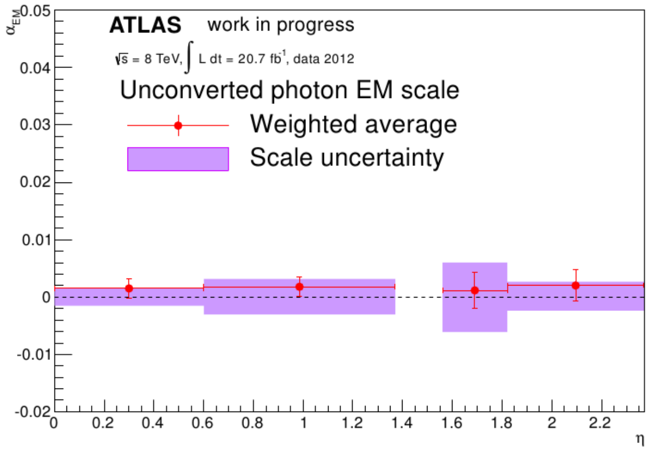


FIGURE 3.56: Figure 33: Combination of scale factors from all unconverted FSR photons in bins of photon $\eta$ (red circles). The violet band around zero represents the systematic uncertainty associated to the electron scale from $Z \to ee$ calculations. The vertical uncertainties on the points are statistical and systematic added in quadrature.

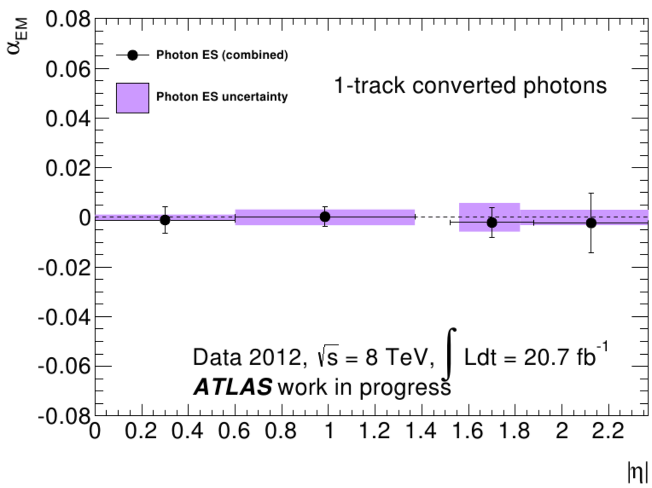


FIGURE 3.57: Combination of scale factors from all converted 1-track FSR photons in bins of photon $\eta$.The violet band around zero represents the systematic uncertainty associated to the electron scale from $Z \to ee$ calculations. The vertical uncertainties on the points are statistical and systematic added in quadrature.

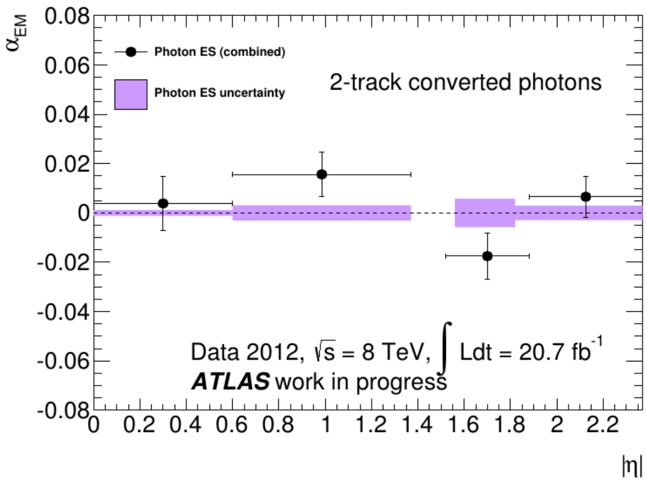


FIGURE 3.58: Combination of scale factors from all converted 2-track FSR photons in bins of photon $\eta$.The violet band around zero represents the systematic uncertainty associated to the electron scale from $Z \rightarrow ee$ calculations. The vertical uncertainties on the points are statistical and systematic added in quadrature.

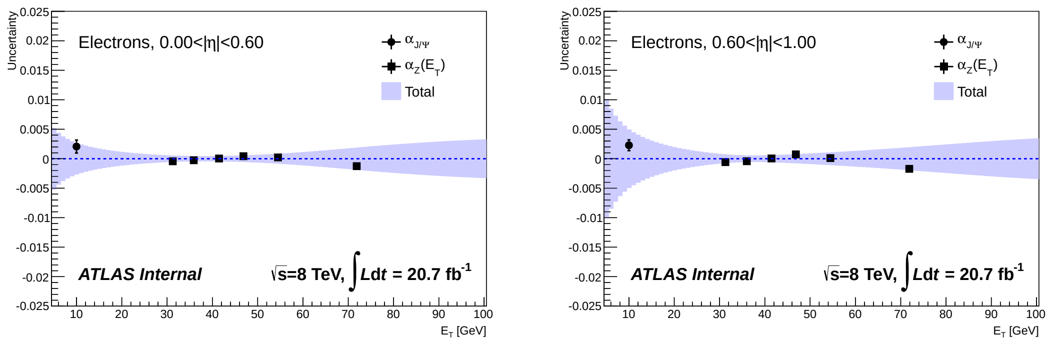


FIGURE 3.59: Comparison of the scale factors extracted from the $J/\psi$ sample with the ones measured in the Z sample as a function of the electron energy in different pseudo-rapidity bins.

# Chapter 4

# The $H \to \gamma\gamma$ Analysis

This chapter describes the study about the mass measurement of the Higgs boson mass in the di-photon decay channel.

## 4.1 Event Selection

In this study data recorded in 2012 with the ATLAS experiment at the LHC are used. This corresponds to 20.3 $fb^{-1}$ of data at the center of mass energy of $\sqrt{s}$= 8 TeV.Figure4.1 shows the evolution of the collected luminosity during the data taking. The average number of collision per bunch crossing is about 21 (Figure 4.2)

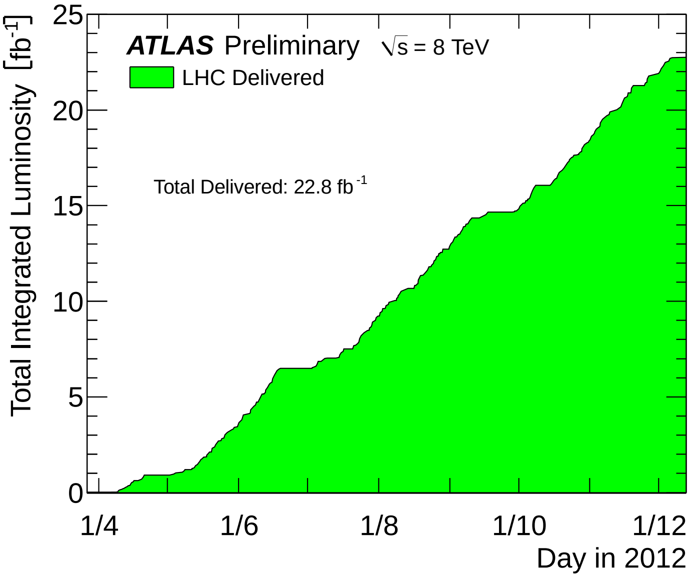


FIGURE 4.1: Integrated Luminosity for the 2012 data taking [44]

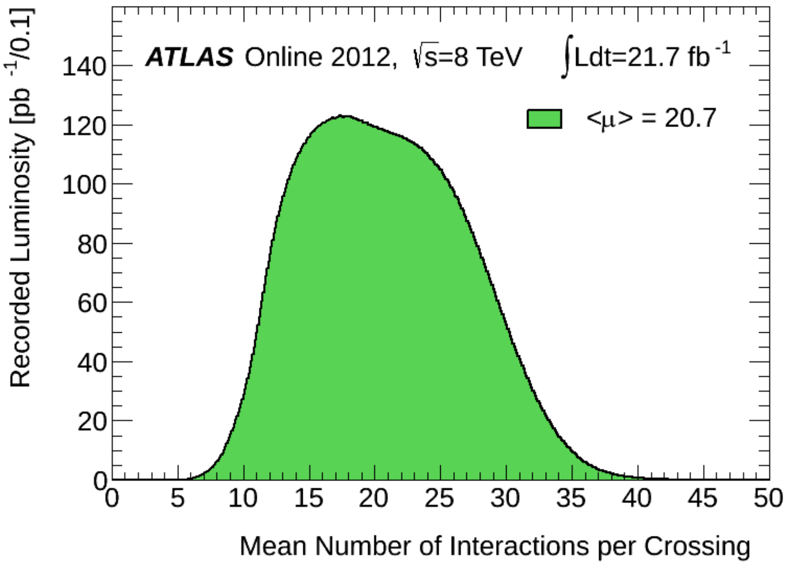


FIGURE 4.2: Distribution of the mean number of interactions per bunch crossing in 2012 data taking [44]

### 4.1.1 Diphoton events selection.

The candidates are first preselected with the following criteria:

- The run number and Luminosity Block need to be contained in the Good Run List (GRL).The GRL is the list of the Runs and the LumiBlocks that are suitable for this physics analysis.
- The events need to pass specific trigger chains requiring at least two photons with loose identification criteria and with transverse momentum of at least 35 and 25 GeV for the leading and the sub-leading photons ($g35\_loose\_g25\_loose$).
- Photons are considered as candidates only if reconstructed in the fiducial region of the calorimeter $|\eta_{s2}| < 1.37$ or $1.52 < |\eta_{s2}| < 2.37$ where $\eta_{s2}$ correspond to the photon pseudo-rapidity in the second sampling of the calorimeter. The barrel to endcap transition region is excluded, as photons in this region suffer from a worse reconstruction due to the large amount of material upstream the calorimeter.
- In the event, At least two reconstructed photons with a tight identification criteria are required.

The candidates are then selected following the signature of Higgs boson decaying in two photons:

- A kinematic cut is applied on the ratio between the transverse momentum of the leading (sub-leading) photon and the di-photon invariant mass $m_{\gamma\gamma}$:

$$\left(\frac{p_{T1}}{m_{\gamma\gamma}}\right) > 0.35 \qquad \left(\frac{p_{T2}}{m_{\gamma\gamma}}\right) > 0.25 \tag{4.1}$$

- The selection of the primary vertex is crucial as it has an impact on the accuracy of the invariant di-photon mass and the signal resolution. Several method has been developed to reconstructed this vertex. In this analysis the longitudinal segmentation of the calorimeter is exploited. The pointing method is the ability to measured the direction of the photon using the sampling in the first and in the second layer in case of unconverted photon or the first layer and the conversion vertex for converted photon. If the photon is converted, the position of the conversion vertex is also used if tracks from the conversion have hits in the silicon detectors. The vertex is finally chosen thanks to a neural network which combines the photon pointing with, for each reconstructed vertex: the conversion information, the sum of the squared momentum $\sum p_T^2$ and the scalar sum of the momentum $\sum p_T$ of the tracks associated with each reconstructed vertex, and the difference in azimuthal angle $\Delta\phi$ between the direction of the vector sum of the tracks momenta and that of the di-photon system.

- The cluster should be isolated in order to remove the fake photons coming from hadronic decays. The type of isolation criteria are required:

  1. **Track isolation**: The sum of the transverse momentum of the tracks inside a cone of $\Delta R = \sqrt{(\Delta\eta)^2 + (\Delta\phi)^2} = 0.2$ around the photon lower than 2.6 GeV.
  2. **Calorimeter isolation**: The sum of energy reconstructed in topological cluster with positive energy in a cone of $\Delta R = 0.4$ around the photon lower than 6 GeV.

## 4.2 Diphoton mass reconstruction

The analysis try to search a resonance in the di-photon invariant mass distribution over a large of monotonic falling background. The di-photon invariant mass is reconstructed with:

$$m_{\gamma\gamma} = \sqrt{2E_{T1}E_{T2}\left(\cosh\Delta\eta + \cos\Delta\phi\right)} \tag{4.2}$$

where $E_{T1}$,$E_{T2}$ are the transverse energies of the leading and the sub-leading photon, $\Delta\phi$ is the difference in azimuthal angle between the two photons. The resolution of the mass depends then on the primary vertex selection efficiency and on the resolution on the photon energy. Events are selected in a the $m_{\gamma\gamma}$ range of $[105, 160]$ GeV.

## 4.3 Signal Model

The signal mode is derived using MC simulation on $H \to \gamma\gamma$ sample considering all the Higgs production modes taking into account their BR. The production of a Higgs boson through the gluon-gluon fusion and the Vector Boson Fusion processes is modeled with the generator POWHEG [45] interfaced with PYTHIA 8 [46] for the generation of the parton showers and their hadronization. The production of the Higgs boson in association with vector bosons or top quark pairs is modeled with the PYTHIA 8 generator. The Higgs boson production and decay are simulated for 11 values of the Higgs boson mass in 5 GeV steps from 100 to 150 GeV.

The five dominant production modes are simulated for each mass value. The normalization and factorization scales are set to the Higgs mass.

The Higgs boson Branching Ratio into two photons and its uncertainty as a function of the Higgs boson mass are calculated using the Hdecay program [47] and are taken from references [19, 48]. The sets of parton distribution functions used correspond to Ct10 [49] for the Powheg generator and to Cteq6l1 [50] or Mrstmcal[51] for the Pythia generator. The pileup is modeled in these simulations following the conditions observed in data by summing up additional simulated inelastic proton-proton collisions. A 50 ns bunch spacing is simulated. The full simulation[52] of the ATLAS detector is made using the Geant4 [53] program.

### 4.3.1 Description of the Signal Model

The mass distribution for the $H \rightarrow \gamma\gamma$ signal is modeled from MC simulations using the full selection presented above. The various production are weighted according to their cross sections (gluon-gluon fusion, VBF, VH, $t\bar{t}H$). For a fixed Higgs mass $m_H$ a the sum of a Crystal Ball (CB) function and a Gaussian (Ga) distribution is used to model the distribution. The CB function describes the bulk of the events which have a narrow Gaussian spectrum in the peak region and tails toward lower reconstructed mass while the Gaussian distribution with a wide width describes the far outliers in the distribution. The Crystal Ball function $F_{CB}$ is defined as:

$$N \cdot \begin{cases} \exp\left(-t^2/2\right) & \text{if } t > -\alpha_{CB} \\ \left(\frac{n_{CB}}{\alpha_{CB}}\right)^{n_{CB}} \cdot e^{-\alpha_{CB}^2/2} \cdot \left(\frac{n_{CB}}{\alpha_{CB}} - \alpha_{CB} - t\right)^{-n_{CB}} & \text{otherwise} \end{cases}$$

where $t = \frac{(m_{\gamma\gamma}-\mu_{CB})}{\sigma_{CB}}$, $N$ is a normalization parameter, $\mu_{CB}$ and $\sigma_{CB}$ are the the peak and the resolution of the Gaussian distribution for the core component. $n_{CB}$ and $\alpha_{CB}$ parametrize the non-Gaussian tail of the Crystal Ball. The parameter $n_{CB}$ is set equal to 10.

The wide Gaussian distribution has a maximum equal to $\mu_{GA}$, different from $\mu_{CB}$, and a standard deviation $\kappa_{GA} \cdot \sigma_{CB}$. The parameter $f_{CB}$ represent the fraction of CB in the composition of the Gaussian and Crystal Ball.

The parametrization of the signal model can be written as:

$$C = f_{CB} \cdot F_{CB}(m_{\gamma\gamma}, \mu_{CB}, \sigma_{CB}, \alpha_{CB}) + (1 - f_{CB}) \cdot F_{Ga}(m_{\gamma\gamma}, \mu_{Ga}, \kappa_{Ga} \cdot \sigma_{CB}). \tag{4.3}$$

In order to get a model describing the signal for any $m_H$ (the global model), the Crystall Ball + Gaussian model is parametrized with respect to $m_H$. The parameters $\mu_{CB}, \sigma_{CB}, \mu_{Ga}$ are described by a linear function of $m_H$. $\alpha_{CB}$, $f_{CB}$, $\kappa_{Ga}$ are considered constant. For example $\mu_{CB}$ is described as:

$$\mu_{CB}(m_H) = m_H + \mu_{CB}\left(m_H = 125\,GeV\right) + s_\mu \cdot \left(m_H - 125\,GeV\right) \tag{4.4}$$

and similarly for $\mu_{Ga}$. $\sigma_{CB}$ is described as:

$$\sigma_{CB}(m_H) = \sigma_{CB}(m_H = 125\,GeV) + s_{\sigma_{CB}}(m_H - 125\,GeV) \tag{4.5}$$

Using all the available signal samples between $m_H = 100$ GeV and 150 GeV, an unique global fit is done to extract the parameters describing the dependence of the Crystall Ball plus Gaussian model with respect to $m_H$. Therefore, for each category, nine parameters describe the global signal model: $\mu_{CB}(m_H = 125\ GeV)$, $\mu_{Ga}(m_H = 125\ GeV)$, $\sigma_{CB}(m_H = 125\ GeV)$, $s_{\mu_{CB}}$, $s_{\mu_{Ga}}$, $s_\sigma$, $f_{CB}$, $\alpha_{CB}$, $k_{Ga}$. After the determination of the signal model its parameters are frozen and used in the analysis.

## 4.4 Categorization optimization

The process that lead to the choice of the optimized categorization for the mass measured will be described in this section. The research of optimized categories is useful for increasing the sensitivity of the signal [40].

The main ingredient that were used to define an interesting categorization are:

- The resolution of a MC sample $H \to \gamma\gamma$ ($m_H = 125\,GeV$)
- The expected number of signal events $s$ and the expected number of background events $b$ are estimated as the number of selected signal (background) events in a window $\pm 2\sigma$
- The significance calculates as the ratio $z = \frac{s}{\sqrt{b}}$
- The ratio $\frac{\sigma}{z}$

A lot of different categories have been defined:

`EPS` **(5 categories)** :

1. Both photons unconverted and central
2. Both photons unconverted, at least one not central, both not in transition region
3. Both photons unconverted, at least one photon in transition region
4. At least one photon converted, both photons central
5. At least one photon converted, at least one not central, both not in transition region

where "central" and "transition" mean respectively $|\eta_{s2}| < 0.75$ and $1.3 < |\eta_{s2}| < 1.75$. See

`eEPS` **(6 categories)** as `EPS`, but splitting unconverted categories in three regions, as for converted categories.

`eEPS85` **(6 categories)** as `eEPS`, but moving the central edge from $|\eta_{s2}| = 0.75$ to $|\eta_{s2}| = 0.85$.

**`eEPS95` (6 categories)** as `eEPS`, but moving the central edge from $|\eta_{s2}| = 0.75$ to $|\eta_{s2}| = 0.95$.

**`eEPS12` (6 categories)** as `eEPS`, but moving the transition edge from $|\eta_{s2}| = 1.3$ to $|\eta_{s2}| = 1.2$.

**`eEPS14` (6 categories)** as `eEPS`, but moving the transition edge from $|\eta_{s2}| = 1.3$ to $|\eta_{s2}| = 1.4$.

**`vfEPS` (7 categories)** as in `fEPS`, but splitting the endcap category in two further regions. For this categorization there is no splitting into conversion status.

**`vfEPSconv` (11 categories)** as `vfEPS` but splitting the first four categories in two, according to the conversion status (as in `EPS`).

**`ptt` (9 categories)** as `EPS`, but splitting all the categories, except the transition one in high/low-$p_{Tt}$, where high-$p_{Tt}$ mean $p_{Tt} > 60\,\mathrm{GeV}$.

**`ptt30` (9 categories)** as in `ptt` but using different definition of high-$p_{Tt}$: $p_{Tt} > 30\,\mathrm{GeV}$

**`ptt40` (9 categories)** as in `ptt` but using different definition of high-$p_{Tt}$: $p_{Tt} > 40\,\mathrm{GeV}$

**`ptt70` (9 categories)** as in `ptt` but using different definition of high-$p_{Tt}$: $p_{Tt} > 70\,\mathrm{GeV}$

**`ptt80` (9 categories)** as in `ptt` but using different definition of high-$p_{Tt}$: $p_{Tt} > 80\,\mathrm{GeV}$

**`eEPSptt60` (10 categories)** as `eEPS`, but splitting all the categories, except the transitions ones, according to $p_{Tt} \lessgtr 60\,\mathrm{GeV}$.

**`eEPSptt70` (10 categories)** as `eEPS`, but splitting all the categories, except the transitions ones, according to $p_{Tt} \lessgtr 70\,\mathrm{GeV}$.

**`fEPS` (8 categories)** as `eEPS`, but splitting in different $|\eta_{s2}|$ regions

**`fEPSptt` (12 categories)** as `fEPS` but splitting category 2, 4, 6, 8 in high/low-$p_{Tt}$.

**`untagged9570` (4 categories)** events are split in two pseudorapidity regions: one central region where both two photons have $|\eta_{s2}| < 0.95$, and one not central. At the same time categories are splitted using $p_{Tt} \lessgtr 70\,\mathrm{GeV}$.

**`Moriond MVA` (14 categories)** As `ptt`, adding 5 more categories dedicated to VBF and VH production processes. There are a one-lepton category (VH), a missing transverse energy category (VH), a low mass two-jets category (VH), and two high mass two-jets category (VBF) with loose and high selection, done with a MVA analysis.

**`foureta` (16 categories)** dividing $|\eta_{s2}^{(1)}| \times |\eta_{s2}^{(2)}|$ in 16 regions using $[0.8, 1.37, 1.8, 2.37]^2$. For this categorization there is no spitting into conversion status.

**`fouretasym` (10 categories)** as `foureta`, but considering symmetric categories to be the same.

**`fouretasymconv` (12 categories)** as `fouretasym` but splitting the first two categories in two unconverted/at least one converted

**`resolution` (4 categories)** : events are divided in four categories depending on the expected resolution. The expected resolution is computed as the truncated RMS, as described at the beginning of the section. The four regions in resolution are $[0, 1.2, 1.45, 1.75, \infty]$ GeV.

**`resolution2` (5 categories)** : similar to the **`resolution`** categorization, but using different resolution regions: $[0, 1.1, 1.25, 1.5, 1.7, \infty]$ GeV.

For each of the categorization describes above the following procedure is made in order to estimate the total expected mass error. This optimization is done using generated Asimov dataset with an injected Higgs mass at $m_H = 126.5$ GeV and signal strength parameter $\mu = 1, 1.5$. First step of the procedure is to produce for each of the categories the global signal model described in Section 4.3. A background shape parametrization has to be chosen between simple function (expo,bern4,...) in order to reproduce the $\gamma\gamma$ irreducible background. The parameters of the background fit are extracted directly on data. The systematics uncertainties related to the peak position described in Chapter 3 are implemented as Gaussian nuisance parameters for all the categories. Starting from this signal plus background model, an Asimov dataset is generated. At this point a fit at $m_H = 126.5$ can be done and the systematics and the statistical error can be extracted. The best categorizations with the minimum total error are taken into account.

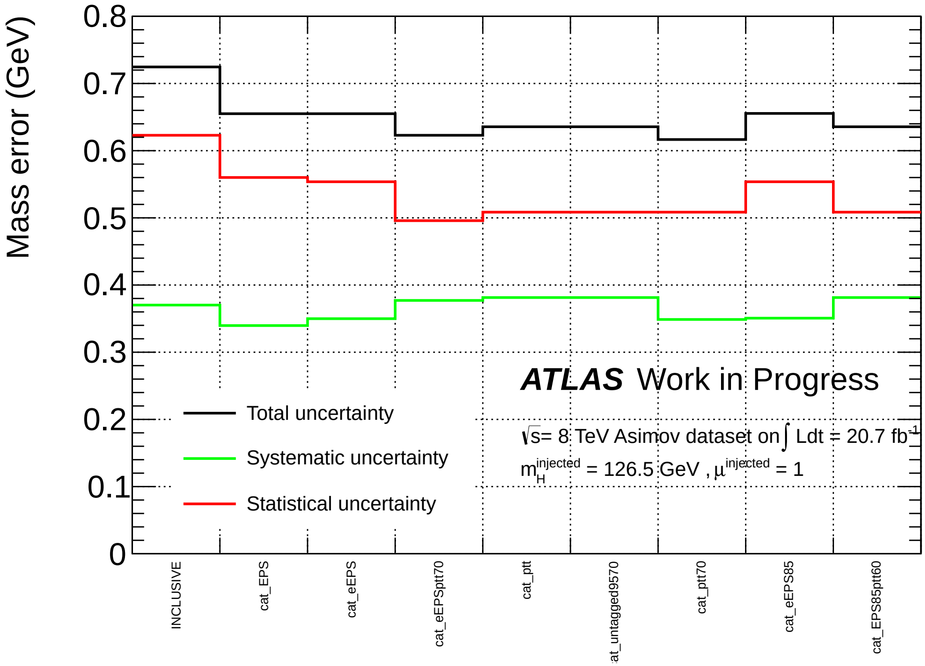


FIGURE 4.3: Total, statistic and systematic expected mass errors for various categories using Asimov datasets for $\mu = 1$ and injected $m_H = 126.5 GeV$.

## 4.5 Selected Categorization

Some of the categories described in the previous section have the same total mass error. In order to simplified the mass measurement it has been decided to choose the eEPSptt70 as baseline. This choice is motivated by different reason: the resolution of the photons is the best in the central barrel region of the calorimeter and worst in the transition region, and is better for unconverted photon than converted ones. Therefore have been chosen a classification which takes into account the geometry of the detector, properties of the photon (converted or unconverted) and a further

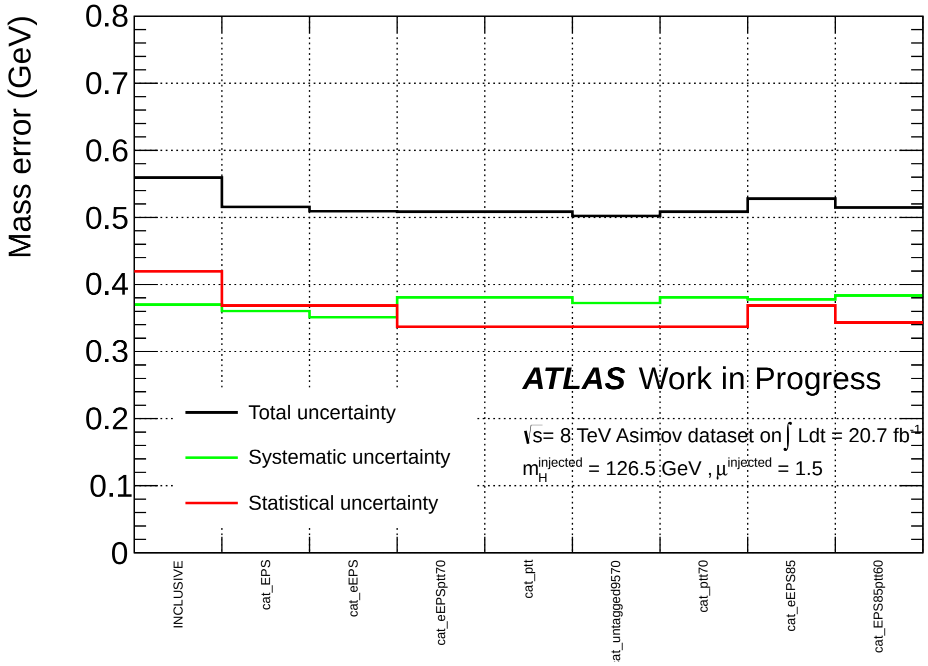


FIGURE 4.4: Total, statistic and systematic expected mass errors for various categories using Asimov datasets for $\mu = 1.5$ and injected $m_H = 126.5 GeV$.

cut in the variable $p_{Tt}$. It corresponds to the component of the $p_T$ vector transverse to the improperly called "thrust axis". The thrust vector is defined as follow:

$$\begin{aligned} p_{x,thrust} &= p_{x,1} - p_{y,2} \\ p_{y,thrust} &= p_{x,2} - p_{y,2} \end{aligned} \tag{4.6}$$

$$p_{Tt} = 2 \cdot |p_{x,1} \cdot \hat{p}_{y,thrust} - p_{y,1} \cdot \hat{p}_{x,thrust}| \tag{4.7}$$

with the indices 1 and 2 denoting the leading and the sub-leading photons, and the $\hat{p}_{thrust}$ the thrust vector normalized to unit vector (Fig. 4.5).

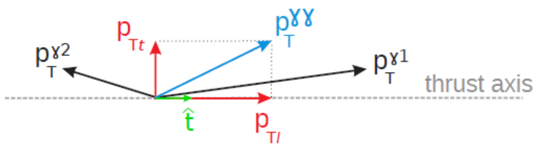


FIGURE 4.5: Sketch of the $p_{Tt}$ definition

This categorization is based on 10 categories, all untagged with respect to a particular production process. The quantities used to define the categories are: $|\eta_{s2}|$ of the photons, $p_{Tt}$ of the diphoton system and the conversion status of the photons. For the categorization the conversion status definition match the one used in the calibration: a converted photon is a photon with an associated conversion vertex with a radius less than 800 mm.

- **C1:** Both photon candidates are unconverted, and have $|\eta_{s2}| < 0.75$; the diphoton system has $p_{Tt} < 70\, GeV$.

- **C2:** Both photon candidates are unconverted, and have $|\eta_{s2}| < 0.75$; the diphoton system has $p_{Tt} > 70\,GeV$.
- **C3:** Both photon candidates are unconverted and at least one candidate has $|\eta_{s2}| > 0.75$; the diphoton system has $p_{Tt} < 70\,GeV$.
- **C4:** Both photon candidates are unconverted and at least one candidate has $|\eta_{s2}| > 0.75$; the diphoton system has $p_{Tt} > 70\,GeV$.
- **C5:** Both photon candidates are unconverted and at least one candidate is in the range $1.3 < |\eta_{s2}| < 1.37$ or $1.52 < |\eta_{s2}| < 1.75$.
- **C6:** At least one photon candidate is converted and both photon candidates have $|\eta_{s2}| < 0.75$; the diphoton system has $p_{Tt} < 70\,GeV$.
- **C7:** At least one photon candidate is converted and both photon candidates have $|\eta_{s2}| < 0.75$; the diphoton system has $p_{Tt} > 70\,GeV$.
- **C8:** At least one photon candidate is converted and both photon candidates have $|\eta_{s2}| < 1.3$ or $|\eta_{s2}| > 1.75$, but at least one photon candidate has $|\eta_{s2}| > 0.75$.
  The diphoton system has $p_{Tt} < 70\,GeV$.
- **C9:** At least one photon candidate is converted and both photon candidates have $|\eta_{s2}| < 1.3$ or $|\eta_{s2}| > 1.75$, but at least one photon candidate has $|\eta_{s2}| > 0.75$.
  The diphoton system has $p_{Tt} > 70\,GeV$.
- **C10:** At least one photon candidate is converted and at least one photon candidate is in the range $1.3 < |\eta_{s2}| < 1.37$ or $1.52 < |\eta_{s2}| < 1.75$.

## 4.6 Background Model

The proper understanding of the diphoton background is important to correct assess its impact on the analysis. Three different high statistics background-only MC samples are used to model the three main background components($\gamma\gamma$, $\gamma$-jet, jet-jet). The prompt diphoton and the photon-jet background are obtain with SHERPA [54]. The jet-jet component is generated with Pythia8. The samples are mixed using as fractions: 77%, 20%,3% [55]. The Drell-Yan component, about 0.8% of the total background, does not significantly affect the shape of the background and is not considered. Due to the high statistic of the MC samples (about 1000 times the expected background in data) it is not feasible to simulate a full detector response. For this reason the detector response to photons is parametrized as a smearing which depends on the transverse momentum, pseudorapidity and conversion status. This procedure takes into account the varying resolutions and reconstruction efficiencies of different detector regions. For jets, the particle level definition of the variable is smeared using a detector response matrix. This response matrix is derived from a sample of fully simulated diphoton plus jets events. For this reason such a simulation is called "smeared Monte Carlo". The bias of a given parametrization is estimate by fitting the smeared MC samples with a function combining the signal model, described in

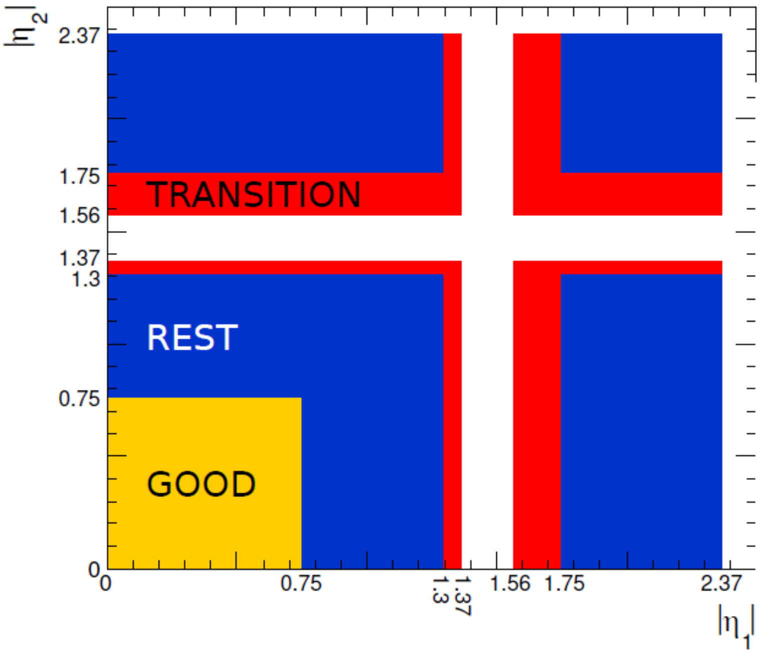


FIGURE 4.6: Graphic representation of the choosen categorization. The representation is duplicated in the case of both unconverted photons (C1-C5) or at least one converted photon (C6-C10)

Section , and background model. A given parametrization is kept if the numbers of signal events extracted from this fit $N_{sp}$ (called "spurious signal") satisfy at least one of the two criteria:

- $N_{sp} < 10\% N_{S,exp}$
- $N_{sp} < 20\% \sigma_{background}$

where $N_{S,exp}$ is the expected number of $H \to \gamma\gamma$ signal passing the selection and $\sigma_{background}$ is the statistical uncertainty on the number of background events.

Exponential decreasing function and exponential of a $2^{nd}$ order polynomial functions have been selected for the 2012 dataset, and for the baseline categorization described in Section 4.5. See Table 4.1.

## 4.7 Systematics uncertainty

The main source of uncertainty for the mass measurement is the determination of the mass energy scale. This scale comes from the propagation of the photon energy scale, described in Chapter 3, to the mass scale and this lead an uncertainty on the $H \to \gamma\gamma$ peak position.
Two different correlation model have been tested: The **Full Model** and **Simplified Model** are characterizer in Table 4.2

The Full Model divides all the energy scale uncertainties into 64 independent effect. This reflects the measurement of the uncertainties and the understanding of the source of the uncertainty.

| Category | $N_{S,exp}$ | $\sigma_{backg}$ | Parametrization | Uncertainty $[N_{sp}]$ |
|---|---|---|---|---|
| Unconverted central, low $p_{\mathrm{Tt}}$ | 58.7 | 34.0 | Exp. of $2^{nd}$ order pol. | 3.5 |
| Unconverted central, high $p_{\mathrm{Tt}}$ | 7.6 | 6.1 | Exponential | 0.3 |
| Unconverted rest, low $p_{\mathrm{Tt}}$ | 100.9 | 73.7 | Exp. of $2^{nd}$ order pol. | 4.4 |
| Unconverted rest, high $p_{\mathrm{Tt}}$ | 10.0 | 11.9 | Exponential | 1.6 |
| Unconverted transition | 23.3 | 36.5 | Exp. of $2^{nd}$ order pol. | 1.7 |
| Converted central, low $p_{\mathrm{Tt}}$ | 34.3 | 28.2 | Exp. of $2^{nd}$ order pol. | 2.7 |
| Converted central, high $p_{\mathrm{Tt}}$ | 4.8 | 5.5 | Exponential | 0.2 |
| Converted rest, low $p_{\mathrm{Tt}}$ | 96.7 | 75.1 | Exp. of $2^{nd}$ order pol. | 4.6 |
| Converted rest, high $p_{\mathrm{Tt}}$ | 12.3 | 15.0 | Exponential | 2.6 |
| Converted transition | 43.8 | 68.8 | Exp. of $2^{nd}$ order pol. | 3.7 |
| Inclusive | 416.8 | 139.9 | Exp. of $2^{nd}$ order pol | 11.3 |

TABLE 4.1: List of the functions chosen to fit the background and the associated systematic uncertainties for the different categories, using the 2012 dataset. The variables $N_{S,exp}$ and $\sigma_{backg}$ that are used to select the model are also given for information.

| Source of systematic Uncertanty | Full Model | NP | Simplified Model | NP |
|---|---|---|---|---|
| Zee Syst | Fully Correlated | 1 | Fully Correlated | 1 |
| Zee Stat | Fully Correlated | 1 | | |
| Lateral Leackage | Fully Correlated | 1 | Fully Correlated | 1 |
| Gain | Fully Correlated | 1 | Fully Correlated | 1 |
| E1/E2 Scale | Decorrelated in bins 0.2 | 12 | Decorrelated Barrel/Endcap | 2 |
| PS Scale | Decorrelated in PS modules | 8 | Decorrelated Barrel/Endcap | 2 |
| Lar E1/E2 modeling for e/conv | Decorrelated Barrel/Endcap | 2 | Decorrelated Barrel/Endcap | 2 |
| Lar E1/E2 modeling for unconv | Decorrelated Barrel/Endcap | 2 | Decorrelated Barrel/Endcap | 2 |
| Lar calibration | Decorrelated Barrel/Endcap | 2 | Decorrelated Barrel/Endcap | 2 |
| Lar calibration for e ($\eta > 1.8$) | Fully Correlated | 1 | Fully Correlated | 1 |
| Material ID | Decorrelated 4 bins | 4 | Decorrelated 4 bins | 4 |
| Material Cryo | Decorrelated in bins 0.2 | 12 | Decorrelated Barrel/Endcap | 2 |
| Material Calo | Decorrelated in bins 0.2 | 12 | Decorrelated Barrel/Endcap | 2 |
| Geant 4 Modelling | Fully Correlated | 1 | Fully Correlated | 1 |
| Conversion fake rate | Fully Correlated | 1 | Fully Correlated | 1 |
| Conversion Inefficency | Fully Correlated | 1 | Fully Correlated | 1 |
| Conversion Radius | Fully Correlated | 1 | Fully Correlated | 1 |
| Pedestal | Fully Correlated | 1 | Fully Correlated | 1 |
| Total numbers of NPs | | 64 | | 27 |

TABLE 4.2: Full and Simplified Correlation Model

In particular 12 bin in $\eta$ are used for the determination of the uncertainties of the E1/E2 scale, the cryo material and the calo material. Eight bin in $\eta$ are used for the PS systematics in order to follow the modules segmentation. Four bin are used for the material ID uncertainties (0-1.1-1.5-2.1-2.5).

The Simplified Model has been chosen for the $H \to \gamma\gamma$ mass analysis: the uncertainty coming from the PS scale, the strips/middle relative scale, the material in the cryostat and in the calorimeter are not anymore uncorrelated in such fine bins, but instead taken as uncorrelated in barrel and endcap region being quadratically summed to give the overall two systematics. This choice has been made to reduce the number of nuisance parameters since no other important advantage has been highlighted in the choice of the full model. The simplified is based on 27 independent energy scale systematics.

### 4.7.1 Impact on $m_{\gamma\gamma}$ peak position

In order to propagate the photon energy uncertainties described in Chapter 3 to an uncertainty to the mass scale, MC samples were generated applying one by one the uncertainties. From this sample several methods have been used to estimate the mass shift of $H \to \gamma\gamma$.

- **Mean in a Window:** In this method the diphoton invariant mass distribution is built with the nominal photon energy in the window [120,130] GeV. From this window the mean (M) and the RMS is extracted. A new mass window is extracted between [M-1.5 RMS,M+2 RMS]. The mean in this recomputed in this new window and it corresponds to the nominal peak position $P_{Nom}$. After the variation of the energy scale, the same procedure is computed and the distorted peak position $P_{bias}$ is evaluated. The final uncertainty on the peak position is computed as:
$$\theta_i = \frac{P_{bias} - P_{nom}}{P_{nom}} \tag{4.8}$$
- **Gaussian Peak:** This method is similar to the previous but instead of the mean a gaussian peak is extracted in the window [M-RMS,M+RMS] and the shift of the gaussian peak is quoted as the effect on the mass. The mean and the RMS are evaluated in a window [115,135] GeV.
- **Mean** In this method no window is defined. The mean is computed in the whole range. This method is bias by tails and outliers in the distribution and is not really a quantification of the shift of the peak.
- **Average Bias:** This method compute the systematics on the mass as the average bias defined as:
$$\theta_i = \left\langle \frac{m_{\gamma\gamma}^{bias} - m_{\gamma\gamma}^{nom}}{m_{\gamma\gamma}^{nom}} \right\rangle \tag{4.9}$$
where the mean is computed averaging all the events in th MC without using any window.
- **Full Fit** For this method a CB+Gaussian fit is done for every systematics. The systematics is quoted are the difference of the CB peak.
- **$m_H$ bias:** Contrary to the other methods this estimation focuses on the fitted Higgs mass and not to the diphoton invariant mass. For every systematic variation a signal-only sample is made from the events of the ggH(125) simulation passing the selection applying to them one energy scale variation. Then this sample is fitted with the nominal signal model (see section 5) and the estimated Higgs mass $m_H^{bias}$ is compared with the one obtained in the same way, but considering a nominal sample, without energy bias. The mass scale systematic is computed as
$$\theta_i = \frac{m_H^{bias} - m_H^{nom}}{m_H^{nom}} \tag{4.10}$$

All the method are consistent. The Full Fit and the Gaussian peak shows some discrepancy compared to the other. The chosen method for the mass analysis is the *$m_H$ bias*. All the contribution of uncertainties are plotted in Figure 4.7-4.11 comparing the various methods.

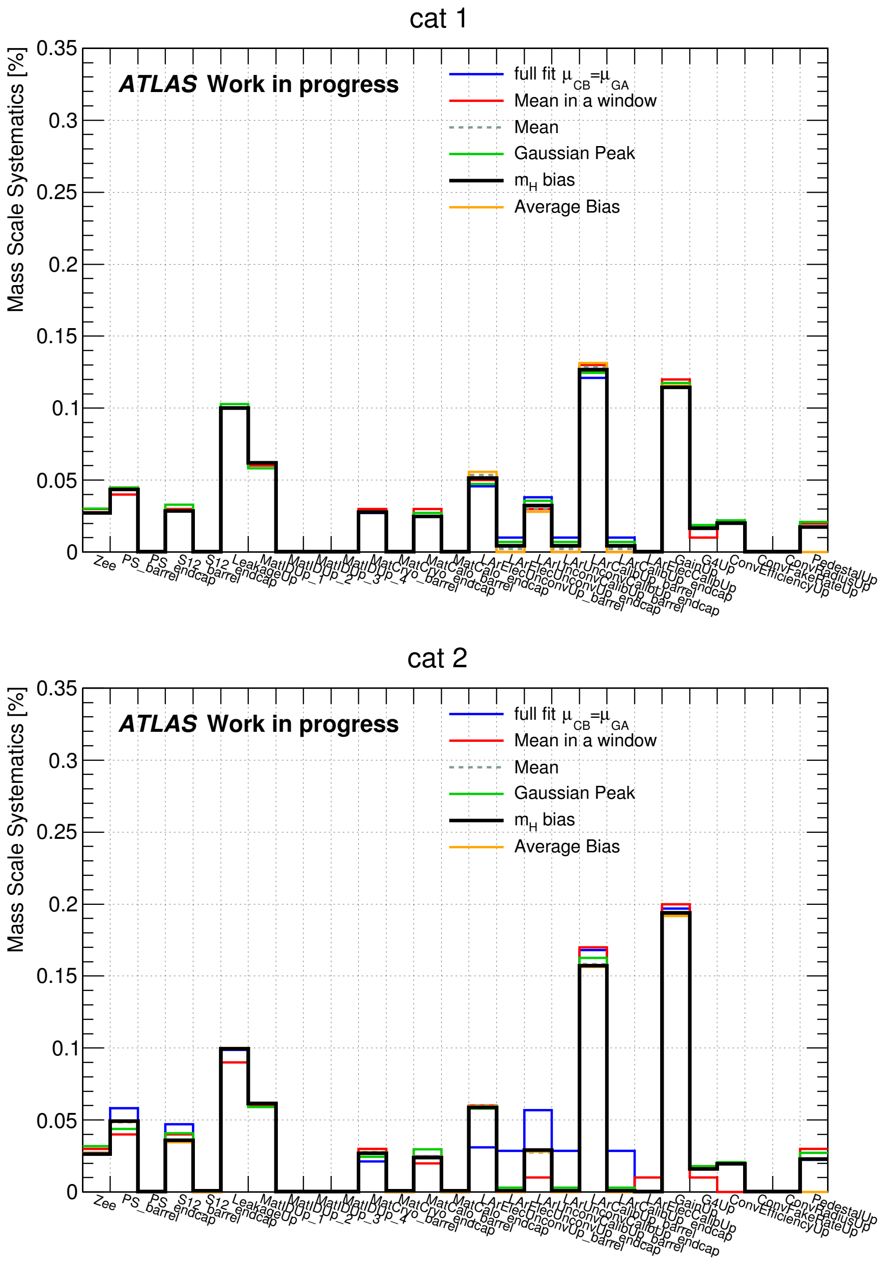


FIGURE 4.7: Mass Scale uncertainties for category 1-2

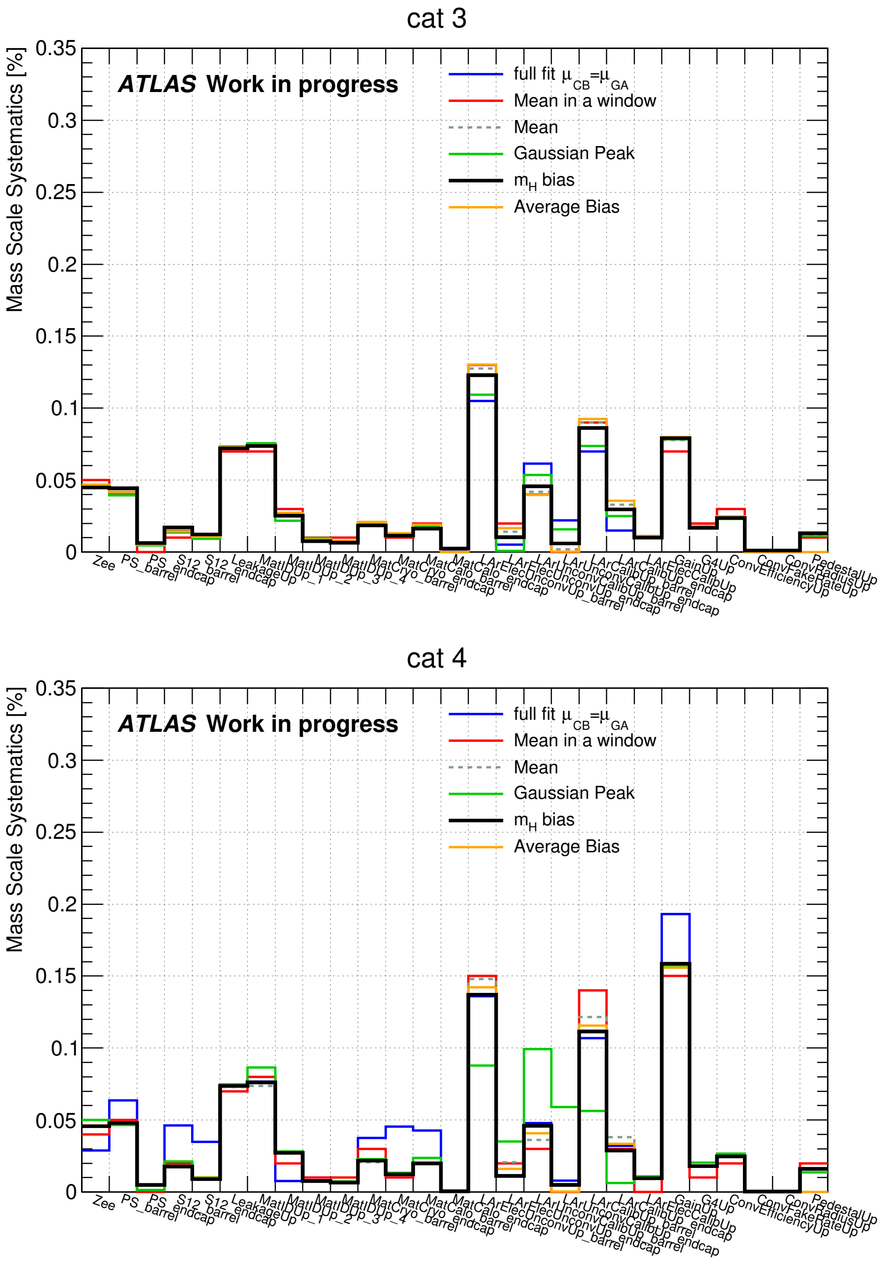


FIGURE 4.8: Mass Scale uncertainties for category 3-4

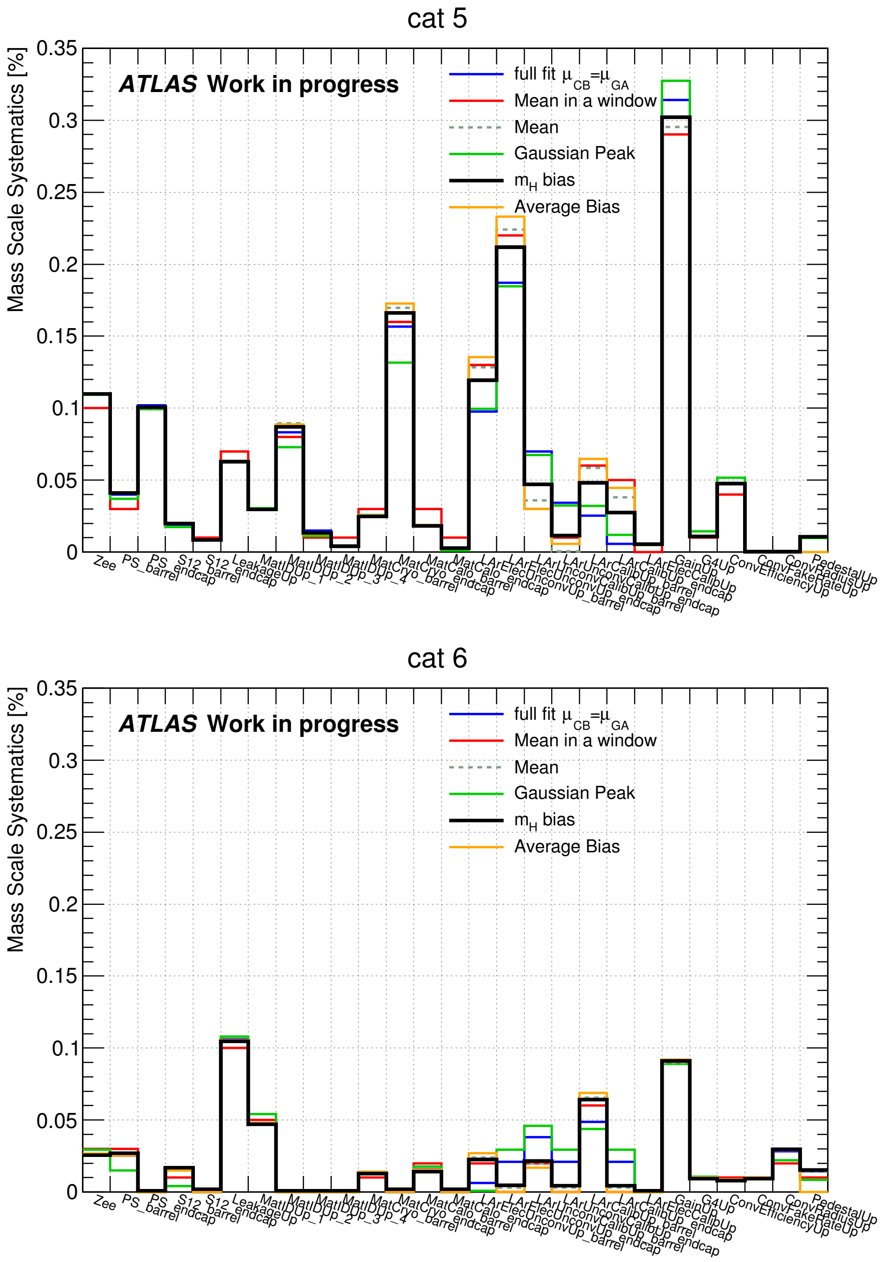


FIGURE 4.9: Mass Scale uncertainties for category 5-6

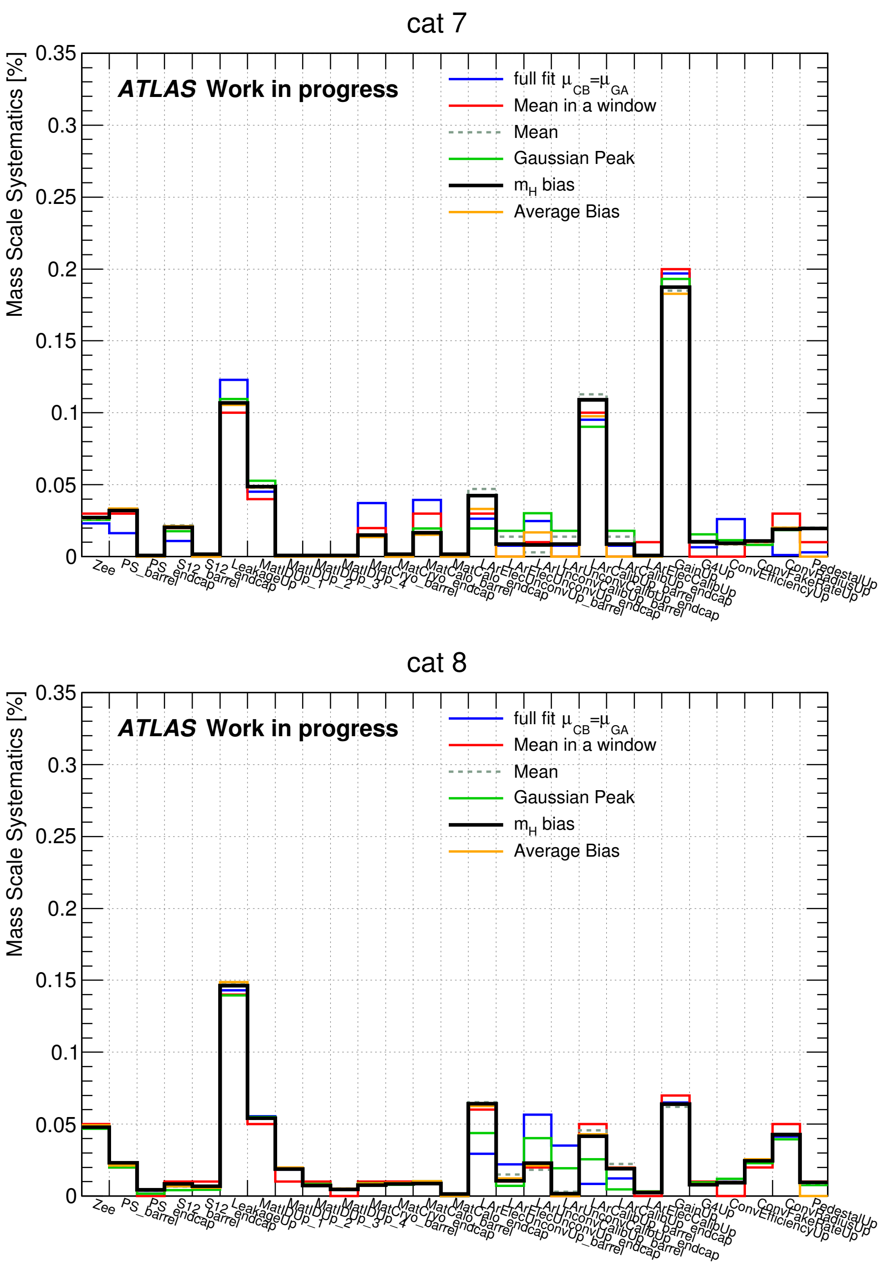


FIGURE 4.10: Mass Scale uncertainties for category 7-8

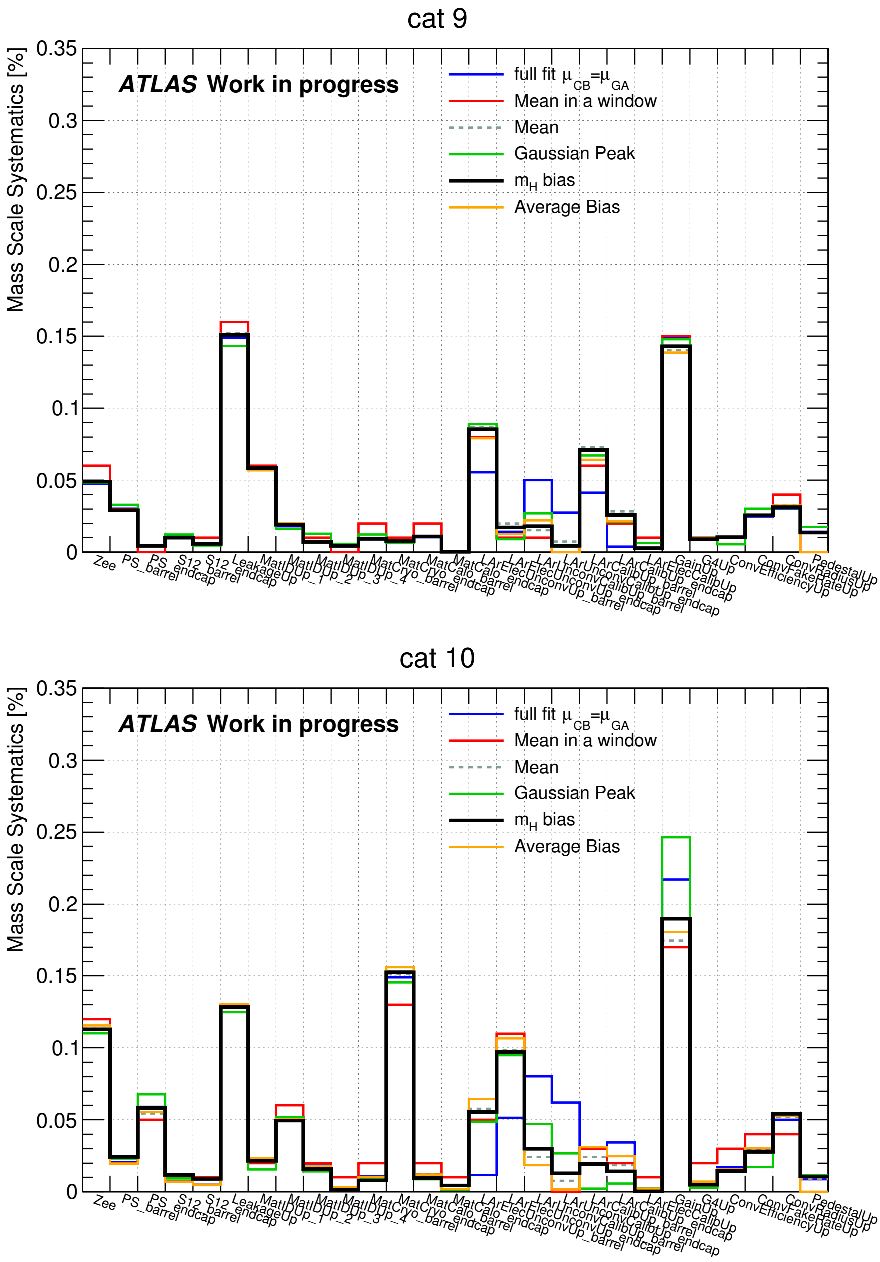


FIGURE 4.11: Mass Scale uncertainties for category 9-10

- $m_H$ Bias

| Systematics | C1 | C2 | C3 | C4 | C5 | C6 | C7 | C8 | C9 | C10 |
|---|---|---|---|---|---|---|---|---|---|---|
| Zee | 0.027 | 0.027 | 0.045 | 0.046 | 0.110 | 0.026 | 0.027 | 0.048 | 0.049 | 0.113 |
| PS barrel | 0.043 | 0.049 | 0.044 | 0.048 | 0.041 | 0.027 | 0.032 | 0.023 | 0.029 | 0.024 |
| PS endcap | - | - | 0.006 | 0.005 | 0.101 | 0.001 | 0.001 | 0.004 | 0.004 | 0.058 |
| S12 barrel | 0.029 | 0.036 | 0.017 | 0.018 | 0.020 | 0.017 | 0.021 | 0.008 | 0.010 | 0.012 |
| S12 endcap | - | 0.001 | 0.012 | 0.009 | 0.009 | 0.002 | 0.002 | 0.007 | 0.006 | 0.009 |
| LeakageUp | 0.100 | 0.100 | 0.072 | 0.074 | 0.063 | 0.105 | 0.107 | 0.146 | 0.151 | 0.128 |
| MatIDUp 1 | 0.062 | 0.061 | 0.074 | 0.076 | 0.030 | 0.047 | 0.049 | 0.054 | 0.059 | 0.021 |
| MatIDUp 2 | - | - | 0.025 | 0.027 | 0.087 | 0.001 | 0.001 | 0.019 | 0.019 | 0.049 |
| MatIDUp 3 | - | - | 0.008 | 0.008 | 0.013 | 0.001 | 0.001 | 0.007 | 0.007 | 0.016 |
| MatIDUp 4 | - | - | 0.007 | 0.006 | 0.004 | 0.001 | 0.001 | 0.005 | 0.005 | 0.001 |
| MatCryo barrel | 0.028 | 0.027 | 0.018 | 0.022 | 0.025 | 0.013 | 0.015 | 0.008 | 0.009 | 0.008 |
| MatCryo endcap | - | 0.001 | 0.011 | 0.012 | 0.166 | 0.002 | 0.002 | 0.008 | 0.008 | 0.153 |
| MatCalo barrel | 0.025 | 0.024 | 0.016 | 0.020 | 0.018 | 0.014 | 0.017 | 0.009 | 0.011 | 0.009 |
| MatCalo endcap | - | 0.001 | 0.002 | - | 0.003 | 0.002 | 0.002 | 0.001 | - | 0.004 |
| LArElecUnconvUp barrel | 0.051 | 0.059 | 0.123 | 0.137 | 0.119 | 0.022 | 0.042 | 0.064 | 0.085 | 0.056 |
| LArElecUnconvUp endcap | 0.004 | 0.001 | 0.010 | 0.011 | 0.212 | 0.005 | 0.009 | 0.011 | 0.017 | 0.097 |
| LArUnconvCalibUp barrel | 0.032 | 0.029 | 0.046 | 0.046 | 0.047 | 0.021 | 0.008 | 0.023 | 0.018 | 0.030 |
| LArUnconvCalibUp endcap | 0.004 | 0.001 | 0.006 | 0.005 | 0.011 | 0.005 | 0.009 | 0.002 | 0.004 | 0.013 |
| LArCalibUp barrel | 0.127 | 0.157 | 0.086 | 0.112 | 0.048 | 0.064 | 0.109 | 0.042 | 0.071 | 0.019 |
| LArCalibUp endcap | 0.004 | 0.001 | 0.030 | 0.029 | 0.028 | 0.004 | 0.009 | 0.019 | 0.026 | 0.014 |
| LArElecCalibUp | - | - | 0.010 | 0.010 | 0.005 | 0.001 | 0.001 | 0.002 | 0.003 | - |
| GainUp | 0.115 | 0.194 | 0.079 | 0.158 | 0.302 | 0.091 | 0.187 | 0.064 | 0.143 | 0.190 |
| G4Up | 0.017 | 0.016 | 0.017 | 0.018 | 0.011 | 0.009 | 0.010 | 0.008 | 0.009 | 0.005 |
| ConvEfficiencyUp | 0.020 | 0.019 | 0.024 | 0.025 | 0.048 | 0.008 | 0.009 | 0.009 | 0.010 | 0.014 |
| ConvFakeRateUp | - | - | 0.001 | - | - | 0.009 | 0.011 | 0.024 | 0.026 | 0.028 |
| ConvRadiusUp | - | - | 0.001 | - | - | 0.030 | 0.019 | 0.043 | 0.031 | 0.054 |
| PedestalUp | 0.017 | 0.023 | 0.013 | 0.016 | 0.011 | 0.015 | 0.019 | 0.010 | 0.014 | 0.011 |
| Total | 0.229 | 0.295 | 0.223 | 0.280 | 0.473 | 0.173 | 0.258 | 0.204 | 0.258 | 0.338 |

- Average bias

| Systematics | C1 | C2 | C3 | C4 | C5 | C6 | C7 | C8 | C9 | C10 |
|---|---|---|---|---|---|---|---|---|---|---|
| Zee | 0.027 | 0.027 | 0.047 | 0.046 | 0.110 | 0.027 | 0.027 | 0.049 | 0.049 | 0.116 |
| PS barrel | 0.044 | 0.049 | 0.042 | 0.048 | 0.041 | 0.025 | 0.033 | 0.021 | 0.029 | 0.020 |
| PS endcap | - | - | 0.005 | 0.005 | 0.101 | - | - | 0.004 | 0.004 | 0.055 |
| S12 barrel | 0.029 | 0.035 | 0.014 | 0.018 | 0.020 | 0.015 | 0.021 | 0.007 | 0.010 | 0.007 |
| S12 endcap | - | - | 0.011 | 0.010 | 0.008 | - | - | 0.006 | 0.006 | 0.005 |
| LeakageUp | 0.100 | 0.100 | 0.073 | 0.074 | 0.063 | 0.106 | 0.106 | 0.149 | 0.151 | 0.131 |
| MatIDUp 1 | 0.062 | 0.062 | 0.074 | 0.076 | 0.030 | 0.048 | 0.048 | 0.054 | 0.057 | 0.023 |
| MatIDUp 2 | - | - | 0.027 | 0.028 | 0.089 | - | - | 0.020 | 0.020 | 0.050 |
| MatIDUp 3 | - | - | 0.009 | 0.008 | 0.013 | - | - | 0.008 | 0.007 | 0.018 |
| MatIDUp 4 | - | - | 0.008 | 0.006 | 0.004 | - | - | 0.005 | 0.004 | 0.003 |
| MatCryo barrel | 0.027 | 0.028 | 0.021 | 0.022 | 0.026 | 0.014 | 0.014 | 0.009 | 0.009 | 0.010 |
| MatCryo endcap | - | - | 0.013 | 0.012 | 0.173 | - | - | 0.009 | 0.008 | 0.156 |
| MatCalo barrel | 0.024 | 0.024 | 0.019 | 0.020 | 0.019 | 0.015 | 0.015 | 0.010 | 0.011 | 0.012 |
| MatCalo endcap | - | - | - | - | 0.003 | - | - | - | - | 0.002 |
| LArElecUnconvUp barrel | 0.056 | 0.060 | 0.130 | 0.142 | 0.135 | 0.027 | 0.033 | 0.063 | 0.079 | 0.064 |
| LArElecUnconvUp endcap | - | - | 0.017 | 0.016 | 0.233 | - | - | 0.012 | 0.013 | 0.107 |
| LArUnconvCalibUp barrel | 0.028 | 0.028 | 0.040 | 0.041 | 0.030 | 0.017 | 0.017 | 0.021 | 0.022 | 0.018 |
| LArUnconvCalibUp endcap | - | - | - | - | 0.006 | - | - | - | - | 0.002 |
| LArCalibUp barrel | 0.131 | 0.156 | 0.093 | 0.115 | 0.065 | 0.069 | 0.098 | 0.043 | 0.064 | 0.031 |
| LArCalibUp endcap | - | - | 0.036 | 0.034 | 0.045 | - | - | 0.020 | 0.022 | 0.025 |
| LArElecCalibUp | - | - | 0.011 | 0.010 | 0.006 | - | - | 0.003 | 0.003 | 0.002 |
| GainUp | 0.116 | 0.192 | 0.080 | 0.156 | 0.302 | 0.092 | 0.183 | 0.064 | 0.139 | 0.180 |
| G4Up | 0.017 | 0.017 | 0.018 | 0.018 | 0.011 | 0.010 | 0.010 | 0.009 | 0.009 | 0.007 |
| ConvEfficiencyUp | 0.020 | 0.020 | 0.025 | 0.025 | 0.048 | 0.009 | 0.009 | 0.010 | 0.010 | 0.016 |
| ConvFakeRateUp | - | - | - | - | - | 0.010 | 0.010 | 0.026 | 0.026 | 0.030 |
| ConvRadiusUp | - | - | - | - | - | 0.029 | 0.020 | 0.043 | 0.032 | 0.053 |
| PedestalUp | 0.018 | 0.022 | 0.012 | 0.016 | 0.010 | 0.014 | 0.020 | 0.009 | 0.013 | 0.009 |
| Total | 0.233 | 0.294 | 0.231 | 0.283 | 0.492 | 0.176 | 0.248 | 0.206 | 0.251 | 0.341 |

- Full Model

| Systematics | C1 | C2 | C3 | C4 | C5 | C6 | C7 | C8 | C9 | C10 |
|---|---|---|---|---|---|---|---|---|---|---|
| Zee | 0.027 | 0.027 | 0.045 | 0.029 | 0.110 | 0.027 | 0.023 | 0.048 | 0.048 | 0.113 |
| PS barrel | 0.044 | 0.058 | 0.042 | 0.064 | 0.040 | 0.025 | 0.016 | 0.022 | 0.030 | 0.021 |
| PS endcap | - | - | 0.005 | 0.005 | 0.102 | - | - | 0.004 | 0.005 | 0.059 |
| S12 barrel | 0.029 | 0.047 | 0.015 | 0.046 | 0.019 | 0.015 | 0.011 | 0.007 | 0.011 | 0.007 |
| S12 endcap | - | - | 0.010 | 0.035 | 0.008 | - | - | 0.006 | 0.006 | 0.005 |
| LeakageUp | 0.100 | 0.099 | 0.073 | 0.074 | 0.063 | 0.106 | 0.123 | 0.143 | 0.149 | 0.129 |
| MatIDUp 1 | 0.062 | 0.062 | 0.075 | 0.077 | 0.030 | 0.048 | 0.045 | 0.055 | 0.059 | 0.023 |
| MatIDUp 2 | - | - | 0.025 | 0.008 | 0.083 | - | - | 0.018 | 0.018 | 0.052 |
| MatIDUp 3 | - | - | 0.009 | 0.008 | 0.015 | - | - | 0.008 | 0.007 | 0.018 |
| MatIDUp 4 | - | - | 0.007 | 0.006 | 0.004 | - | - | 0.005 | 0.004 | 0.003 |
| MatCryo barrel | 0.027 | 0.021 | 0.021 | 0.037 | 0.025 | 0.014 | 0.037 | 0.009 | 0.009 | 0.011 |
| MatCryo endcap | - | - | 0.013 | 0.045 | 0.157 | - | - | 0.009 | 0.008 | 0.149 |
| MatCalo barrel | 0.024 | 0.025 | 0.019 | 0.043 | 0.018 | 0.016 | 0.039 | 0.010 | 0.010 | 0.012 |
| MatCalo endcap | - | - | - | - | 0.003 | - | - | - | - | 0.002 |
| LArElecUnconvUp barrel | 0.046 | 0.031 | 0.105 | 0.136 | 0.098 | 0.006 | 0.026 | 0.029 | 0.055 | 0.012 |
| LArElecUnconvUp endcap | 0.010 | 0.029 | 0.005 | 0.011 | 0.187 | 0.021 | 0.008 | 0.022 | 0.014 | 0.051 |
| LArUnconvCalibUp barrel | 0.038 | 0.057 | 0.062 | 0.048 | 0.070 | 0.038 | 0.025 | 0.057 | 0.050 | 0.080 |
| LArUnconvCalibUp endcap | 0.010 | 0.029 | 0.022 | 0.008 | 0.034 | 0.021 | 0.008 | 0.035 | 0.028 | 0.062 |
| LArCalibUp barrel | 0.121 | 0.168 | 0.070 | 0.107 | 0.025 | 0.049 | 0.095 | 0.008 | 0.041 | 0.030 |
| LArCalibUp endcap | 0.010 | 0.029 | 0.015 | 0.032 | 0.006 | 0.021 | 0.008 | 0.012 | 0.004 | 0.034 |
| LArElecCalibUp | - | - | 0.011 | 0.010 | 0.006 | - | - | 0.003 | 0.003 | 0.002 |
| GainUp | 0.115 | 0.197 | 0.079 | 0.193 | 0.314 | 0.091 | 0.197 | 0.065 | 0.149 | 0.217 |
| G4Up | 0.017 | 0.017 | 0.018 | 0.018 | 0.011 | 0.010 | 0.007 | 0.009 | 0.009 | 0.007 |
| ConvEfficiencyUp | 0.020 | 0.020 | 0.025 | 0.025 | 0.048 | 0.009 | 0.026 | 0.010 | 0.010 | 0.017 |
| ConvFakeRateUp | - | - | - | - | - | 0.010 | 0.011 | 0.024 | 0.025 | 0.029 |
| ConvRadiusUp | - | - | - | - | - | 0.028 | 0.001 | 0.041 | 0.030 | 0.050 |
| PedestalUp | 0.018 | 0.022 | 0.012 | 0.016 | 0.010 | 0.014 | 0.003 | 0.009 | 0.014 | 0.009 |
| Total | 0.226 | 0.310 | 0.212 | 0.312 | 0.463 | 0.174 | 0.267 | 0.200 | 0.249 | 0.354 |

- Mean in a window

| Systematics | C1 | C2 | C3 | C4 | C5 | C6 | C7 | C8 | C9 | C10 |
|---|---|---|---|---|---|---|---|---|---|---|
| Zee | 0.030 | 0.030 | 0.050 | 0.040 | 0.100 | 0.030 | 0.030 | 0.050 | 0.060 | 0.120 |
| PS barrel | 0.040 | 0.040 | 0.040 | 0.050 | 0.030 | 0.030 | 0.030 | 0.020 | 0.030 | 0.020 |
| PS endcap | - | - | - | - | 0.100 | - | - | - | - | 0.050 |
| S12 barrel | 0.030 | 0.040 | 0.010 | 0.020 | 0.020 | 0.010 | 0.020 | 0.010 | 0.010 | 0.010 |
| S12 endcap | - | - | 0.010 | 0.010 | 0.010 | - | - | 0.010 | 0.010 | 0.010 |
| LeakageUp | 0.100 | 0.090 | 0.070 | 0.070 | 0.070 | 0.100 | 0.100 | 0.140 | 0.160 | 0.130 |
| MatIDUp 1 | 0.060 | 0.060 | 0.070 | 0.080 | 0.030 | 0.050 | 0.040 | 0.050 | 0.060 | 0.020 |
| MatIDUp 2 | - | - | 0.030 | 0.020 | 0.080 | - | - | 0.010 | 0.020 | 0.060 |
| MatIDUp 3 | - | - | 0.010 | 0.010 | 0.010 | - | - | 0.010 | 0.010 | 0.020 |
| MatIDUp 4 | - | - | 0.010 | 0.010 | 0.010 | - | - | - | - | 0.010 |
| MatCryo barrel | 0.030 | 0.030 | 0.020 | 0.030 | 0.030 | 0.010 | 0.020 | 0.010 | 0.020 | 0.020 |
| MatCryo endcap | - | - | 0.010 | 0.010 | 0.160 | - | - | 0.010 | 0.010 | 0.130 |
| MatCalo barrel | 0.030 | 0.020 | 0.020 | 0.020 | 0.030 | 0.020 | 0.030 | 0.010 | 0.020 | 0.020 |
| MatCalo endcap | - | - | - | - | 0.010 | - | - | - | - | 0.010 |
| LArElecUnconvUp barrel | 0.050 | 0.060 | 0.130 | 0.150 | 0.130 | 0.020 | 0.030 | 0.060 | 0.080 | 0.050 |
| LArElecUnconvUp endcap | - | - | 0.020 | 0.020 | 0.220 | - | - | 0.010 | 0.010 | 0.110 |
| LArUnconvCalibUp barrel | 0.030 | 0.010 | 0.040 | 0.030 | 0.030 | 0.020 | 0.010 | 0.020 | 0.010 | 0.030 |
| LArUnconvCalibUp endcap | - | - | - | - | 0.010 | - | - | - | - | - |
| LArCalibUp barrel | 0.130 | 0.170 | 0.090 | 0.140 | 0.060 | 0.060 | 0.100 | 0.050 | 0.060 | 0.030 |
| LArCalibUp endcap | - | - | 0.030 | 0.030 | 0.050 | - | - | 0.020 | 0.020 | 0.020 |
| LArElecCalibUp | - | 0.010 | 0.010 | - | - | - | 0.010 | - | 0.010 | 0.010 |
| GainUp | 0.120 | 0.200 | 0.070 | 0.150 | 0.290 | 0.090 | 0.200 | 0.070 | 0.150 | 0.170 |
| G4Up | 0.010 | 0.010 | 0.020 | 0.010 | 0.010 | 0.010 | - | 0.010 | 0.010 | 0.020 |
| ConvEfficiencyUp | 0.020 | - | 0.030 | 0.020 | 0.040 | 0.010 | - | - | 0.010 | 0.030 |
| ConvFakeRateUp | - | - | - | - | - | 0.010 | 0.010 | 0.020 | 0.030 | 0.040 |
| ConvRadiusUp | - | - | - | - | - | 0.020 | 0.030 | 0.050 | 0.040 | 0.040 |
| PedestalUp | 0.020 | 0.030 | 0.010 | 0.020 | 0.010 | 0.010 | 0.010 | 0.010 | - | 0.010 |
| Total | 0.233 | 0.301 | 0.224 | 0.293 | 0.469 | 0.168 | 0.259 | 0.202 | 0.267 | 0.327 |

- Gaussian Peak

| Systematics | C1 | C2 | C3 | C4 | C5 | C6 | C7 | C8 | C9 | C10 |
|---|---|---|---|---|---|---|---|---|---|---|
| Zee | 0.030 | 0.032 | 0.046 | 0.050 | 0.109 | 0.029 | 0.026 | 0.047 | 0.048 | 0.110 |
| PS barrel | 0.045 | 0.044 | 0.039 | 0.047 | 0.037 | 0.015 | 0.032 | 0.020 | 0.033 | 0.023 |
| PS endcap | - | - | 0.005 | 0.001 | 0.099 | - | - | 0.002 | 0.004 | 0.068 |
| S12 barrel | 0.033 | 0.041 | 0.014 | 0.021 | 0.018 | 0.004 | 0.018 | 0.004 | 0.012 | 0.009 |
| S12 endcap | - | - | 0.009 | 0.010 | 0.009 | - | - | 0.004 | 0.005 | 0.005 |
| LeakageUp | 0.103 | 0.099 | 0.073 | 0.075 | 0.062 | 0.108 | 0.110 | 0.139 | 0.143 | 0.125 |
| MatIDUp 1 | 0.058 | 0.059 | 0.076 | 0.087 | 0.030 | 0.054 | 0.053 | 0.055 | 0.059 | 0.015 |
| MatIDUp 2 | - | - | 0.022 | 0.028 | 0.073 | - | - | 0.019 | 0.016 | 0.052 |
| MatIDUp 3 | - | - | 0.010 | 0.008 | 0.011 | - | - | 0.008 | 0.013 | 0.014 |
| MatIDUp 4 | - | - | 0.006 | 0.007 | 0.004 | - | - | 0.005 | 0.006 | 0.003 |
| MatCryo barrel | 0.028 | 0.024 | 0.020 | 0.023 | 0.026 | 0.014 | 0.015 | 0.009 | 0.012 | 0.009 |
| MatCryo endcap | - | - | 0.011 | 0.013 | 0.132 | - | - | 0.008 | 0.006 | 0.145 |
| MatCalo barrel | 0.027 | 0.030 | 0.018 | 0.024 | 0.018 | 0.018 | 0.020 | 0.010 | 0.011 | 0.009 |
| MatCalo endcap | - | - | - | - | 0.001 | - | - | - | - | 0.001 |
| LArElecUnconvUp barrel | 0.047 | 0.058 | 0.109 | 0.088 | 0.100 | 0.001 | 0.020 | 0.044 | 0.089 | 0.049 |
| LArElecUnconvUp endcap | 0.007 | 0.003 | 0.001 | 0.035 | 0.185 | 0.029 | 0.018 | 0.007 | 0.009 | 0.095 |
| LArUnconvCalibUp barrel | 0.036 | 0.028 | 0.054 | 0.099 | 0.068 | 0.046 | 0.030 | 0.040 | 0.027 | 0.047 |
| LArUnconvCalibUp endcap | 0.007 | 0.003 | 0.016 | 0.059 | 0.032 | 0.029 | 0.018 | 0.019 | 0.005 | 0.027 |
| LArCalibUp barrel | 0.124 | 0.163 | 0.074 | 0.056 | 0.032 | 0.044 | 0.090 | 0.026 | 0.067 | 0.002 |
| LArCalibUp endcap | 0.007 | 0.003 | 0.025 | 0.006 | 0.012 | 0.029 | 0.018 | 0.005 | 0.021 | 0.006 |
| LArElecCalibUp | - | - | 0.011 | 0.011 | 0.005 | - | - | 0.003 | 0.006 | 0.002 |
| GainUp | 0.117 | 0.192 | 0.078 | 0.157 | 0.327 | 0.089 | 0.193 | 0.064 | 0.148 | 0.246 |
| G4Up | 0.019 | 0.018 | 0.017 | 0.020 | 0.015 | 0.011 | 0.016 | 0.010 | 0.010 | 0.003 |
| ConvEfficiencyUp | 0.022 | 0.021 | 0.023 | 0.027 | 0.052 | 0.009 | 0.011 | 0.012 | 0.005 | 0.015 |
| ConvFakeRateUp | - | - | - | - | - | 0.010 | 0.008 | 0.023 | 0.030 | 0.017 |
| ConvRadiusUp | - | - | - | - | - | 0.022 | 0.019 | 0.039 | 0.030 | 0.055 |
| PedestalUp | 0.021 | 0.027 | 0.012 | 0.014 | 0.010 | 0.009 | 0.020 | 0.008 | 0.018 | 0.012 |
| Total | 0.232 | 0.297 | 0.212 | 0.269 | 0.462 | 0.178 | 0.258 | 0.192 | 0.257 | 0.369 |

## 4.8 Other uncertainties due to Energy Scale

### 4.8.1 Signal Yields

The uncertainties of the photon energy scale gives an uncertainty on the $p_T$ scale used to select the photons, through the relative $pT$ cut. For each of the category the selection efficiency is evaluated varying the energy scale within the uncertainty.

The variation in efficiency can be written as:

$$\alpha = \frac{N_{A'} + N_{B'}}{N_A + N_B} - 1 \tag{4.11}$$

with $N_A$ and $N_B$ being the number of selected events respectively in a category with $p_{Tt} > 70\,GeV$ $p_{Tt} < 70\,GeV$ and $N_{A'}$ and $N_{B'}$ being the number of selected events in the same categories, when applied the energy scale. The inclusive impact in the systematics from the energy scale on the total yields was found to be lower than 0.035% and therefore neglected.

### 4.8.2 Migration

The uncertainty on the energy scale leads to an uncertainty on the boundary between low and high $p_{Tt}$ category. The systematics on the migration of candidates between these two categories is evaluated as:

$$\delta_{mig} = \frac{\alpha'}{\alpha} - 1 \tag{4.12}$$

with

$$\alpha = \frac{N_A}{N_A + N_B} \text{ and } \alpha' = \frac{N_{A'}}{N_{A'} + N_{B'}} \tag{4.13}$$

with $N_A$,$N_B$,$N_{A'}$ and $N_{B'}$ defined as before. The $\delta_{mig}$ is computed for the different categories and found to be lower 0.05% and it's therefore neglected.

## 4.9 Theoretical Uncertainty

Theoretical uncertainties comes from three different contribution:

1. **Branching Ratio**: The BR of SM Higgs boson decaying into two photons has a theoretical uncertainties of $\sim 4.8\%$ for a mass around $126GeV$, and this uncertainty depends on the mass [19]

| | ggH | VBF | WH | ZH | $t\bar{t}H$ |
|---|---|---|---|---|---|
| BR | | | $^{4.8}_{4.7}$ | | |

2. **Scale**: The Higgs boson cross section from different process have an uncertainty coming from the variation of the renormalization and factorization scales.

| | ggH | VBF | WH | ZH | $t\bar{t}H$ |
|---|---|---|---|---|---|
| Scale | $^{+7.2}_{-7.8}$ | $\pm 0.2$ | $\pm 1.0$ | $\pm 3.2$ | $^{+3.8}_{-9.3}$ |

3. **PDF + $\alpha_s$**: The variation of the set of parton distribution functions chosen to compute the cross section leads to an uncertainty. The uncertainty is the largest for the ggH.

| | ggH | VBF | WH | ZH | $t\bar{t}H$ |
|---|---|---|---|---|---|
| $PDF + \alpha_s$ | $^{+7.5}_{-6.9}$ | $^{+2.6}_{-2.7}$ | $\pm 2.3$ | $\pm 2.5$ | $\pm 8.1$ |

## 4.10 Migration Uncertainties

This systematic impacts the repartition into the difference categories of the analysis and comes from uncertainties on the variable used to built the categories.

- **Higgs Boson $p_T$**: The non perfect knowledge of the Higgs $p_T$ spectrum shape can introduce migrations between high and low $p_{Tt}$ categories.
- **Material and Conversion**: The probability of photon conversion in the detector depends on the amount of material crossed by. Therefore this introduce an uncertainties on the number of converted photons with respect to the number of unconverted ones.

All the contributions of the migration uncertainties are summarizes in Table 4.3

| | C1 | C2 | C3 | C4 | C5 | C6 | C7 | C8 | C9 | C10 |
|---|---|---|---|---|---|---|---|---|---|---|
| Higgs $p_T$ | -0.9 | +11.3 | -0.9 | +11.3 | +0.2 | -0.9 | +11.3 | -0.9 | +11.3 | -0.4 |
| Material | -0.7 | -0.7 | -2.6 | -2.6 | -4.0 | +1.0 | +1.0 | +2.3 | +2.3 | +2.6 |
| Conv Inefficiency | -2.6 | -2.7 | -4.8 | -5.0 | -4.4 | 3.4 | 3.4 | 3.8 | 3.6 | 4.9 |
| Conv FakeRate | -1.1 | -1.0 | -2.2 | -2.2 | -3.1 | +1.5 | +1.2 | +2.2 | 2.0 | 1.7 |

Table 4.3: Uncertainty on the yield from events migration between categories, in%

## 4.11 Resolution Uncertainty

The systematics uncertainties on the di-photons invariant mass related to the determination of the resolution are coming from four different sources:

- Constant term: (see Chapter 3) uncertainty on the extraction of the smearing from the $Z \to ee$ sample applied to MC.
- Intrinsic resolution: a 10% uncertainty in the intrinsic calorimeter resolution is taken as 10% relative.
- Material mis-modeling effect.
- Electronic and pileup noise modeling.

These four source of uncertainties are implemented in the analysis as four different parameters in different categories (See Table 4.4).

| Category | Constant Term[%] | Intrinsic resolution[%] | Material [%] | Electronic pileup[%] |
|---|---|---|---|---|
| Incl | ±9 | ±2 | ±6 | ±1 |
| Cat 1 | ±9 | ±3 | ±6 | ±1 |
| Cat 2 | ±11 | ±6 | ±7 | ±2 |
| Cat 3 | ±11 | ±2 | ±7 | ±1 |
| Cat 4 | ±12 | ±4 | ±8 | ±1 |
| Cat 5 | ±12 | ±2 | ±10 | ±1 |
| Cat 6 | ±7 | ±3 | ±4 | ±1 |
| Cat 7 | ±8 | ±6 | ±6 | ±1 |
| Cat 8 | ±8 | ±1 | ±4 | ±1 |
| Cat 9 | ±11 | ±3 | ±7 | ±2 |
| Cat 10 | ±8 | ±1 | ±6 | ±1 |

Table 4.4: Resolution Uncertainty

## 4.12 Statistical

Statistical methods are needed in order to estimate the properties of the signal, like Higgs Mass $m_H$, the cross section $\sigma$, the coupling to other particles or the signal strength $\mu$. In order to extract properties from data the more corrected procedure was found to built a **likelihood function**. The likelihood contains the POI (parameters of interest) ,i.e. the variables that are tested like the mass of the Higgs or the signal strength, and the *nuisance parameters* i.e. unknown parameters related to the systematics. The nuisance parameters are denoted with the vector $\vec{\theta}$.

The $H \to \gamma\gamma$ mass analysis is based on an extended unbinned likelihood function(considering only one category):

$$L(m_H, \vec{\theta}) =$$

$$Pois(N'|\mu N_s^{SM} + N_b) \cdot \prod_{k=1}^{N'} \left[ \frac{\mu \cdot N_s^{SM}}{\mu \cdot N_s^{SM} + N_b} \Psi_s(m_{\gamma\gamma}^{(k)}|m_H, \vec{\theta}) + \frac{N_b}{\mu \cdot N_s^{SM} + N_b} \Psi_b^k(m_{\gamma\gamma}^{(k)}|\vec{\theta}) \right] \cdot F(\vec{\theta}) \tag{4.14}$$

where $N'$ is the total number of events,the signal strength $\mu$ is the ratio between the numbers of signal events observed and the corresponding expected events in the SM

$$\mu = \frac{N_s}{N_s^{SM}} \tag{4.15}$$

$N_b$ the number of background events and $\Psi_s^k$, $\Psi_s^k$ are the probability density function of $m_{\gamma\gamma}$ respectively for the signal and the background. The parametrization of the signal pdf $\Psi_S$ is taken from the global fit described in Section 4.3. The parameters for the background are fit directly on data while the shape is chosen from background study. The only POI taken into account for this analysis is $m_H$. The likelihood is built taken into account the chosen categorization. Each category has its own likelihood $L_c(m_H, \vec{\theta_i})$ with the POI $m_H$ common to all the categories, whereas the nuisance parameters $\vec{\theta_i}$ can be different for each channel. If an uncertainty is common to all categories, a common nuisance parameter is used. The combine likelihood is built as product of all the individual likelihoods.

$$L(m_H, \vec{\theta}) = \prod_{c=1}^{N_c} L_c(m_H, \vec{\theta_c}) \tag{4.16}$$

where $\vec{\theta} = \cup\vec{\theta_c} = (\theta_1, \theta_2, ...)$ is the complete set of nuisance parameters, and $N_c$ is the total numbers of categories. The test statistic used for the $m_H$ estimation is the profile likelihood ratio defined as:

$$\lambda(m_H) = \frac{L(m_H, \hat{\hat{\theta}}(m_H))}{L(m_H, \hat{\theta})} \tag{4.17}$$

with $\hat{\hat{\theta}}$ are the nuisance parameters that maximize the likelihood for the mass hypothesis $m_H$, and the denominator corresponding to the unconditional maximum of the likelihood. It's more significant to evaluate the following expression

$$-2\ln[\lambda(m_H)] \tag{4.18}$$

at each tested mass point. The profile likelihood ratio is built testing the ratio at different $m_H$ mass. The minimum is extracted by an interpolation between this point.

### 4.12.1 Uncertainties in the likelihood

The systematics uncertainties are taken into account through the use of nuisance parameters in the likelihood. The uncertainties can affect the signal yields, the migration of events in different categories (Sec 4.10),the signal resolution (Sec. 4.11). For the systematic affecting the event yield, the systematic uncertainties are carried out by the parameter $K^c$ in the expression:

$$N_s^c = \mu N_s^{SM,c} = \mu[N^{ggH,c} + N^{VBF,c} + N^{WH,c} + N^{ZH,c} + N^{ttH,c}] \cdot K^c + n_{spurious} \cdot K_{spurious},$$

where $N_s^c$ is the number of signal observed in the category $c$.

$$K^c = K_{Lumi} \cdot K_{ID} \cdot K_{Iso} \cdot K_{ES} \cdot K_{BR} \cdot K^c_{\sigma^{theor}_{ggH}} \cdot K^c_{p_T} \cdot K^c_{Mat} \cdot K_{ConvEff} \cdot K_{ConvFake} \tag{4.19}$$

and

$$N^{X,c} = N^{X,SM}[K_{X\,,scale} \cdot K_{X\,,PDF}] \tag{4.20}$$

In these formulae:

- $n_{spurious}$ is the number of signal measured in background-only sample with a signal+background fit (see Section 4.6)
- $N^{X,SM}$ corresponds to the number of signal expected in the Standard Model for a Higgs boson production *via* the $X$ process, $X = ggH,\ VBF,\ WH,\ VH,\ ttH$
- the terms $K_{yy}$ correspond to the function that models the systematic uncertainty associated with the source $yy$.
- the terms $K^c_{yy}$ have the same definition than the $K_{yy}$ except that they depend on the category $c$.
- the terms $K_{X,yy}$ or $K^c_{X,yy}$ have the same definition than the $K_{yy}$ or $K^c_{yy}$ except that they depend on the production process $X$

### 4.12.2 Signal width and position

The signal shape is modeled with a composition of a Crystal Ball and a Gaussian functions as detailed in Section 4.3. Taking now the systematic uncertainties into account, Equation 4.3 can be rewritten as:

$$\begin{aligned} C =& f_{CB} \cdot F_{CB}(m_{\gamma\gamma}, \mu_{CB} \cdot K_\mu, \sigma_{CB} \cdot K_\sigma, \alpha_{CB}) + \\ &+ (1 - f_{CB}) \cdot F_{Ga}(m_{\gamma\gamma}, \mu_{Ga} \cdot K_\mu, \kappa_{Ga} \cdot \sigma_{CB} \cdot K_\sigma) \end{aligned} \tag{4.21}$$

where $K_\mu$ and $K_\sigma$ are functions that model the systematic uncertainties on the signal position and resolution and with $K_\mu$ defined as:

$$K_\mu = \prod_{i=1}^{N} K_i \tag{4.22}$$

with $N$ the total number of uncorrelated sources of uncertainties for the signal position determined in Section 4.7.

### 4.12.3 K modeling and the constraints

The functions $K$ defined above have different modeling, depending on the source of uncertainties they represent. Two main cases are:

$$\begin{aligned} K =& 1 + \delta\theta \\ K =& e^{\sqrt{\log(1+\delta^2)}\theta} \end{aligned} \tag{4.23}$$

where $\delta$ is the value of the uncertainty and $\theta$ is the nuisance parameter associated to the uncertainty. The systematic uncertainty as experimentally or theoretically determined $\delta$ is not used directly as an uncertainty in these models. Instead, the factor $\theta$ gives more or less weight to this uncertainty. This is the frequentist approach for treating the systematic uncertainties. The $\theta$ parameters are directly determined during the fit, so that they minimize the likelihood. Their value is not free to vary. The constraint can take different forms:

- Gaussian constraint $G$: $G(x) = \frac{1}{N} e^{(x-\delta)^2/2}$. The fit is allowed to find a value of $\theta$ inside a Gaussian function having for mean the value of the uncertainty itself $\delta$ and a width of unity. It is then less probable to find a value far from the mean.
- Flat constrain, generally a Double-Fermi-Dirac function is used. In this case, the probably to find a value far from the mean is almost as probable as finding a value close to the mean:

  $$DFD(x) = A - B \cdot \frac{1}{1 + e^{C \cdot x}} \cdot \frac{1}{1 + e^{D \cdot x}}$$

  with $A$ the averaged value on either sides of the hole, $B$ the hole depth and $C$ and $D$ the hole width.

For example for the uncertainty on the peak position, taking Equation 4.22:

$$K_\mu = \prod_{i=1}^{N} (1 + \theta_i \delta_i) \tag{4.24}$$

where $\theta_i$ are the 27 nuisances parameters constrained with a Gaussian form $G$ and where $\delta_i$ correspond to the 27 different systematics uncertainties values associated to the peak position. The same form is used for the uncertainty coming from the background model $K_{spurious}$.These forms are called Gaussian constraints. Another representative example concerns the uncertainty on the resolution:

$$K_\sigma = e^{\theta_{CT}\sqrt{ln(1+\delta^2_{CT})}} \cdot e^{\theta_{ST}\sqrt{ln(1+\delta^2_{ST})}} \cdot e^{\theta_{MAT}\sqrt{ln(1+\delta^2_{MAT})}} \cdot e^{\theta_{PU}\sqrt{ln(1+\delta^2_{PU})}},$$

with $\delta_i$ the uncertainty value on the mass resolution coming from the source $i$ and $\theta_i$ the nuisance parameter related to this uncertainty, constrained with a Gaussian function $G$ of width 1 in the likelihood. This form is called a lognormal constraint.

## 4.13 Results

Taking into account all the uncertainties and the parametrization of the signal and the background, the value of the Higgs mass is evaluated minimizing the Profile Likelihood Ratio.Figure shows the inclusive category. Figure 4.13 show the inclusive $m_{\gamma\gamma}$ distribution with the signal and background fit to data. Figures 4.14-4.18 shows the $m_{\gamma\gamma}$ distribution in different categories. The profile likelihood defined in Equation 4.18 is shown in Figure 4.12. The two curves with the smaller and the larger width give a measurement of the mass and respectively of the statistical and total uncertainties. The statistical error evaluation is perform setting the nuisance parameters to their value best. The systematic error is estimated from the difference in quadrature of the statistical and total error. The measured mass and its uncertainty is:

$$m_H = 126.30 \pm 0.37 \text{ (stat)} \pm 0.29 \text{ (syst) GeV} \tag{4.25}$$

where the systematic error is obtained by quadratically subtraction the statistical uncertainty from the total uncertainty. In a similar way the signal strength is also tested:

$$\mu = 1.33^{+0.27}_{-0.27} \text{ (stat)}^{+0.19}_{-0.14} \text{ (syst)} \tag{4.26}$$

In Figure 4.19 the pull of the nuisance parameters is shown. No particular pull is present during the fit process.

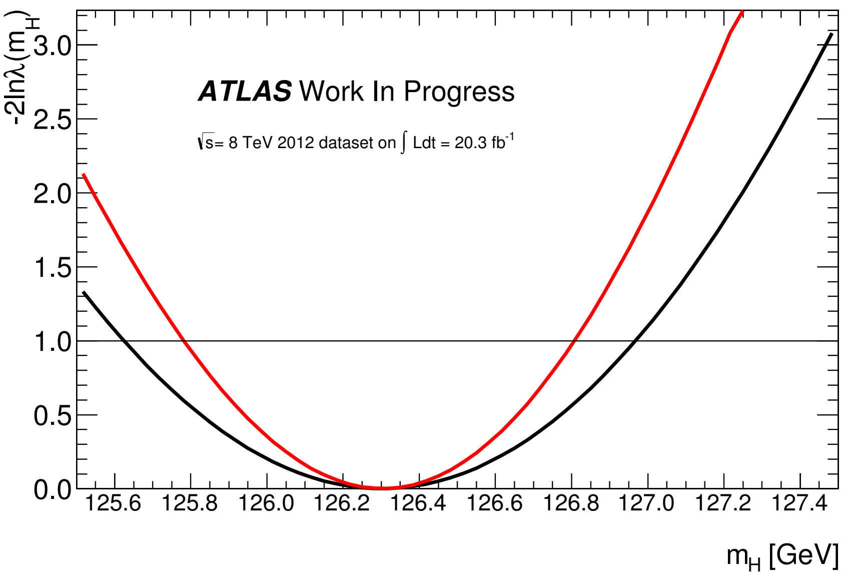


FIGURE 4.12: Profile Likelihood Ratio

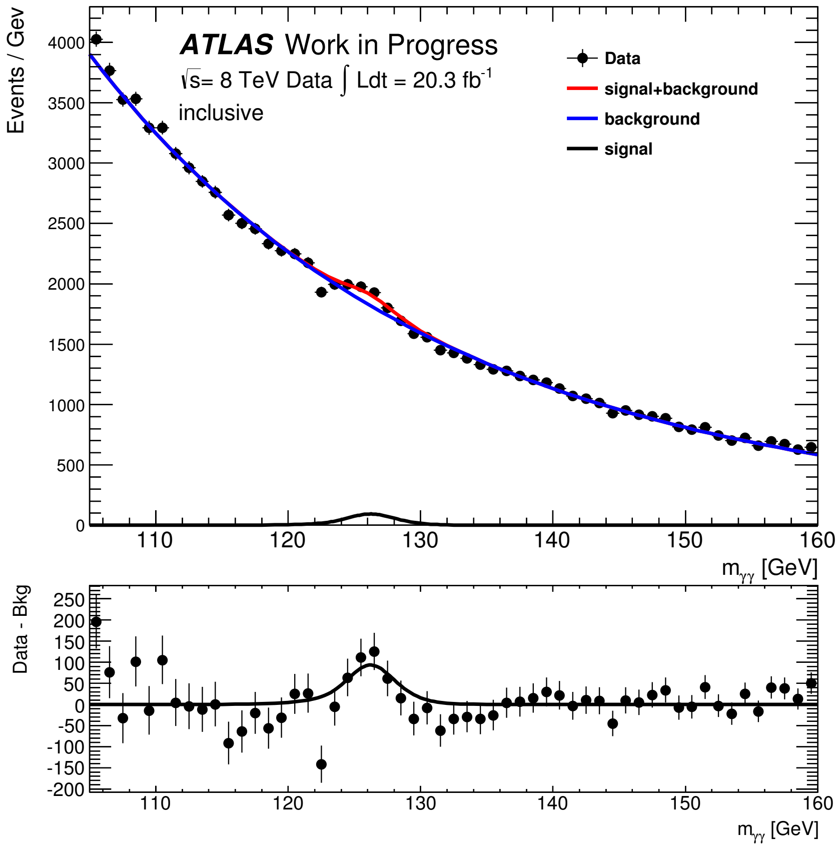


FIGURE 4.13: Inclusive category.

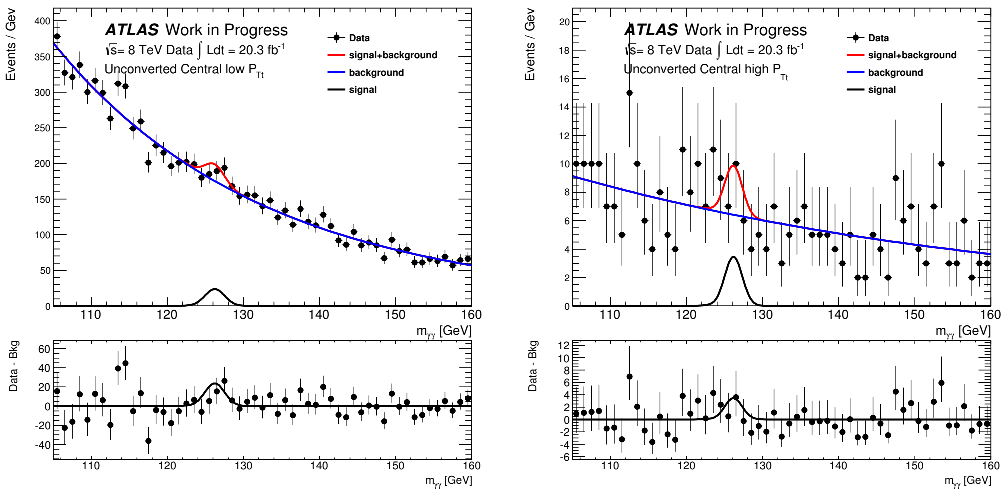


FIGURE 4.14: Unconverted Good low/high $p_{Tt}$

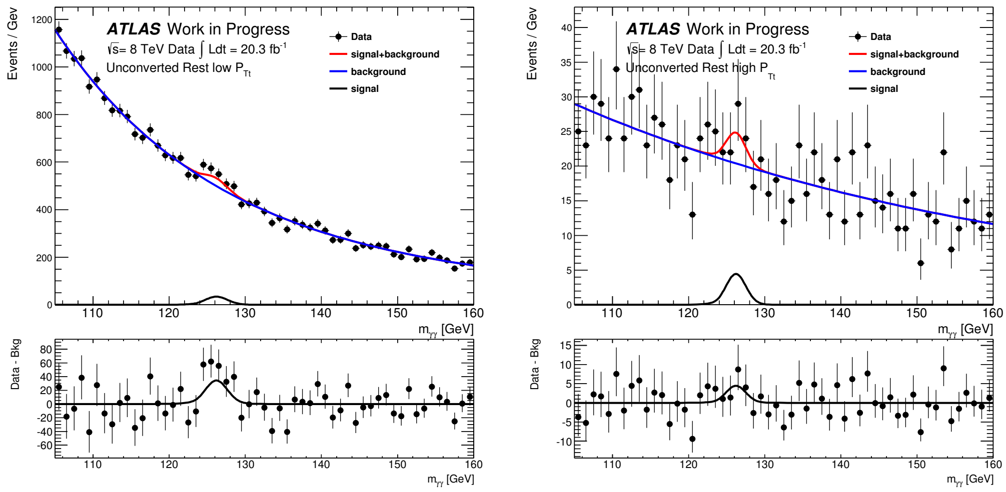


FIGURE 4.15: Unconverted Rest low/high $p_{Tt}$

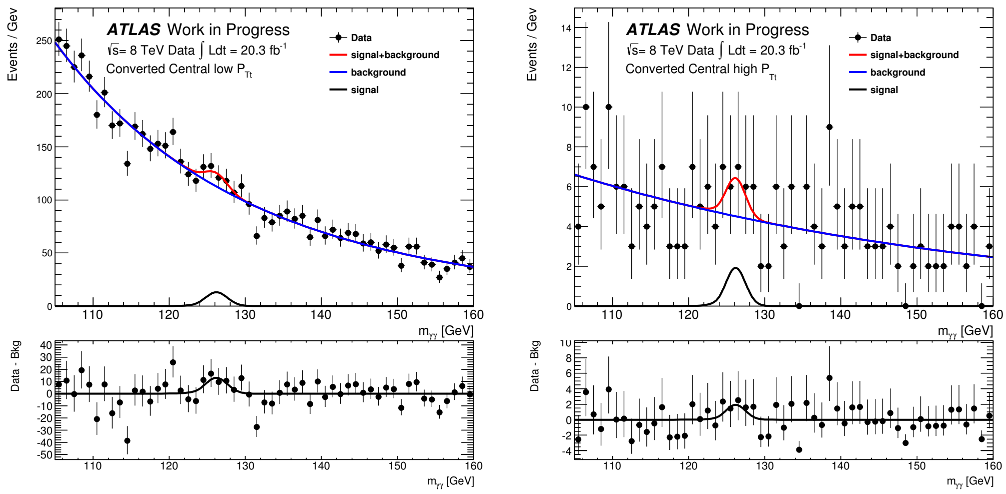


FIGURE 4.16: At least one converted Good low/high $p_{Tt}$

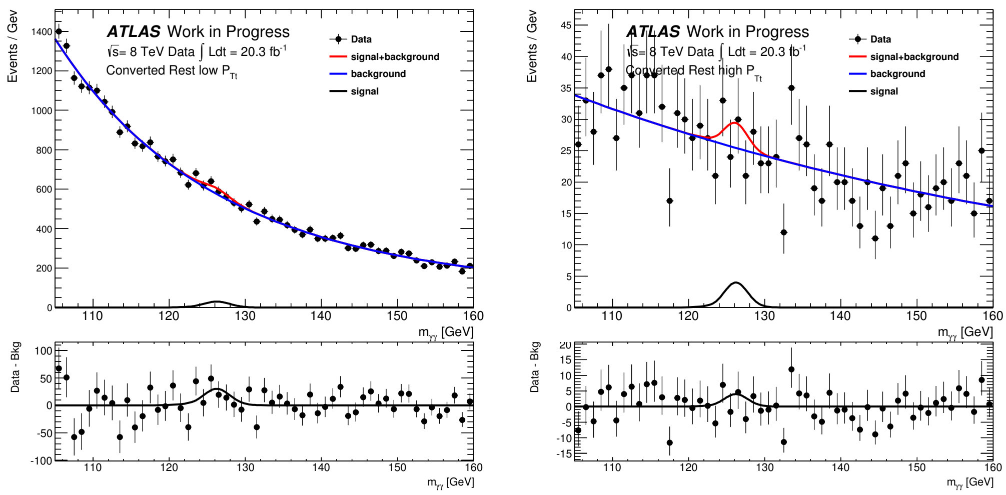


FIGURE 4.17: At least one converted Rest low/high $p_{Tt}$

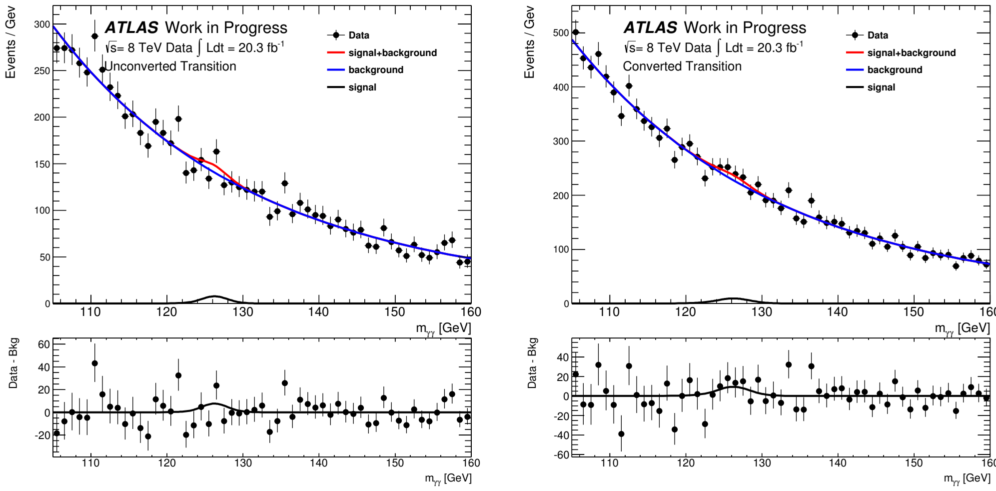


FIGURE 4.18: Transition Unconverted/Converted

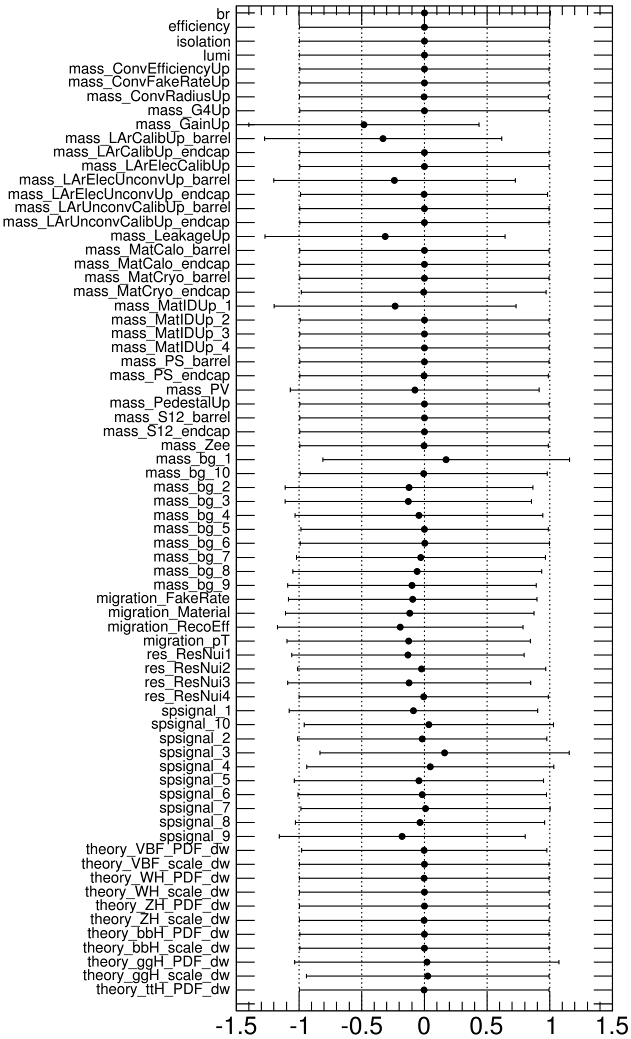


FIGURE 4.19: Pull of nuisance parameters

# Conclusion

A new mass measurement of the Higgs boson decay into di-photon has been performed using the 20.3 $\text{fb}^{-1}$ of proton-proton collision at the $\sqrt{8}$ TeV with the ATLAS detector at the LHC. The systematics uncertainties has been reduced by a factor 2 thanks to an important effort in the refinement and revaluation of the systematics. The measured mass is:

$$m_H = 126.30 \pm 0.37 \text{ (stat)} \pm 0.29 \text{ (syst) GeV}$$

# Bibliography


[1] Sheldon L. Glashow. Partial-symmetries of weak interactions. *Nuclear Physics*, 22(4):579 – 588, 1961.

[2] Steven Weinberg. A model of leptons. *Phys. Rev. Lett.*, 19:1264–1266, Nov 1967.

[3] G. 't Hooft and M. Veltman. Regularization and renormalization of gauge fields. *Nuclear Physics B*, 44:189–213, July 1972.

[4] P. W. Higgs. Broken symmetries, massless particles and gauge fields. *Physics Letters*, 12:132–133, September 1964.

[5] F. Englert and R. Brout. Broken symmetry and the mass of gauge vector mesons. *Phys. Rev. Lett.*, 13:321–323, Aug 1964.

[6] G. S. Guralnik, C. R. Hagen, and T. W. B. Kibble. Global conservation laws and massless particles. *Phys. Rev. Lett.*, 13:585–587, Nov 1964.

[7] Observation of a new particle in the search for the standard model higgs boson with the atlas detector at the lhc. *Physics Letters B*, 716(1):1 – 29, 2012.

[8] Serguei Chatrchyan et al. Observation of a new boson at a mass of 125 GeV with the CMS experiment at the LHC. *Phys.Lett.*, B716:30–61, 2012.

[9] The nobel prize in physics 2013.

[10] Beringer et al. Review of particle physics. *Phys. Rev. D*, 86:010001, Jul 2012.

[11] Makoto Kobayashi and Toshihide Maskawa. CP Violation in the Renormalizable Theory of Weak Interaction. *Prog.Theor.Phys.*, 49:652–657, 1973.

[12] Amsler et al. Review of particle physics. *Physics Letters B*, 667(1–5):1–6, 2008. Review of Particle Physics.

[13] Cern experiments observe particle consistent with long-sought higgs boson.

[14] Abdelhak Djouadi. The Anatomy of electro-weak symmetry breaking. I: The Higgs boson in the standard model. *Phys.Rept.*, 457:1–216, 2008.

[15] R. Barate et al. Search for the standard model Higgs boson at LEP. *Phys.Lett.*, B565:61–75, 2003.

[16] Updated Combination of CDF and D0 Searches for Standard Model Higgs Boson Production with up to 10.0 $\text{fb}^{-1}$ of Data. 2012.

[17] *The LEP Electroweak Working Group.*

[18] *A Generic fitter project for HEP Model Testing.*

[19] S et at Dittmaier. Handbook of LHC Higgs Cross Sections: 2. Differential Distributions. (arXiv:1201.3084. CERN-2012-002), 2012. Working Group web page: https://twiki.cern.ch/twiki/bin/view/LHCPhysics/CrossSections.

[20] Da Huang, Yong Tang, and Yue-Liang Wu. Note on Higgs Decay into Two Photons $H \to \gamma\gamma$. *Commun.Theor.Phys.*, 57:427–434, 2012.

[21] John R. Ellis, Mary K. Gaillard, and Dimitri V. Nanopoulos. A Phenomenological Profile of the Higgs Boson. *Nucl.Phys.*, B106:292, 1976.

[22] Lyndon R Evans and Philip Bryant. LHC Machine. *J. Instrum.*, 3:S08001. 164 p, 2008. This report is an abridged version of the LHC Design Report (CERN-2004-003).

[23] The ATLAS Collaboration. The atlas experiment at the cern large hadron collider. *Journal of Instrumentation*, 3(08):S08003, 2008.

[24] P Lebrun Stephen Myers Ranko Ostojic John Poole Oliver Sim Brning, Paul Collier and Paul Proudlock. Lhc design report. 2004.

[25] Lyndon Evans and Philip Bryant. Lhc machine. *Journal of Instrumentation*, 3(08):S08001, 2008.

[26] The ALICE Collaboration. The alice experiment at the cern lhc. *Journal of Instrumentation*, 3(08):S08002, 2008.

[27] The LHCb Collaboration. The lhcb detector at the lhc. *Journal of Instrumentation*, 3(08):S08005, 2008.

[28] The CMS Collaboration. The cms experiment at the cern lhc. *Journal of Instrumentation*, 3(08):S08004, 2008.

[29] J M Campbell, J W Huston, and W J Stirling. Hard interactions of quarks and gluons: a primer for lhc physics. *Reports on Progress in Physics*, 70(1):89, 2007.

[30] M et al Bajko. Report of the Task Force on the Incident of 19th September 2008 at the LHC. Technical Report LHC-PROJECT-Report-1168. CERN-LHC-PROJECT-Report-1168, CERN, Geneva, Mar 2009.

[31] *ATLAS: letter of intent for a general-purpose pp experiment at the large hadron collider at CERN.* Letter of Intent. CERN, Geneva, 1992.

[32] *ATLAS detector and physics performance: Technical Design Report, 1.* Technical Design Report ATLAS. CERN, Geneva, 1999.

[33] *ATLAS detector and physics performance: Technical Design Report, 2.* Technical Design Report ATLAS. CERN, Geneva, 1999.

[34] W Lampl, S Laplace, D Lelas, P Loch, H Ma, S Menke, S Rajagopalan, D Rousseau, S Snyder, and G Unal. Calorimeter Clustering Algorithms: Description and Performance. Technical Report ATL-LARG-PUB-2008-002. ATL-COM-LARG-2008-003, CERN, Geneva, Apr 2008.

[35] Electron/Gamma public results at. Technical report.

[36] Electron and photon reconstruction and identification in ATLAS: expected performance at high energy and results at 900 GeV. Technical Report ATLAS-CONF-2010-005, CERN, Geneva, Jun 2010.

[37] Evidence for prompt photon production in pp collisions at sqrts = 7 TeV with the ATLAS detector. Technical Report ATLAS-CONF-2010-077, CERN, Geneva, Jul 2010.

[38] M Boonekamp, B Lenzi, N Lorenzo Martinez, P Schwemling, F Teischinger, G Unal, and L Yao. Electromagnetic calorimeter layers energy scales determination. Technical Report ATL-COM-PHYS-2013-1423, CERN, Geneva, Oct 2013.

[39] M Aleksa, C Becot, B Laforge, N Lorenzo Martinez, F Teischinger, and G Unal. Calibration stability and uniformity measurements of electrons and photons. Technical Report ATL-COM-PHYS-2013-1421, CERN, Geneva, Oct 2013.

[40] G. Aad et al. *Expected Performance of the ATLAS Experiment - Detector, Trigger and Physics*. 2009.

[41] ATLAS Collaboration. Electron performance measurements with the atlas detector using the 2010 lhc proton-proton collision data. *The European Physical Journal C*, 72(3):1–46, 2012.

[42] Ruggero Turra, C Meroni, and M Fanti. *Energy calibration and observation of the Higgs boson in the diphoton decay with the ATLAS experiment*. PhD thesis, Milano U., Jan 2013. Presented 18 Feb 2013.

[43] J-B Blanchard, J-B de Vivie, and P Mastrandrea. In situ scales and smearings from Z and $J/\Psi$ events. Technical Report ATL-COM-PHYS-2013-1653, CERN, Geneva, Dec 2013.

[44] Luminosity public plot. Technical report.

[45] Simone Alioli, Paolo Nason, Carlo Oleari, and Emanuele Re. NLO Higgs boson production via gluon fusion matched with shower in POWHEG. *JHEP*, 0904:002, 2009.

[46] Paolo Nason and Carlo Oleari. NLO Higgs boson production via vector-boson fusion matched with shower in POWHEG. *JHEP*, 1002:037, 2010.

[47] A. Djouadi, J. Kalinowski, and M. Spira. HDECAY: A Program for Higgs boson decays in the standard model and its supersymmetric extension. *Comput.Phys.Commun.*, 108:56–74, 1998.

[48] S. Dittmaier et al. Handbook of LHC Higgs Cross Sections: 1. Inclusive Observables. 2011.

[49] Marco Guzzi, Pavel Nadolsky, Edmond Berger, Hung-Liang Lai, Fredrick Olness, et al. CT10 parton distributions and other developments in the global QCD analysis. 2011.

[50] Pavel M. Nadolsky, Hung-Liang Lai, Qing-Hong Cao, Joey Huston, Jon Pumplin, et al. Implications of CTEQ global analysis for collider observables. *Phys.Rev.*, D78:013004, 2008.

[51] A. Sherstnev and R.S. Thorne. Parton Distributions for LO Generators. *Eur.Phys.J.*, C55:553–575, 2008.

[52] G. Aad, B. Abbott, J. Abdallah, A. A. Abdelalim, A. Abdesselam, O. Abdinov, B. Abi, M. Abolins, H. Abramowicz, H. Abreu, and et al. The ATLAS Simulation Infrastructure. *European Physical Journal C*, 70:823–874, December 2010.

[53] S. Agostinelli et al. Geant4—a simulation toolkit. *Nuclear Instruments and Methods in Physics Research Section A: Accelerators, Spectrometers, Detectors and Associated Equipment*, 506(3):250 – 303, 2003.

[54] T. Gleisberg, Stefan. Hoeche, F. Krauss, M. Schonherr, S. Schumann, et al. Event generation with SHERPA 1.1. *JHEP*, 0902:007, 2009.

[55] Differential cross sections of the Higgs boson measured in the diphoton decay channel using 8 TeV pp collisions. Technical Report ATLAS-CONF-2013-072, CERN, Geneva, Jul 2013.